Since 2012

IJAET

International Journal of Automotive Engineering and Technologies

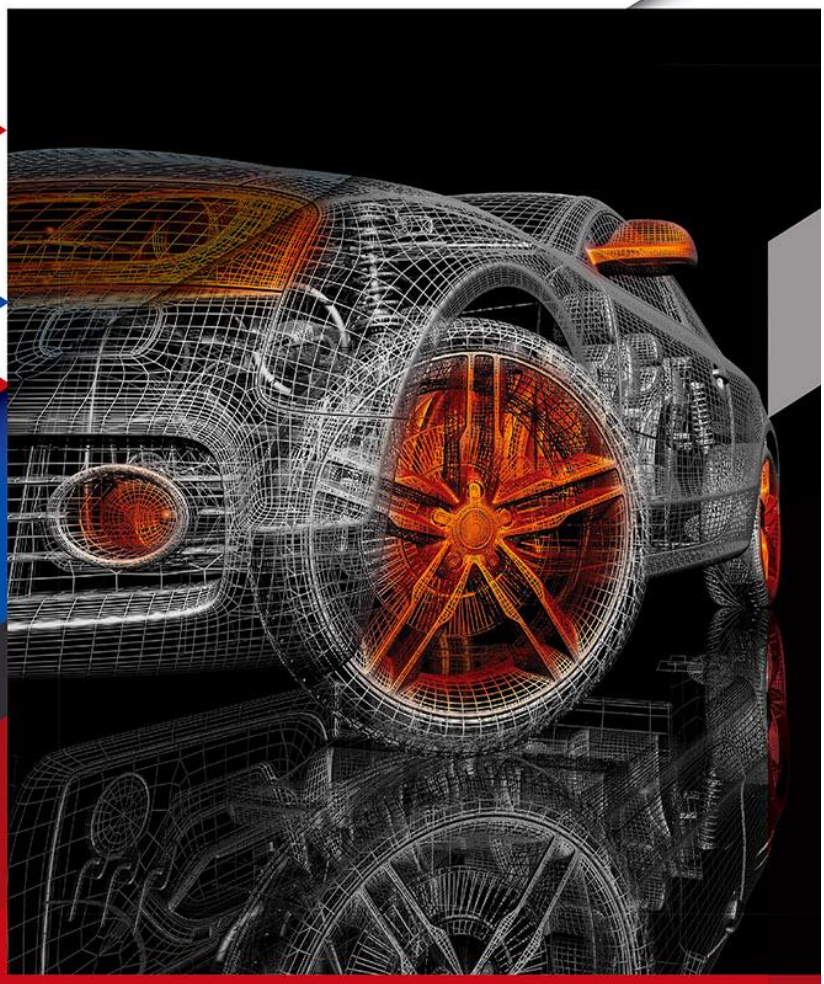

e-ISSN 2146-9067

e-mail: editorofijaet@gmail.com

Editor: Prof. Dr. Murat CİNİVİZ

International Journal of Automotive Engineering and Technologies

e-ISSN: 2146-9067, **Period:** Quarterly

Founded: 2012, **Publisher:** Murat CİNİVİZ

Year : 2023

Volume : 12

Number : 4

https://dergipark.org.tr/tr/pub/ijaet

12.	Prof. Dr. Apostolos PESİRİDİS
13.	Dr. Mohammad AL ZUBİ
14.	Dr. Öğr. Üyesi Fatih AYDIN
15.	Dr. Öğr. Üyesi Mehmet DEMİRALP
16.	Doç. Dr. Tanzer ERYILMAZ
17.	Prof. Dr. Fatih AKSOY
18.	Prof. Dr. Habib GÜRBÜZ
19.	Doç. Dr. Aleksandr KABANOV

Language Editor

1.	DR. Öznur YEMEZ

e-ISSN: 2146 - 9067

International Journal of Automotive Engineering and Technologies

journal homepage:
https://dergipark.org.tr/en/pub/ijaet

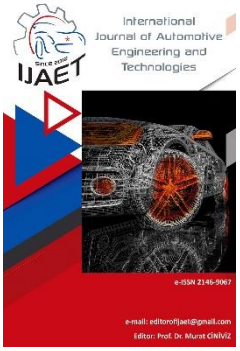

Original Research Article

Utilizing an integrated AHP-COPRAS approach for battery selection in electric vehicles

Aslı Abdulvahitoğlu[1, *], Gözde Ekmekçi Güçlüten[2]

[1, *2] Adana Alparslan Türkeş Science and Technology University, Engineering Faculty, Mechanical Engineering Department, Adana, Türkiye.

ARTICLE INFO

Orcid Numbers
1. 0000-0002-3603-6748
2. 0000-0003-0392-1369

Doi: 10.18245/ijaet.1342516

* Corresponding author
aabdulvahitoglu@atu.edu.tr

Received: Feb 13, 2023
Accepted: Oct 04, 2023

Published: 31 Dec 2023

Published by Editorial Board Members of IJAET

ABSTRACT

Internal combustion engine vehicles provide better performance and longer-range using fossil fuels such as gasoline and diesel. However, fossil fuels are non-renewable and cause environmental pollution, alternative fuels such as blends of ethanol and biodiesel, hydrogen etc have been sought for these vehicles. On the other hand, some researchers prefer to design alternative vehicles such as hybrid and electrical vehicles, instead of changing the fuel type. Among the studied topics for alternative vehicles, the battery is one of the most important components, especially in electrical vehicles. Batteries are diversified with different criteria such as battery life, nominal voltage, energy density, volumetric energy density, specific power, operating temperature, and production cost. In this study, the expert perspective was utilized when selecting the battery type to be employed for the energy source through utilizing the Integrated Analytical Hierarchy Process (AHP) - Complex Proportional Assessment (COPRAS), a multi-criteria decision-making approach. Various batteries such as Lead-acid (Pb-acid), Nickel-cadmium (Ni-Cd), Ni-MH, Sodium Nickel Chloride (Zero Emission Battery Research Activity-ZEBRA), Lithium –Ion (Li-Ion) Battery were evaluated in terms of different criterion. Among the alternatives the Li-ion battery type is chosen as the best option and the Ni-Cd battery is the least chosen alternative.

Keywords: Battery Selection, Electric Vehicle, AHP, COPRAS, Multi-Criteria Decision-Making

1. Introduction

Traditional automobiles, also known as internal combustion engine vehicles (ICEVs), are often used because of their efficiency and accessibility to fuel. However, they run on fossil fuels and emit dangerous pollutants including carbon monoxide, nitrogen oxides and unburn hydrocarbons. Particularly, the transportation industry is the source of these dangerous exhaust gases. It has been demonstrated that these gases substantially affect the health of living beings, particularly humans [1]. Concerns regarding climate change have driven the need for eco-conscious substitutes for regular internal

combustion engine (ICE) cars, aiming to cut down on greenhouse gas and carbon discharges. Electric vehicles (EVs) are gaining traction as an environmentally mindful, reduced-carbon, and enduring substitute for internal combustion engines (ICEs) [2]. Since their historical growth began in the 19th century, electric vehicles (EVs) have gained popularity, especially in light of the rise in greenhouse gases and air pollution brought on by internal combustion engines. The quantity of EVs in operation has surged significantly over the past ten years, rising from 17,000 in 2010 to over 15 million by 2021 [3]. According to Turkish Standard Instute, there are 14,706,162 registered vehicles in Türkiye. Approximately 98.5% of the registered vehicles are fossil-fueled (27.8% gasoline, 36.4% diesel, 34.3% LPG), 1.2% hybrid, and 0.2% electrical vehicles [4].

Studies on various EV kinds are becoming more prevalent every day. Three categories best describe the types of EVs now in use. The first item that typically springs to mind is EVs, also known as All Electric Vehicles, which derive all of their energy from a battery pack. Recently, as battery technology has advanced, interest in all-electric vehicles has grown. However, hybrid electric vehicles—which combine an internal combustion engine with an electric motor for propulsion—are among the most popular types of EVs today. The literature refers to another form of EV as fuel cell electric vehicles that use hydrogen energy [5].

Compared to cars powered by internal combustion engines, electric vehicles use quite different technology. These automobiles utilize electric motors that utilise electric energy [6]. Parts used in energy storage and conversion include batteries, fuel cells, and supercapacitors, which are all members of the energy converter family. To meet the varied energy needs of different devices and systems, all three are necessary. However, they are unable to handle all applications on their own [7].

Batteries are the essential power source for electric vehicles, utilizing chemical reactions to supply energy for vehicle functioning. This approach obviates the necessity for fossil fuels, provided the electricity fueling EVs originates from sustainable sources. During discharge, batteries transform chemical energy into electrical energy, and during charging, they reverse this process, converting electrical energy back into chemical energy. Batteries serve as reliable storage units for energy, offering diverse power and capacity options. Achieved by connecting battery cells in series or parallel, this flexibility enables their application in various contexts.

The batteries in EVs are their most costly component. EV battery costs were on average $750/kWh in 2010, $500/kWh in 2012, and $380/kWh in 2014. Since then, the cost has dropped significantly. It is predicted that the unit cost of EVs would reduce as a result of this anticipated decline, increasing consumer buying power [8]. Battery technology is the most important piece of technology for the creation of electric cars. The battery types that will be employed in this study will be briefly described before delving into the specifics of the battery chemistry of electric cars [9].

Lead-acid (Pb-Acid) Battery: Lead-acid batteries are the most traditional and well-known kind of rechargeable batteries. This battery technology is so popular across the world for several reasons. The technology that underpins lead-acid batteries is straightforward, affordable to produce, widely used, and simple to build. The comparatively compact batteries are strong and dependable, and they require almost little maintenance. They also fit easily inside the engine compartment. The relatively short cycle life and working life of the battery, however, are the limiting considerations for these batteries. Lead-acid batteries typically last 5 to 15 years [10] or 1200 to 1800 charge-discharge cycles.

Nickel-cadmium (Ni-Cd) Battery: Nickel-cadmium batteries have a long lifespan and may be completely depleted without suffering any harm. It discharges current at a rapid rate. Higher specificity and gravitational energy density than lead-acid batteries. Both its power and cycle life are longer. The expensive nature of this battery is one of the factors limiting its utilisation. The high expense of recycling the material is the major cause of this. Cadmium is a heavy metal that is exceedingly hazardous and may pollute the environment if improperly disposed of [11].

Ni-MH Battery: The most popular nickel-based battery is the Ni-MH, which entered the market in 1991. Compared to lead-acid and nickel-

cadmium batteries, it has a higher weight energy density and specific power. But they are also more expensive than lead-acid batteries due to the greater price of nickel and hydride-storing metals. They are free of poisonous substances. Ni-MH batteries are not promising batteries because of the high nickel content and high nickel costs. Ni-MH batteries are not promising batteries because of the high nickel content and high nickel costs [12].

ZEBRA Battery: Zebra batteries are another name for Sodium Nickel Chloride (NaNiCl) batteries. The project "Zero Emission Battery Research Activity" gave rise to the moniker Zebra. Lead acid and nickel-based batteries have lower energy density and nominal voltage values. This battery's drawbacks are low specific power, self-discharge issue, and temperature control [8].

Li-Ion Battery: When compared to other battery types like Pb-acid and Ni-MH, Li-ion batteries stand out as one of the most innovative energy storage options due to their properties like high energy and power densities and extended shelf lives. There is a lot of energy that can be held per unit of weight and volume. However, the lifespan of a lithium-ion battery is temperature-dependent; at higher temperatures, ageing occurs considerably more quickly, and deep discharges significantly shorten the cycle life. Li-ion batteries are particularly vulnerable to overcharging and deep discharge, which can harm them, decrease their lifespans, and even put them in risky circumstances [13].

In multi-criteria decision-making, first, the problem is determined, then the problem is structured and the result is reached by using the model. The processes they follow are normalization of data, weighting of criteria and ranking of alternatives. There are many weighting methods in the literature such as AHP, SWARA, CRITIC, ENTROPY, and DEMATEL decision-making methods in the literature. Such as AHP, ANP, TOPSIS, ARAS, WASPAS, CODAS, COPRAS, MABAC, MAIRCA [14]. MCDM is used in almost every area where the decision is needed such as Chemistry [15], Earth and Planetary Sciences [16], Economics, Econometrics and Finance [17], Material Science [18], Energy [19, 20, 21, 22, 23, 24, 25], Agricultural and Biological Science [26] Environmental Science [27,28] , Decision Science [29,30], Business, Management and Accounting[31], Engineering[32,33], Computer Science [34,35].

Loganathan et al. developed a multi-criteria decision-making technique-based methodology, with categories depending on cathode/anode material for the selection of Li-ion batteries. The technique helps original equipment manufacturers of electric vehicles choose the optimum battery and optimize the price and efficiency of electric vehicles. The Lithium-Titanate ($Li_4Ti_5O_{12}$) battery was shown to be the best all-around battery appropriate for electric vehicle applications as a consequence of the presented technique [36].

Sonar and Kulkarni sought to present the best alternative in current electric vehicles by combining the analytical hierarchy process (AHP) and the multi-attribute boundary approach area comparison (MABAC) method as a multi-criteria decision-making tool (MCDM) for the selection and ranking of the best alternative. According to the AHP weighting, the driving range received more attention from the experts. The Hyundai Kona is picked as the top option based on the performance selection criteria used in the MABAC approach since it has the greatest performance score of all the alternatives considered. For clients looking for inexpensive cars where price is a major concern, Tata Tigor has done well [37].

Chakraborty and Saha used a multi-criteria group decision making (MCGDM) approach to determine the optimal recycling strategy for Lithium-Ion Batteries in a Fermatean fuzzy environment (FFE). Under FFE, a new entropy measure (EM) and numerous aggregation operators (AOs) have been added. According to the proposed method, the best alternative for lithium-ion battery (LIB) recycling is "a combination of mechanical shredding (MS), electrolyte extraction (EE), electrode dissolution (ED), and cobalt electrochemical reduction (CECR) [38].

Wu et al. present a decision assistance tool for assessing commercial (small-scale) energy storage devices. It then determines the best option(s) depending on the preferences of the users. The ranking findings clearly illustrate that user preferences have a significant influence on the recommended energy storage solutions [39].

For the thorough assessment of battery energy

storage systems, Zhao et al suggested an integrated fuzzy-MCDM (multi-criteria decision making) model incorporating the Fuzzy-Delphi methodology, the Best-Worst method (BWM), and fuzzy-cumulative prospect theory (CPT). The empirical results reveal that Li-ion batteries are the preferred choice for micro-grid demonstration projects, followed by NaS batteries and NiMH batteries. Even if decision makers and investors have different risk preferences, the results show that when considering technological, environmental, economic, social, and performance factors, the Li-ion battery is still the best, followed by the NaS battery [40].

Yücenurşen and Sabancı investigated Different battery types for use in converting a small and light (600-1000 kg) ICE vehicle into an electric vehicle. The investigation was carried out to guarantee that this vehicle is acceptable for urban use and has a range of about 100 kilometers. Each battery technology's capacity is estimated to be around 15 kWh. When doing the techno-economic study of various battery types, it was taken into account that they delivered the required energy for about ten years. For comparison, seven different battery technologies (lead-acid, gel, Ni-Cd, Li-Ion, $LiFePo_4$, LiPo, and Ni-MH) were employed. Price assessment in US Dollars ($), 10-year investment cost, weight and volume values, as well as weight and volume values necessary to create 1 kWh of energy, were included in the analysis tables. The analysis found that the cheapest technology for a 10-year lifetime was lead-acid technology. Lead-acid technology is 30% less costly than the second-cheapest gel technology and 82% less expensive than the most expensive technology, LiPo technology. The investigation discovered that the lightest technology was LiPo. This technique has been proven to be 85% lighter than gel technology. Aside from this information, tabular statistics on cycle life, self-discharge, benefits and downsides are provided [41].

The goal of this article is to select the best battery type for electric cars that also fits the distinctive criteria specified by experts, from among the five various battery types analyzed. The AHP approach, a multi-criteria decision-making process, will be researched to assess the weight of each criterion and then choose the best alternative among the given batteries. This study will discuss the electric car batteries issue and, with the help of expert judgment, by using integrated AHP-COPRAS, one of the multi-criteria decision-making approaches, to select the best battery type.

2. MATERIAL AND METHODS

The battery type and attributes were analyzed using the AHP approach in this study, and a decision-making study was conducted. First and foremost, battery factors influencing battery selection were investigated for this aim. Nominal voltage, energy density, volumetric energy density, specific power, life cycle, and operating temperature are some of these properties [42]. In light of this knowledge, our decision-making criteria will be based on nominal voltage, energy density, volumetric energy density specific power, life cycle, operating temperature, and production cost, all of which are debatable for all battery kinds.

This section evaluates AHP by comparing different criteria and battery types based on expert assessments. A total of seven specialists were interviewed bilaterally. Two of the specialists are engineers who are industry professionals in their professions, and five of them are academics.

Analytical Hierarchy Process (AHP)

Thomas L. Saaty created the Analytical Hierarchy Process (AHP), a multi-criteria decision-making technique, in 1971 [43]. AHP; It is made out of previously understood discrete ideas and methods such as pairwise comparison, eigenvector-based weight derivation, and consistency measurement. Every element at every level is put through a two-way comparison with a target element [44]. When distributing weights, AHP has the option of allowing a hierarchical structure of criteria, which enables users to better concentrate on certain (primary) criteria and sub-criteria. A different construction might result in a different final ordering, thus this step is crucial. The decision maker should attempt to cluster these items similarly when building the AHP hierarchy with a lot of them [45].

The Analytical Hierarchy Process (AHP) is used in this study to assign weights to criteria. Figure 1 displays the battery type selection hierarchy framework, and Table 1 lists the importance

scale values along with their related meanings.

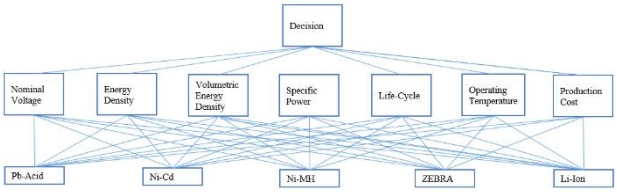

Figure 1. A hierarchical framework for selecting batteries.

Table 1. Importance scale values and definitions [44]

	Intensity of importance	
Saaty 1-9 Scale	1	Equal Importance (EI)
	3	Moderate Importance (MI)
	5	Strong Importance (SI)
	7	Very Strong Importance (VSI)
	9	Extreme Importance (EI)
	2, 4, 6, 8	Intermediate values

The calculation of AHP involved utilizing the following mathematical formula. Specifically, formula 1 was applied to the components listed below the diagonal [46].

$$A=\begin{bmatrix} a_{12} & a_{12} & . & . & a_{1n} \\ a_{21} & a_{22} & . & . & a_{2n} \\ \dots & . & . & . & . \\ \dots & . & . & . & . \\ a_{n1} & a_{n2} & . & \dots & a_{nn} \end{bmatrix} \qquad a_{ji}=\frac{1}{a_{ji}} \qquad (1)$$

The matrix is created using the normalizing technique to evaluate the significance levels of the components, with a particular emphasis on equation 2 [47].

$$B_i=\begin{bmatrix} b_{11} \\ b_{21} \\ .. \\ .. \\ b_{n1} \end{bmatrix} \qquad bi_j=\frac{a_{ij}}{\sum_{i=1}^{n} a_{ij}} \qquad (2)$$

Following that, matrix C is created by combining a collection of B-column vectors in a matrix structure, equal to the number of components. The Priority Vector, which displays the significance values, is then utilized to calculate the mathematical mean of matrix C's row components [44].

The number of elements and a coefficient (λ) known as Eigen Value is used to determine the Consistency Ratio (CR). To acquire the D column vector, initially compare the comparison matrix A with the priority vector W.

$$C=\begin{bmatrix} c_{11} & c_{12} & .. & .. & c_{1n} \\ c_{21} & c_{22} & .. & .. & c_{2n} \\ .. & .. & .. & .. & .. \\ .. & .. & .. & .. & .. \\ c_{n1} & c_{n2} & .. & .. & c_{nn} \end{bmatrix} \quad W=\begin{bmatrix} W_1 \\ W_2 \\ .. \\ .. \\ W_n \end{bmatrix} \quad W_i=\frac{\sum_{j=1}^{n} c_{ij}}{n} \qquad (3)$$

$$D=\begin{bmatrix} a_{11} & a_{12} & .. & .. & a_{1n} \\ a_{21} & a_{22} & .. & .. & a_{2n} \\ .. & .. & .. & .. & \dots \\ .. & .. & .. & .. & .. \\ a_{n1} & a_{n2} & \dots & .. & a_{nn} \end{bmatrix} \times \begin{bmatrix} w_1 \\ w_2 \\ .. \\ . \\ w_n \end{bmatrix} \qquad (4)$$

Equation (5) is used to calculate E, and the arithmetic mean value (equation 6) yields the eigenvalue λ.

$$E_i=\frac{d_i}{w_i} \qquad (i=1,2,....n) \qquad (5)$$

$$\lambda=\frac{\sum_{i=1}^{n} E_i}{n} \qquad (6)$$

After calculating the λ, it becomes possible to determine the Consistency Indicator (CI) using equation 7. In addition, the Consistency Ratio (CR) may be derived by dividing the calculated value by the equation (8) and comparing the CI value to the Random Consistency Index (RI) in Table 2.

$$CI=\frac{\lambda-n}{n-1} \qquad (7)$$

$$CR=\frac{CI}{RI} \qquad (8)$$

Table 2. Values for the random consistency index [48]

n	1	2	3	4	5	6	7	8	9	10
RI	0	0	0.58	0.9	1.12	1.24	1.32	1.41	1.45	1.49

The consistency test is considered complete after the CR is determined. The obtained data is consistent if the CR is less than 10%, showing that the comparison matrix is reliable. If the CR is equal to or more than 10%, the collected data is erratic, and the comparison matrix should be altered [19].

Table 3 was generated using experimental numbers from the literature for five distinct battery types.

Table 3. Comparison of Battery Types [49-55]

Battery Property	**Pb-Acid**	**Ni-Cd**	**NiMH**	**ZEBRA**	**Li-Ion**
Nominal Voltage (V)	2.0	1.2	1.2	2.6	3.6
Energy Density (MJ/L)	0.36	1.08	1.55	0.32-0.43	0.83-3.6
Volumetric energy density (Wh L^{-1})	100	300	180-220	160	200-400
Specific Power (W kg^{-1})	180	200	200-300	155	200-430
Life-Cycle	1000	2000	<3000	>1200	2000
Operating Temperature (°C)	-15 to +50	-20 to +50	-20 to +60	+245 to +350	-20 to +60

Tablo 4. Experts' response to the one-on-one interview

Decision Variables	*Experts*	*C1*	*C2*	*C3*	*C4*	*C5*	*C6*	*C7*
	E1	1	1/3	1/5	1/3	1/7	1	1/3
	E2	1	1/5	1/5	1/5	1/2	1	1/2
	E3	1	1/5	1/7	1/5	1/7	/3	1/9
Nominal voltage C1	***E4***	1	1/5	1/5	1/7	1/7	/3	1/7
	E5	1	1/3	1/3	1	1/3	1	1/3
	E6	1	1/3	1/7	1/3	1/2	1	1/9
	E7	1	1/5	1/7	1/5	1/7	/3	1/9
	E1	3	1	1	1/3	1/5	3	1/3
	E2	5	1	1	1	1/2	1	1/2
	E3	5	1	1	1	1/3	3	1/5
Energy Density C2	***E4***	5	1	1	1/3	1/3	3	1/5
	E5	3	1	1/3	1	1/3	3	1/3
	E6	3	1	1/7	1/3	3	1	1/9
	E7	5	1	1/3	1	1/3	3	1/5
	E1	5	1	1	1	1/3	3	1/3
	E2	5	1	1	1	1/2	1	1/2
	E3	7	3	1	1	1/3	3	1/5
Volumetric Energy Density C3	***E4***	5	1	1	1/3	1/3	3	1/5
	E5	3	3	1	3	1/2	3	1/2
	E6	7	7	1	1	3	3	1/7
	E7	7	3	1	1	1/3	3	1/5
	E1	3	3	1	1	1/3	5	1/3
	E2	5	1	1	1	1/2	1	1/2
	E3	5	1	1	1	1/3	3	1/5
Specific Power C4	***E4***	7	3	3	1	1	5	1
	E5	1	1	1/3	1	1/2	2	1/2
	E6	3	3	1	1	3	3	1/7
	E7	5	1	1	1	1/3	3	1/5
	E1	7	5	3	3	1	5	1/3
	E2	7	2	2	2	1	2	2
	E3	7	3	3	3	1	5	1/3
Life-cycle C5	***E4***	7	3	3	1	1	7	1
	E5	3	3	2	2	1	2	1/2
	E6	2	1/3	1/3	1/3	1	2	1/9
	E7	7	3	3	3	1	5	1/3
	E1	1	1/3	1/3	1/5	1/5	1	1/5
	E2	3	1	1	1	1/2	1	1/3
	E3	3	1/3	1/3	1/3	1/5	1	1/7
Operating Temperature C6	***E4***	3	1/3	1/3	1/5	1/7	1	1/7
	E5	1	1/3	1/3	1/2	1/2	1	1/3
	E6	1	1	1/3	1/3	1/2	1	1/9
	E7	3	1/3	1/3	1/3	1	1	1/7
	E1	3	3	3	3	3	5	1
	E2	7	2	2	2	1/2	3	1
	E3	9	5	5	5	3	7	1
Production cost C7	***E4***	7	3	5	1	1	7	1
	E5	3	3	2	2	2	3	1
	E6	9	9	7	7	9	9	1
	E7	9	5	5	5	3	7	1

Table 5. Decision Matrix for criteria

Decision Variables	C1	C2	C3	C4	C5	C6	C7
C1	1.0000	0.2489	0.1863	0.2776	0.2306	0.6245	0.1954
C2	4.0169	1.0000	0.5533	0.6245	0.4494	2.1918	0.2425
C3	5.3691	2.1145	1.0000	1.0000	0.5123	2.5643	0.2664
C4	3.6025	1.6013	1.0000	1.0000	0.5993	2.8002	0.3353
C5	5.1857	2.2250	1.9520	1.6685	1.0000	3.5424	0.4562
C6	1.8734	0.4562	0.3900	0.3571	0.3553	1.0000	0.1842
C7	6.1198	3.8328	3.7537	2.9827	2.1918	5.4285	1.0000

Table 6. Normalized matrix for criteria

Decision Variables	C1	C2	C3	C4	C5	C6	C7
C1	0.0368	0.0217	0.0211	0.0351	0.0432	0.0344	0.0729
C2	0.1479	0.0871	0.0626	0.0789	0.0842	0.1207	0.0905
C3	0.1976	0.1842	0.1132	0.1264	0.0960	0.1413	0.0994
C4	0.1326	0.1395	0.1132	0.1264	0.1123	0.1543	0.1251
C5	0.1909	0.1938	0.2209	0.2109	0.1873	0.1952	0.1702
C6	0.0690	0.0397	0.0441	0.0451	0.0665	0.0551	0.0687
C7	0.2253	0.3339	0.4249	0.3771	0.4105	0.2991	0.3731

COPRAS method

Zavadskas and Kaklauskas presented the COmplex Proportional ASsessment approach to the literature in 1996 [56]. It is used to rank and assess options while taking the benefit and cost features of the criterion into account [14]. The distinction between this approach and other MCDM methods is that the options may be compared to each other and their superiority over each other can be expressed as a percentage. The application of this method is as follows

i. Decion matrix created

$$A_{ij} = \begin{matrix} a_{11} & \dots & a_{1p} \\ \vdots & \ddots & \vdots \\ a_{m1} & \dots & a_{mp} \end{matrix}$$

where m is alternative and p is criteria

ii. The elements of matrix A are used to compute the normalized decision matrix (X*). The elements of the normalized resolution matrix are represented by (x_{ij}^*). Equation (9) was implemented to calculate (x_{ij}^*).

$$x_{ij}^* = \frac{x_{ij}}{\sum_{i=1}^{m} x_{ij}} \quad (i = 1, \dots, m \; and \; j = 1, \dots p) \tag{9}$$

$$X^* = \begin{matrix} x_{11}^* & \dots & x_{1p}^* \\ \vdots & \ddots & \vdots \\ x_{m1}^* & \dots & x_{mn}^* \end{matrix}$$

iii. The weighting of the normalized decision matrix is determined using equation 10 and the weights w_i.

$$n_{ij} = x_{ij}^* w_j \tag{10}$$

iv. S_i^+ and S_i^- values calculated
S_i^+ the sum of utility criteria in a weighted normalized decision matrix
S_i^- the sum of cost criteria in a weighted normalized decision matrix

v. Equation 11 is used to compute relative significance values.

$$Q_i = S_i^+ + \frac{\sum_{i=1}^{m} S_i^-}{S_i^- \sum_{i=1}^{m} \left(\frac{1}{S_i^-}\right)} \tag{11}$$

vi. Equation 12 is used to calculate the value of the performance index.

$$P_i = \left(\frac{Q_i}{Q_{max}}\right) * 100 \tag{12}$$

3. RESULT AND DISCUSSION

Seven experts were interviewed one-on-one and questions were posed Table 4 has been prepared. By taking the geometric mean of the values given in Table 4, the decision matrix (Table 5) was generated.

In order to normalize the decision matrix (table 5) equation 2 was used. Results tabulated in Table 6.

Once the normalization was completed, the eigenvector, eigenvalue, consistency index and consistency ratio were determined by using equations 3 to 8. The results were tabulated in Table 7.

The CR is less than 10%, implying that the data acquired is consistent, demonstrating that the matrix used for comparison is reliable. The weighted outcomes of the criterion calculations are tabulated in Table 8.

where wC1: weight of Nominal voltage, wC2: weight of Energy Density, wC3: weight of Volumetric Energy Density, wC4: weight of Specific Power, wC5: weight of Life-cycle, wC6: weight of Operating Temperature, wC7: weight of Production cost

Ranking the batteries with COPRAS

After the weights are determined by AHP, a ranking will be made between the alternatives with the COPRAS method. To appeal to the consumer (buyer), the manufacturing cost requirement was also added, and expert opinions were sought.

In addition to the values given in the literature, linguistic evaluation such as expensive, very expensive, given verbally, is given a 1 to 9 scale to be close to the Saaty scale.

Table 7. The results of the eigenvector, eigenvalue, consistency index and consistency ratio

eigen vector	*eigenvalue*	*λmax*	*CI*	*CR*
0.037884	0.271082	7.30908	0.0515	0.0382
0.095996	0.698679			
0.136866	1.007783			
0.129048	0.945755			
0.195612	1.443963			
0.05548	0.403517			
0.349114	2.577456			

Table 8. Weight of the criteria

w_{C1}	w_{C2}	w_{C3}	w_{C4}	w_{C5}	w_{C6}	w_{C7}
0.0379	0.0960	0.1369	0.1291	0.1956	0.0555	0.3491

Table 9. Production cost

	Pb-Acid	**Ni-Cd**	**NiMH**	**ZEBRA**	**Li-Ion**
Production Cost	Cheap	Over costing	Over costing	Average	Over costing

Table 10. Linguistic Scale

Linguistic	**Scale**
Very Cheap	1
Cheap	3
Average	5
Expensive	7
Very Expensive	9

To evaluate the batteries the chosen criteria are coded as: *C_1: Nominal voltage criteria, C_2: Energy Density criteria, C_3: Volumetric Energy Density, C_4: Specific Power criteria, C_5: Life-cycle criteria, C_6: Operating Temperature criteria, C_7: Production cost criteria*

The decision matrix was created using literature [49-55]. The alternatives of batteries were symbolized as Pb-Acid: A1, Ni-Cd: A2, Ni-Mh: A3, Zebra: A4, and Li-ion: A5, respectively. While creating the decision matrix operating temperature is given as a range so the maximum temperature is chosen for evaluation since it is considered a utility. In addition to this assumption, Life-cycle criteria were given for the battery Ni-Mh as <3000 and also for the ZEBRA type battery >1200 these values were taken as 2900 and 1300, respectively.

Table 11. Decision matrix for evaluating alternative batteries

Alternatives	*Criteria*						
	C_1	C_2	C_3	C_4	C_5	C_6	C_7
A_1	2	35	100	180	1000	50	3
A_2	1.2	80	300	200	2000	50	9
A_3	1.2	95	220	300	2900	60	9
A_4	2.6	120	160	155	1300	350	5
A_5	3.6	250	400	430	2000	60	9

In order to normalize the decision matrix (Table 11) equation 9 was used and the results were tabulated in Table 12.

The weight of the criteria that were calculated by the AHP method was used to calculate the weighted normalized matrix by using equation 10 and the results are tabulated in Table 13.

Table 12. Normalized matrix for alternative batteries

C_1	C_2	C_3	C_4	C_5	C_6	C_7
0.1887	0.0603	0.0847	0.1423	0.1087	0.0877	0.0857
0.1132	0.1379	0.2542	0.1581	0.2174	0.0877	0.2571
0.1132	0.1638	0.1864	0.2372	0.3152	0.1053	0.2571
0.2453	0.2069	0.1356	0.1225	0.1413	0.6140	0.1429
0.3396	0.4310	0.3390	0.3399	0.2174	0.1053	0.2571

Table 13. Weighted normalized matrix

C_1	C_2	C_3	C_4	C_5	C_6	C_7
0.0071	0.0058	0.0116	0.0184	0.0213	0.0049	0.0299
0.0043	0.0132	0.0348	0.0204	0.0425	0.0049	0.0898
0.0043	0.0157	0.0255	0.0306	0.0617	0.0058	0.0898
0.0093	0.0199	0.0186	0.0158	0.0276	0.0341	0.0499
0.0129	0.0414	0.0464	0.0439	0.0425	0.0058	0.0898

The criterion C1 to C6 are utility criteria and C7 is the cost criteria. Si+ and Si- values are calculated where Si+ the sum of utility criteria in a weighted normalized decision matrix and Si- the sum of cost criteria in a weighted normalized decision matrix. Si+ and Si- values were used to compute the relative significance values. Equation 11 is used to compute relative significance values (Qi). And the gained results are tabulated in Table 14.

Table 14. Relative Significance values of the alternatives

Alternative	S_i^+	S_i^-	$1/S_i^-$	Q_i
A_1	0.0690	0.0299	33.4183	0.2033
A_2	0.1201	0.0898	11.1394	0.1649
A_3	0.1436	0.0898	11.1394	0.1884
A_4	0.1252	0.0499	20.0510	0.2058
A_5	0.1929	0.0898	11.1394	0.2376

Relative significance values were used to calculate the performance indices. Performance indices were calculated by using Equation 12 and the computed results are tabulated in Table 15. The performance index shows the ranks of alternatives.

Table 15. Performance index

	Performance index
P_1	85.5551
P_2	69.3848
P_3	79.2800
P_4	86.6036
P_5	100.00

Table 16. Ranks of batteries

Alternative	*Performance index*	*Rank*
A_1	*85.5551*	*3*
A_2	*69.3848*	*5*
A_3	*79.2800*	*4*
A_4	*86.6036*	*2*
A_5	*100*	*1*

Once the performance index is calculated the ranks of the alternatives which are tabulated in Table 16 come to the fore.

where A_1: Pb-Acid, A_2: Ni-Cd, A_3:Ni-Mh, A_4: Zebra, A_5: Li-ion, respectively.

The calculations show that alternative A5, with the highest performance index, is the best option, while alternative A2, with the lowest performance index, is the worst. In terms of battery preferences, the final ranking is as follows: Li-ion, Zebra, Pb-Acid, Ni-Mh, and Ni-Cd, in that order. A decision has been made to encourage the development and deployment of alternative Li-ion, which has the greatest performance index.

4. CONCLUSION

The environmental damage of internal combustion engines threatens the balance of the world. For this reason, scientists have started to search for renewable alternative vehicles in terms of environmental impact and health. Electric vehicles have grown in popularity among researchers because they are safe, ecologically benign, and long-lasting.

The analytical hierarchy technique was used to examine the properties of five distinct battery types (Pb-Acid, Ni-Cd, NiMH, ZEBRA, and Li-Ion) in this study. The present study examined seven distinct battery properties (nominal voltage, energy density, volumetric energy density, specific power, life cycle, operating temperature, and production cost) and five different battery types. The relevance of attributes is given as manufacturing cost, life-cycle, volumetric energy density, specific

power, energy density, operating temperature, and nominal voltage, according to determined weighted results using AHP. Based on this point, the COPRAS method assessment of five distinct battery types revealed that Li-Ion is the best-suited battery type and Ni-Cd is the least favorable among the analyzed battery kinds. In prospective research, different attributes and battery kinds can be produced. Similarly, the outcomes may be compared using various multi-criteria decision-making procedures.

Acknowledgement:

The authors wish their sincere thanks to Prof. Kadir Aydın, Assoc. Prof. Gökhan Tüccar, Assoc. Prof. Erinç Uludamar, Assist. Prof. Tayfun Özgür, Assist. Prof. Tahsin Köroğlu, Enes Karabıyık, and Bengü Üst for their valuable answers to the questionnaire.

CRediT authorship contribution statement

Aslı Abdulvahitoğlu: Conceptualization, Formal Analysis, Methodology, Visualization, Writing - original draft, Writing - review & editing. **Gözde Ekmekçi Güçlüten:** Investigation, Resources, Writing - Original Draft

5. References

1. Verma S., Mishra S., Gaur, A., Chowdhury S., Mohapatra S., Dwivedi G. and Verma P. A comprehensive review on energy storage in a hybrid electric vehicle. Journal of Traffic and Transportation Engineering (English Edition), 2021.
2. Troy R. Hawkins, Ola Moa Gausen, Anders Hammer Strømman, Environmental impacts of hybrid and electric vehicles—a review, Int. J. Life Cycle Assess. 17(8), 997–1014, 2012.
3. IEA, Global EV Outlook 2022, Technical Report, International Energy Agency, Paris, France, 2022, https://www.iea.org/reports/global-ev-outlook-2022, Accessed August 2023.
4. TurkStadt https://www.tuik.gov.tr/ accessed August 223
5. Özbay, H., Közkurt, C., Dalcalı, A., Tektaş, M. Geleceğin Ulaşım Tercihi: Elektrikli Araçlar. Akıllı Ulaşım Sistemleri ve Uygulamaları Dergisi, 3 (1), 34-50, 2020.
6. Sezen B. and İşler A.U. Elektrikli Araçların Mevcut Durumu, Tercih Edilme Ve Edilmeme Sebepleri. Turkish Journal of Marketing, 2(2), 82-103, 2017
7. Winter M. and Brodd R.J. What are Batteries, Fuel Cells, and Supercapacitors? Chemical Reviews, 105 (3), 1021-1021, 2005
8. Kerem, A. Elektrikli Araç Teknolojisinin Gelişimi ve Gelecek Beklentileri. Mehmet Akif Ersoy Üniversitesi Fen Bilimleri Enstitüsü Dergisi, 5 (1) , 1-13, 2014.
9. Özcan, Ö. F., Karadağ, T., Altuğ, M., Özgüven, Ö. F. Elektrikli Araçlarda Kullanılan Pil Kimyasallarının Özellikleri ve Üstün Yönlerinin Kıyaslanması Üzerine Bir Derleme Çalışması. GU J Sci, Part A, 8(2), 276-298, 2021.
10. Muratoğlu Y. and Alkaya A. Elektrikli Araç Teknolojisi ve Pil Yönetim Sistemi-İnceleme. Elektrik Mühendisliği, 458, 10-14, Eylül 2016.
11. Budde-Meiwes H, Drillkens J, Lunz B, et al. A review of current automotive battery technology and future prospects. Proceedings of the Institution of Mechanical Engineers, Part D: Journal of Automobile Engineering, 227(5):761-776. 2013
12. Moralı, U. & Erol, S.,18650 lityum-iyon ve 6HR61 nikel-metal hidrit tekrar şarj edilebilir pillerinin elektrokimyasal empedans analizi. Gazi Üniversitesi Mühendislik Mimarlık Fakültesi Dergisi, 35 (1) , 297-310. 2020.
13. Miao Y, Hynan P, von Jouanne A, Yokochi A. Current Li-Ion Battery Technologies in Electric Vehicles and Opportunities for Advancements. Energies; 12(6):1074, 2019
14. Demir G., Özyalçın A. T. Bircan H. Çok Kriterli Karar Verme Yöntemlerive ÇKKV Yazılımı ile Problem Çözümü, Nobel Yayınevi, 382 sf., Mayıs 2021.
15. Alojaiman B., A Multi-Criteria Decision-Making Process for the Selection of an Efficient and Reliable IoT Application, Processes; 11(5):1313,2023.
16. Halder S., Roy M.B., Roy P. K., Sedighi M., Groundwater vulnerability assessment for drinking water suitability using Fuzzy Shannon Entropy model in a semi-arid river basin, CATENA, Volume 229, 107206, 2023
17. Geetha S., Jeon J.H., Stratified network mapping decision making technique based

decision support framework for R&D budget allocation in South Korea, Socio-Economic Planning Sciences, Volume 87, Part B, 101579, 2023.
18. Annamalai, P., Dhavamani, C. Experimental Investigation on Machining of Recycled Aluminum Alloy Metal Matrix Composite in ECMM. Trans Indian Inst Met 76, 1831–1839, 2023.
19. Abdulvahitoglu A., Kilic M., A new approach for selecting the most suitable oilseed for biodiesel production; the integrated AHP-TOPSIS method, Ain Shams Engineering Journal, 13(3), 101604, 2022.
20. Abdulvahitoğlu, A., Abdulvahitoğlu, A., Kılıç, M. Elektrikli Araç Bataryalarının Bütünleşik Swara-Topsis Metodu ile Değerlendirilmesi. Çukurova Üniversitesi Mühendislik Fakültesi Dergisi, 37 (4), 1061-1076, (2022).
21. Fossile, D.K.; Frej, E.A.; da Costa, S.E.G.; de Lima, E.P.; de Almeida, A.T. Selecting the most viable renewable energy source for Brazilian ports using the FITradeoff method. J. Clean. Prod., 260, 121107, 2020.
22. Siksnelyte-Butkiene, I.; Zavadskas, E.K.; Streimikiene, D. Multi-Criteria Decision-Making (MCDM) for the Assessment of Renewable Energy Technologies in a Household: A Review. Energies, 13, 1164,2020.
23. Ebbs-Picken T, Da Silva C. M., Amon C. H., Design optimization methodologies applied to battery thermal management systems: A review Journal of Energy Storage 67, 107460, 2023.
24. Lamya Albraheem, Lama AlAwlaqi, Geospatial analysis of wind energy plant in Saudi Arabia using a GIS-AHP technique, Energy Reports, 9, 5878-5898, 2023.
25. Brodny J., Tutak M., Assessing the energy security of European Union countries from two perspectives – A new integrated approach based on MCDM methods, Applied Energy, 347, 121443, 2023.
26. Äkräs L., Vahvaselkä M., Silvenius F., Seppälä J., Ilvesniemi H., A multi-criteria decision-making framework and analysis of vegetable oils to produce bio-based plastics, Industrial Crops and Products, Volume 188, Part A, , 115584, 2022.
27. Kang D., Jaisankar R., Murugesan V., Suvitha K., Narayanamoorthy S., Omar H. A, Arshad N. I., Ahmadian A., A novel MCDM approach to selecting a biodegradable dynamic plastic product: a probabilistic hesitant fuzzy set-based COPRAS method, Journal of Environmental Management, Volume 340, 17967, 2023.
28. Daniel, M., Ahammed, M.M. & Shaikh, I.N. Selection of Greywater Reuse Options Using Multi-criteria Decision-making Techniques. Water Conserv Sci Eng 8, 2, 2023.
29. Abdulvahitoğlu, A. Prioritization of risk factors causing juvenile delinquency with SWARA Method: A Case Study from Türkiye. Türk İdare Dergisi, 95(496):39-61, 2023
30. Ecer F., Küçükönder H., Kaya S. K., Görçün Ö.F., Sustainability performance analysis of micro-mobility solutions in urban transportation with a novel IVFNN-Delphi-LOPCOW-CoCoSo framework, Transportation Research Part A: Policy and Practice, Volume 172, 103667, 2023.
31. Deveci M., Pamucar D., Gokasar I., Zaidan B. B., Martinez L., Pedrycz W., Assessing alternatives of including social robots in urban transport using fuzzy trigonometric operators based decision-making model, Technological Forecasting and Social Change, 194, 122743, 2023.
32. Can G. F., Toktaş P. and Pakdil F., Six Sigma Project Prioritization and Selection Using AHP–CODAS Integration: A Case Study in Healthcare Industry, in IEEE Transactions on Engineering Management, 70(10), 3587-3600, 2023.
33. Akhoundi, B., Modanloo, V. A multi-criteria decision-making analysis on the extrusion-based additive manufacturing of ABS/Cu composites. Int J Interact Des Manuf 17, 1995–2003, 2023.
34. Nayagam, V.L.G., Suriyapriya, K., Jagadeeswari, M. A Novel Similarity Measure Based on Accuracy Score of Conventional Type of Trapezoidal-Valued Intuitionistic Fuzzy Sets and Its Applications in Multi-criteria Decision-Making Problems. Int J Comput Intell Syst 16, 106, 2023.
35. Lamrini, L., Abounaima, M.C. & Talibi Alaoui, M. New distributed-topsis approach for multi-criteria decision-making problems in a big data context. J Big Data 10, 97,2023.
36. Loganathan M.K., Mishra B., Tan C.M., Kongsvik T. and Rai R.N. Multi-Criteria

decision making (MCDM) for the selection of Li-Ion batteries used in electric vehicles (EVs). Materials Today: Proceedings 41, 1073-1077, 2021.
37. Sonar H.C. and Kulkarni S.D. An Integrated AHP-MABAC Approach for Electric Vehicle Selection. Research in Transportation Business & Management, 41,100665, 2021.
38. Chakraborty S., Saha A. K., Selection of optimal lithium ion battery recycling process: A multi-criteria group decision making approach, Journal of Energy Storage, 55, Part B, 105557, 2022.
39. Wu Z., Khalilpour K., Hämäläinen R. P., A decision support tool for multi-attribute evaluation of demand-side commercial battery storage products, Sustainable Energy Technologies and Assessments, Volume 50, 2022, 101723.
40. Zhao H., Guo S., Zhao H., Comprehensive assessment for battery energy storage systems based on fuzzy-MCDM considering risk preferences, Energy, 168, 450-461, 2019.
41. Yücenurşen, A. & Samancı, A. Battery selection criteria for electric vehicles: techno-economic analysis. International Journal of Automotive Engineering and Technologies, 12(2), 65-74, 2023.
42. Liang Y., Zhao C., Yuan H., Chen Y., Zhang W., Huang J., Yu D., Liu Y., Titirici M., Chueh Y., Yu H. and Zhang Q. A review of rechargeable batteries for portable electronic devices. Wiley Online Library, 1(1), 6-32, 2019.
43. Ünal, Ö. F. Analitik Hiyerarşi Prosesi Ve Personel Seçimi Alanında Uygulamaları. Uluslararası Alanya İşletme Fakültesi Dergisi, 3 (2) , 18-38, 2011.
44. Abdulvahitoğlu A. Using Analytic Hierarchy Process for Evaluating Different Biodiesels as an Alternative Fuel. Çukurova Üniversitesi Mühendislik Mimarlık Fakültesi Dergisi, 33 (3), 177 – 186, 2018.
45. Ishizaka A., Labib A. Review of the main developments in the analytic hierarchy process, Expert Systems with Applications, 38(11), 14336-14345, 2011.
46. Alonso, J.A., Lamata, M.T. Consistency in the Analytic Hierarchy Process: A New Approach. International Journal of Uncertainty, Fuzziness and Knowledge-Based Systems 14, (04), 445-459,2006.
47. Davras, G. M. & Karaatlı, M., Otel İşletmelerinde Tedarikçi Seçimi Sürecinde Ahp Ve Bahp Yöntemlerinin Uygulanması. Hacettepe Üniversitesi İktisadi ve İdari Bilimler Fakültesi Dergisi , 32 (1) , 87-112, 2014 .
48. Awasthi, A., Satyaveer S. Chauhan. Using AHP and Dempster Shafer Theory for Evaluating Sustainable Transport Solutions, Environmental Modelling & Software 26(6):787-796, 2011.
49. Hadjipaschalis, I., Poullikkas, A., & Efthimiou, V. Overview of current and future energy storage technologies for electric power applications. Renewable and Sustainable Energy Reviews, 13(6-7), 1513-1522, 2009.
50. Cano, Z. P., Banham, D., Ye, S., Hintennach, A., Lu, J., Fowler, M. and Chen, Z. Batteries and fuel cells for emerging electric vehicle markets. Nature Energy, 3(4), 279-289, 2018.
51. Perujo, A., Grootveld, G. V., and Scholz, H. Present and future role of battery electrical vehicles in private and public urban transport. In: Z. Stević (Eds), New Generation of Electric Vehicles (pp. 3-25). Intech, 2012.
52. Khaligh, A. and Li, Z. Battery, ultracapacitor, fuel cell, and hybrid energy storage systems for electric, hybrid electric, fuel cell, and plug-in hybrid electric vehicles: State of the art. IEEE Transactions on Vehicular Technology, 59(6), 2806-2814, 2010.
53. Soloveichik, G. L. Battery technologies for large-scale stationary energy storage. Annual Review of Chemical and Biomolecular Engineering, 2(1), 503-527, 2011.
54. Vidyanandan, K. V. Batteries for Electric Vehicles. IEEE, 2019.
55. S. M. Sundaram, M. Kulkarni and V. Diwakar, "Management of large format liion batteries," 2015 IEEE International Transportation Electrification Conference (ITEC), Chennai, India, 2015, pp. 1-7, doi: 10.1109/ITEC-India.2015.7386883.
56. Hezer, S., Gelmez, E., & Özceylan, E. Comparative analysis of TOPSIS, VIKOR and COPRAS methods for the COVID-19 Regional Safety Assessment. Journal of infection and public health, 14(6), 775-786, 2021.

e-ISSN: 2146 - 9067

International Journal of Automotive Engineering and Technologies

journal homepage:
https://dergipark.org.tr/en/pub/ijaet

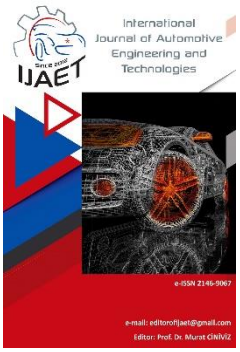

Original Research Article

Investigation of the under-vehicle plastic protection parts manufactured by core-back injection process in terms of strength and weight

Yasemin Gültekin[1], Mustafa Atakan Akar[2], Anıl Altındağ[3], Doğukan Duran[4], Umut Kumlu[5, *]

[1, 3, 4] NOVARES Turkey Otom. A.Ş. TOSB TAYSAD OIZs 2. street 11 path Şekerpınar, Kocaeli, Türkiye.
[2, 5 *] Department of Automotive Engineering, Çukurova University, 01330, Adana, Türkiye.

ARTICLE INFO

Orcid Numbers
1. 0000-0001-9967-8329
2. 0000-0002-0192-0605
3. 0009-0005-0871-4301
4. 0000-0001-8008-5785
5. 0000-0001-7624-6240

Doi: 10.18245/ijaet.1331175

* Corresponding author
umutkumlucrlmkl@gmail.com

Received: Jul 25, 2023
Accepted: Nov 11, 2023

Published: 31 Dec 2023

Published by Editorial Board Members of IJAET

ABSTRACT

Material type, chemical foaming agent, NOx level, core-back distance, and cavity temperature, being the influential parameters in an injection process, significantly affect the weight-based issues and mechanical properties of the resulting product. When the product under inspection is an automotive part, in terms of both the weight and the mechanics are considered to be of high importance. This work is carried out due to a recent task, assigned to NOVARES Engineering and R&D Departments, about the weight reduction of the vehicle underbody plastic protection part (VUPPP), which is located in the rear-lower section of the vehicles. As the core-back process is mostly applied in industry to parts with thickness values of 2.5 mm, the present work involves a challenge due to the fact that before core-back the initial thickness of VUPPP changes between 1.5-1.8 mm. In this study, prototypes are produced with recycled two different polypropylene materials from (PP1 and PP2), two different chemical foaming agents (CFA-X and CFA-Y), six different core-back distances, and two different NOx levels. Finally, laboratory tests are performed on the prototypes to evaluate the weight-based and mechanical features. Experimental data are debated in particular to outline the individual and combined effects of the influential parameters.

Keywords: Core-back process, mold injection, weight reduction, mechanical properties, chemical foaming

1. Introduction

Vehicle parts are designed and manufactured by considering different aspects and targets. The current expectations are lighter components, but having still robust quality and durability; which is mostly recognized in the automotive industry as weight-reduction [1]. As a vehicle body with lower weight results in fewer carbon emissions and lower fuel consumption; mechanical strength is inevitably a primary must. VUPPP is located between the rear wheels and it covers the rear axle of the vehicles. Its visual and CAD data presentation is given in Figure 1, and it has been manufactured by NOVARES since 2015. Recently the task of weight-reduction is assigned for VUPPP; thus, the NOVARES Engineering and R&D Departments focused on this objective.

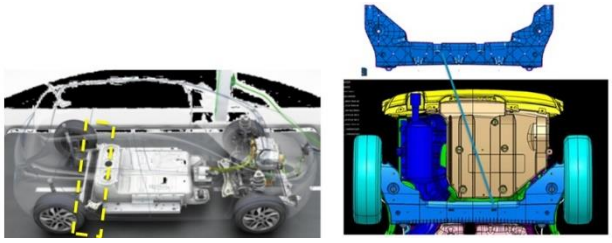

Figure 1. Visual and CAD Data Presentation of the VUPPP.

VUPPP is produced with foam injection molding (FIM) technology. This process is among the most widely used in automotive plastic parts manufacturing processes. In the production of VUPPP, the core-back method is applied to create voids in the internal structure of the sprayed foam. These gaps provide lightening of the product.

Considerable scientific and industrial efforts have been carried out on the core-back FIM process. Liu et al. investigated the influences of four nucleation agents on the nucleation effect and occurring morphologies in the polypropylene foaming injection molding process. Experimental investigations were carried out with and without core-back applications. Both the physical and mixture parameters of the nucleation agents are defined in tabulated form. Results are given in terms of SEM nucleation photos, cell size & cell density, volume expansion ratio, the void fraction of foams, and foaming efficiency. The primary evaluations are (i) the existence of cavities on the boundaries of nucleation agent and polymer, (ii) foaming is observed with the core-back application, (iii) cavities result in higher bubble density and lower bubble diameter, (iv) micro-structures depend on the selection and volume fraction of nucleation agents [2]. In another research, Wang et al., prepared and blended the composition with cellulose nanofibers (CNF) to augment the mechanical features of polypropylene. The composites are prepared with 2 different levels of CNF addition, namely 0.2 and 0.4. Nitrogen (N_2) is applied, by 0.2 wt%, as the physical blowing agent. As the cell density is increased by the addition of CNF, the cell diameters are observed to decrease. Besides the mechanical properties such as tensile modulus and yield stress are recorded to promote by the inclusion of CNF. Moreover, the effects of core-back application are also investigated for different distances which were in the range of 1-9 mm, resulting in expansion ratios of foams with 2-10 fold. Core-back application is determined to weaken the mechanical durability of foam by decreasing the elastic modulus and collapse stress [3]]. Bai et al. investigated the effects of time and compression pressure on the cell built of polystyrene foam during the foaming operation. The investigations were performed with core-back speed and distance of 2 mm/s and 1 mm respectively; moreover, the compression pressure range was 0-300 bar. The main evaluation is the drop in cell diameter and the growth of cell density with compression pressure. Besides, the results indicated that die compression caused high pressure, while the core-back technique provided a rapid pressure reduction. Rapid pressure decrease and higher cavity pressure caused the formation of thin cell builds [4]. A new method with a unique secondary filling stage right after the core-back operation is proposed by Wu et al. It is stated that by combining core-back and secondary filling, a closed shell composed of dense polymer skins can be created right before melt filling. This closed shell is declared to prevent the gas loss from the melt flow front, and act as the gas counter pressure to reduce cell coalescence and collapse, thus leading to significant improvement of cell structure. Tests indicated that plastic foams provide notch impact strength, elastic modulus, and improved tensile strength with the new technology. Azodicarbonamide (AC) was used as the chemical blowing agent; core-back speed and distance of 7 mm/s and 3.5 mm respectively [5]. Pascual et al. foamed a mixture of a polyolefin elastomer (POE), a long-chain branched polypropylene (LCB-PP), and a linear polypropylene (L-PP) with the help of core-back injection molding. The chemical blowing agent Hydrocerol CF 40 E, which is a composition of sodium bicarbonate and sodium citrate, was applied 2 wt%. With the addition of POE, it was observed that the impact response was improved in solids and cellular polymers, while the stiffness decreased. Furthermore, replacing L-PP with LCB-PP in blends including POE has revealed in solids and cellular materials with superior stiffness and impact characteristics[6]. Polyamide 6 (PA6) injection microcellular foams were produced by Jiang et al. via short-

shot and core-back foaming processes to examine the foaming process's effect on cell and surface quality. Experiments were carried out with core-back speed and distance weight reduction values of 20 mm/s, 0.2-10 mm, and 5-25 % respectively; moreover, the chemical foaming masterbatch (F-70) was applied 2 %. Results show that the core-back foaming microcellular foams possess lower deformation of cells, smaller cell size, and narrower cell size distributions with the same weight reduction, compared to the samples prepared using the short-shot foaming process. PA6 microcellular foams that were manufactured via core-back foaming had higher surface glossiness with different weight reductions [7]. Ishikawa and Ohshima foamed copolymer polypropylene with carbon dioxide in a core-back injection-molding investigation. Experiments were carried out with core-back speed and CO2 injection period ranges of 1-10 mm/s and 2-4 s. When the cavity is completely filled, the bubbles disappear; The cavity pressure drops and die plate actuation were confirmed by experiments to induce bubble nucleation. According to the results, it was observed that faster return rates and higher gas concentrations caused an increase in the number of bubbles but reduced the size of the bubbles [8]. The effects of chemical blowing agent content, shot size, mold temperature, holding time, injection speed, holding pressure, and core-back rate [mm/s] on the core-back foam injection molding process was studied by Wu et al. As azodicarbonamide (AC) was used as the chemical blowing agent, the core-back velocity and AC content were in the ranges of 1-9 mm/s and 3-9 %. The cell density is recorded to increase with AC content. The filling rate is determined to increase with the first stage holding pressure time; besides there exist specific time instants for maximum/optimum mechanical properties [9]. Ruiz et al. used polyethylene-based compounds, containing citric acid and sodium bicarbonate, as chemical blowing agents in a core-back foam injection molding investigation. The specific information in this article is the variation of pressure in the mold cavity during filling, packing, and core-back periods [10]. The sequential molding process, with one die for manufacturing multi-component products, was investigated by Park and Anh for different core-back distances. It was observed that the geometric quality/precision of the product can be satisfied with different core-back distances; however, optimization is necessary from the point of material usage amount as well. On the mechanical side, filling time and injection pressure cross-correlate to cause higher residual stress on the skin part of the product [11].

In this study, it has aimed to reduce the weight of the VUPPP structure without weakening it mechanically. Prototypes were produced using recycled two different polypropylene materials and two different chemical foaming agents to observe the effect of different NOx levels and core-back distances on the product. The core-back process is mostly associated with products with thickness values around 2.5 mm. The research's original contribution is applying the core-back process to VUPPP with thickness values in the range of 1.5-1.8 mm. The positive results demonstrated by this innovative side of the research revealed the potential in the lightening of all products that can be produced, although very thin, in the injection process using the core-back method. Within the scope of the research, geometric, weight-based, and mechanical tests were applied to the prototypes. The evaluations were presented in tabular form and discussed in detail, identifying the individual and combined roles of the effective parameters on the results.

2. Material and Method

2.1. Materials

Polypropylene is a thermoplastic polymer with a wide range of uses, from textile and food packaging to parts used in the automotive industry [12, 13]. Products created using this polymer are generally used in automotive interior parts, as this material is light, durable, and easily shaped [14 - 16].

Researchers aim to reduce the amount of waste to some extent by recycling this polymer [17, 18]. The properties of the recycled polypropylene used in this study and purchased from 2 different suppliers are shown in Table 1. Two different chemical blowing agents were used in the production of VUPPP prototypes. The reason for this is to examine the impact of diverse blowing agents on the features of the part. The properties of 2 different chemical foaming agents are shown in Table 2.

Table 1. Properties of used polypropylenes

	PP 1	PP 2
Density (g/cm^3)	0.90-0.95	0.95
Melt flow rate (230^{o}C; 2,16 kg) (g/10min)	9-14	15
Tensile stress (50 mm/min) (MPa)	≥16	20
Tensile strain at break (50 mm/min) (%)	≥40	-
Tensile modulus (1mm/min) (MPa)	≥750	900-1200
Flexural modulus (2mm/min) (MPa)	≥700	1000
Notched impact strength (Izod) (23^{o}C) kJ/m^2	≥8	10
Hardness (D-shore)	56-60	-

Table 2. Characteristics of chemical foaming agents

	CFA-X	CFA-Y
Characteristic	Endothermic composition	Endothermic composition
Types of chemical foaming	Bicarbonate	Bicarbonate
Start of activation/decomposition	160°C	140-150°C
Active content	65%	40%
Processing temperature	160-180°C	170-190°C
Dosage for injection molding	0.5-2.0%	1.0-3.0%

2.2. Methods

Conventional FIM technology is applied by short-shot injection of a mixture of polymer melt and supercritical fluid into a closed mold cavity, and the expandable melt/gas mixture forms a foam structure under reduced pressure. Meanwhile, polymer foams are widely used in various fields due to their superior properties such as lightweight, and high specific strength. Injection-compression molding is a process in which the mold is filled through controlled compression, after which the cavity pressure increases rapidly. In general, the core-back operation is a process in which the filling operation is completed, after which the cavity expands at a certain opening rate, in the direction perpendicular to the flow at a certain distance. For core-back technology, a fast pressure drop in a cavity can be acquired easily. Core-back FIM process is an advanced technology to further increase the plastic foam's weight reduction. In the core-back FIM process, When the filling phase is complete, the core side of the mold is retracted to a certain extent, creating an extra area for foaming and thus the weight reduction of the final molded foam can be particularly augmented [19 - 21]. A schematic presentation of the chemical foaming agent-assisted core-back injection process is given in Figure 2.

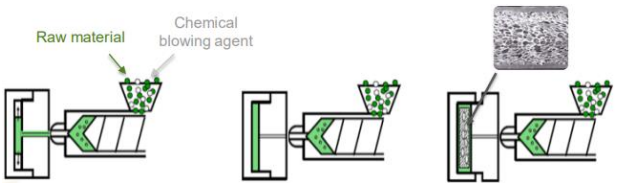

Figure 2. Schematic Presentation of Chemical Foaming Agent Assisted Core-Back Injection Process.

Although the objective of the present research is to produce some prototypes and perform weight-based and mechanical tests on them, MoldFlow simulations are also carried out to inspect the process. Figure 3 displays the result of the MoldFlow simulation executed on the part, with a thickness of 1.5 mm, to evaluate the filling behavior. As Figure 3(a) displays the thickness distribution of the part, the elapsed time for the melt to fill different sections of the mold is shown in Figure 3(b). Moldflow simulation shows that there is no problem in filling with a 1.5mm thick part with current gate numbers.

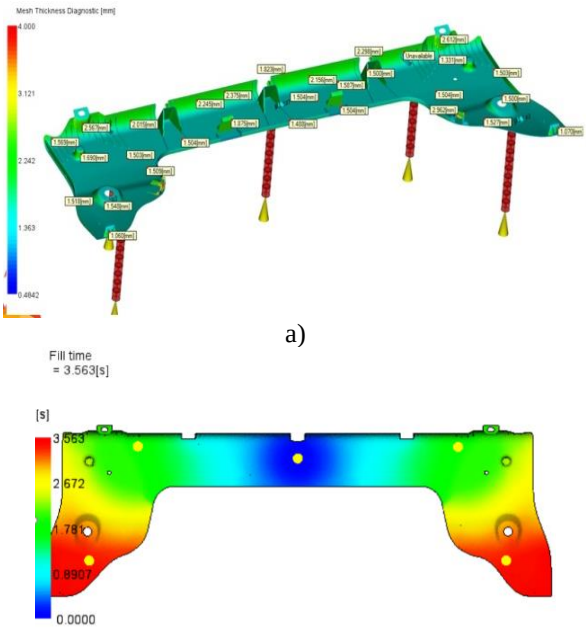

a)

b)

Figure 3. a) The thickness distribution of the part, b) the elapsed time for the melt to fill different sections of the mold

Prototypes are produced with thickness values of 1.5, 1.8, 2.0, and 2.5 mm. The prototype plaque mold, with different thicknesses, available in the NOVARES production area is shown in Figure 4.

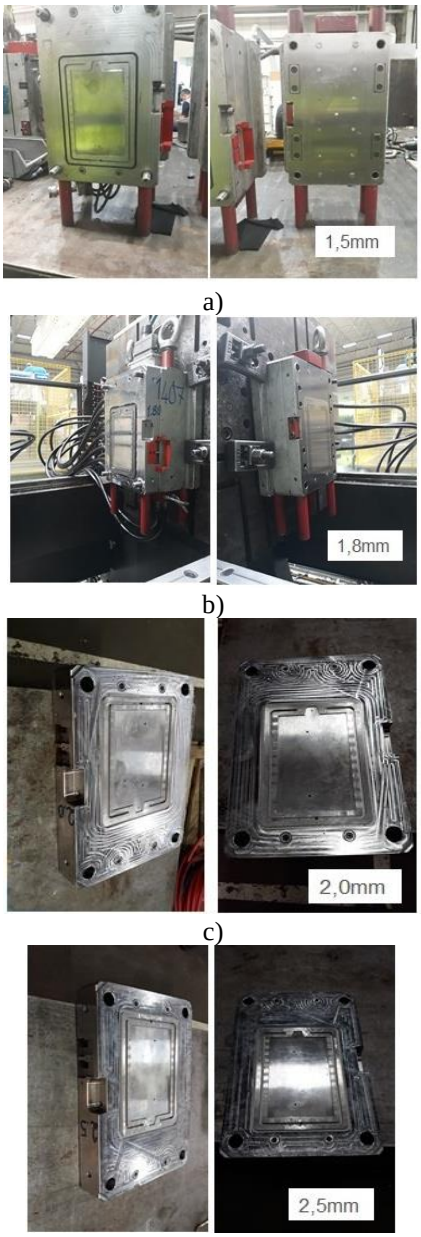

a)
b)
c)
d)

Figure 4. Prototype Plaque Mold with Different Thickness a) 1.5 mm b)1.8 mm c) 2.0 mm d)2.5 mm

Both of the used CFA types contain bi-carbonate type sort active material with 40 and 60% portions. Besides the CFA types react in the endothermic way, where reaction formulations are given in Eq. (1-5).

$$CFA(endo) \xrightarrow{+\Delta E} CO_2 + H_2O + inorganic\ subprod. \quad (1)$$

$$2NaHCO_3 \rightarrow Na_2CO_3 + H_2O + CO_2 \quad (2)$$

$$C_6H_8O_7 \rightarrow C_6H_6O_6 + H_2O \quad (3)$$

$$C_6H_6O_6 \rightarrow C_5H_6O_4 + CO_2 \quad (4)$$

$$C_6H_8O_7 + 3NaHCO_3 \rightarrow Na_3C_6H_5O_7 + 3H_2O + 3CO_2 \quad (5)$$

Tensile and impact tests were applied to the produced prototypes. The prototypes were cut according to the TS EN ISO 527 standard for the water jet tensile test and the TS EN ISO 180/A1 standard for the impact tests and tested in accordance with these standards.

3. Results and Discussion

Laboratory tests are performed on the prototypes which are produced with different recycled polypropylene materials, chemical foaming agents, NOx levels, and core-back distances. Evaluations and discussions are based on geometrical, interior structure of plaques, weight-based and mechanical results.

3.1. Effects of CFA

The variants in this data set are the CFA (CFA-X, CFA-Y) and the thickness of the mold (1.5, 1.8, 2.0 mm). Moreover, the CFA adding ratio is 1.5% and the cavity temperature is 37oC stable, the main target of this injection trial is CFA types effect in different thicknesses. For the CFA types CFA-X and CFA-Y, according to the results, the CFA-X weight reduction ratio seems more than CFA-Y for each thickness value. The corresponding tensile strength at yield was 19.69 and 20.99 MPa, the tensile strength at break was 17.40 and 16.29 MPa, and the tensile modulus values were 1201 and 1221 MPa respectively. From the point of strains, the related data for tensile strain at yield were 6.05 and 5.18%, and tensile strain at break was 31.23 and 28.32% respectively. These data as a whole indicate that CFA-X causes higher weight reduction, which can be associated with the excess content ratio of CFA-X with respect to CFA-Y. As a result, the higher weight reduction can be attributed to more bubbles with bigger cell diameters in the VUPPP volume. In return, the mechanical properties are comparably poorer when compared to those of the CFA-Y case, with lower tensile strength values and higher strain data. Table 3 presents the results of the experiments that were carried out on the prototypes which were produced by PP1.

As the weight reduction is less with CFA-X, the mechanical properties are recorded to be superior to those of CFA-Y. Such that tensile strength at yield was 23.63 and 22.4 MPa, tensile strength at break was 21.31 and 17.86 MPa, and the tensile modulus values were 1312 and 1296 MPa for CFA-X and CFA-Y respectively. From the point of strains, the related data for tensile strain at yield were 6.22 and 5.21%, and tensile strain at break was 19.47 and 22.65% respectively.

Table 3. Effects of CFA Type on the Weight and Mechanical Properties of Prototypes.

Material Descriptions	**Values According to Scenarios**					
Started Thickness (mm)	2.0	2.0	1.8	1.8	1.5	1.5
Final Thickness (mm)	2.0	2.0	1.85	1.85	1.54	1.53
Core-Back (mm)	0	0	0.05	0.05	0	0.03
Theoretical Mass (acc to final thick.) (g)	50.64	50.64	46.84	46.84	38.99	38.74
Measured Mass (g)	46.74	46.21	43.00	43.50	38.10	38.29
Weight Reduction (%)	7.7	8.7	8.2	7.1	2.3	1.2
CFA	CFA-X	CFA- Y	CFA-X	CFA- Y	CFA-X	CFA- Y
CFA adding % (w/w)	1.5	1.5	1.5	1.5	1.5	1.5
Mechanical Test Result						
Tensile Strength at Yield / Tensile stress (50mm/min) (MPa)	17.75	19.58	19.69	20.99	23.63	22.4
Tensile Strain at Yield (50 mm/min) (%)	5.88	5.15	6.05	5.18	6.22	5.21
Tensile Strength at Break / (50 mm/min) (MPa)	16.49	17.72	17.40	16.29	21.31	17.86
Tensile Strain at Break (50 mm/min) (%)	42.99	33.99	31.23	28.32	19.47	22.65
Tensile Modulus (1 mm/min) (MPa)	1090	1146	1201	1221	1312	1296
Charpy Impact no notched (23°C)						
1J hammer (kJ/m^2)	No break	No break	No break	No break	No break	No break
5J hammer (kJ/m^2)	No break	No break	No break	No break	No break	No break

Table 4. Effects of NOx usage on the weight and mechanical properties of prototypes.

Material Descriptions	**Values According to Scenarios**			
Started Thickness (mm)	1.8	1.8	1.8	1.8
Final Thickness (mm)	1.85	1.8	1.88	189
Core Back (mm)	0.05	0	0.08	0.09
Theoretical Mass (acc to final thick.) (g)	46.8373	45.5715	47.5969	47.8500
Measured Mass (g)	43	43.8	42.24	43.3
Weight Reduction (%)	8.2	3.9	11.3	9.5
CFA ID	CFA- X	CFA-X	CFA- X	CFA- X
CFA % Adding	1.50%	1.50%	1.50%	1.50%
NO_X %	No	1%	No	1%
Mechanical Test Result				
Tensile Strength at Yield / Tensile stress (50 mm/min) (MPa)	19.69	21.60	24.21	23.66
Tensile Strain at Yield (50 mm/min) (%)	6.05	5.28	7.62	7.86
Tensile Strength at Break/(50 mm/min) (MPa)	17.40	14.51	21.14	21.52
Tensile Strain at Break (50 mm/min) (%)	31.23	31.26	34.84	32.05
Tensile Modulus (1 mm/min) (MPa)	1201	1078	1071	991
Charpy Impact no notched (23°C)				
1J hammer (kJ/m2)	No break	No break	25.5	No break
5J hammer (kJ/m2)	No break	No break	-	No break

3.2. Effect of NOx addition

Effects of NOx addition are also investigated and the evaluated results are given in the tabulated form in Table 4. The expectation in NOx addition is to optimize the variation of mechanic property variations of the recycled material in every individual product. The material and CFA types used in these scenario sets were selected to be PP1 and CFA-X respectively. The starting thicknesses were always 1.8 mm, core-back distances were in the range of 0-0.09 mm and the cavity temperatures were around 36-38 ºC. In the case with the core-back distance of 0.09 mm, NOx was applied by 1%; the weight reduction attained here was 9.5%. However, in the comparably lower core-back distance of 0.08 mm, without NOx addition (0%) the weight reduction was higher with the specific value of 11.3%. These results indicate the suppressive effect of NOx on weight reduction. From the mechanical testing

perspective, NOx addition does not seem to have an inspectable role in mechanical properties. Such that tensile strength at yield was 23.66 and 24.21 MPa, tensile strength at break was 21.52 and 21.14 MPa, the tensile modulus values were 991 and 1071 MPa for with (1.5%), and without NOx addition (0%) respectively. From the point of strains, the related data for tensile strain at yield were 7.86 and 7.66%, and tensile strain at break was 32.05 and 34.84% respectively.

Table 5. Effects of material type on the weight and mechanical properties of prototypes.

Material Descriptions	**PP1**	**PP2**
Started Thickness (mm)	1.8	1.8
Final Thickness (mm)	1.85	1.85
Core Back (mm)	0.05	0.05
Theoretical Mass (acc to final thick.) (g)	46.8373	46.8373
Measured Mass (g)	43	42.24
Weight Reduction (%)	8.2	9.8
CFA ID	CFA -X	CFA -X
Mechanical test result		
Tensile Strength at Yield/Tensile stress (50 mm/min) (MPa)	19.69	24.21
Tensile Strain at Yield (50 mm/min) (%)	6.05	7.62
Tensile Strength at Break / (50 mm/min) (MPa)	17.40	21.14
Tensile Strain at Break (50 mm/min) (%)	31.23	34.84
Tensile Modulus (1 mm/min) (MPa)	1201	1071
Charpy Impact no notched (23°C)		
1J hammer (kJ/m^2)	No break	25.5
5J hammer (kJ/m^2)	No break	-

Table 6. Effects of core-back application on the weight and mechanical properties of prototypes.

Material Descriptions	**Values According to Scenarios**							
Started Thickness (mm)	1.56	1.5	1.5	1.8	1.8	1.8	1.8	1.8
Final Thickness (mm)	1.56	1.54	2.04	1.8	1.8	1.85	2.03	2.2
Core Back (mm)	0	0	0.54	0	0	0	0.23	0.4
Theoretical Mass (acc to final thick.) (g)	41.26	38.98	51.39	45.57	45.57	46.83	51.39	55.69
Measured Mass (g)	42.51	38.10	47.81	45.57	43.8	43	44	43.2
Weight Reduction (%)	0.0	2.3	6.97	0.0	3.9	8.2	14.4	22.4
CFA adding% (w/w)	0	1.5	1.5	0	1.5	1.5	1.5	1.5
Mechanical test result								
Tensile Strength at Yield / Tensile stress (50 mm/min) (MPa)	25.43	23.63	22.98	24.3	21,60	19.69	19.53	18.84
Tensile Strain at Yield (50 mm/min) (%)	5.91	6.22	8.09	5.7	5.28	6.05	6.41	6.98
Tensile Strength at Break (50 mm/min) (MPa)	14.61	21.31	19.59	10.05	14.51	17.40	17.51	16.98
Tensile Strain at Break (50 mm/min) (%)	28.77	19.47	20.32	31.5	31.26	31.23	30.87	33.52
Tensile Modulus (1 mm/min) (MPa)	1340	1312	1251	1219.9	1078	1201	892	842
Charpy Impact no notched (23°C)								
1J hammer (kJ/m^2)	N/A	N/A	N/A	No break	No break	No break	18,86	16,77
5J hammer (kJ/m^2)	N/A	N/A	16,9	No break	No break	No break	No break	No break

3.4. Effect of Core-back Application

The starting thicknesses were in the range of 1.5-1,8 mm and the core-back distances were applied within the limits of 0.5 mm. The increase of air voids formed after this process in Figure 5 can be seen clearly.

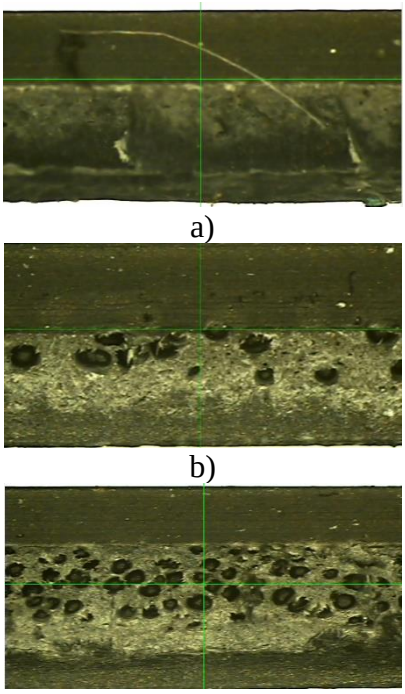

Figure 5. Prototype cross-section images of different thicknesses a) 1.5 mm thickness without CFA b) 1.8 mm thickness with CFA c) 2.2 mm thickness with CFA + 0.5mm core-back

The CFA was CFA-X; its adding quantity was 1.5%. Besides, the cavity temperature is set at 25 ºC. The complete set of results indicated a rise in weight reduction with the core-back application. Similarly, CFA-X addition also promoted weight reduction. Cavity temperature appears to limit weight reduction. An increase in weight reduction can be said to be an indicator for loss of mechanical durability with lower property data. Table 6 displays the variation of weight reduction and mechanical property data of 8 scenarios where the primary material was selected as PP1. In addition, tensile test data and graphs of the 5 samples produced for each scenario are also given in Figure 6. The tensile test strength values given in Table 6 are the average values of the data taken from 5 samples. Table 6 and Figure 5 shows that the core-back has a significant effect on increasing the number of air voids and thus the weight reduction ratio. The important issue to be considered is the mechanical properties of polypropylene. After core-back, the tensile stress and strain modulus values decreased for each sample, but this was a negligible decrease. The highest weight reduction rate (22.4%) was observed in the 2.2 mm thick sample with a core back distance of 0.4 mm. While the tensile strength at the yield value of this sample was 18.84 MPa, the tensile strain at the yield value was 6.98%. As the initial thickness increases, the core back distance may increase, and weight reduction can be achieved without affecting the mechanical strength much.

4. Conclusion

An experimental investigation of geometric and mechanical results of the chemical foaming agent-assisted core-back injection process is reported for different suppliers' recycled polypropylene material, chemical foaming agents, NOx levels, core-back distances, and cavity temperatures. The main outcomes of the computations can be summarized as follows;

- The core-back process is successfully applied to VUPPP with thickness values down to 1.5 mm.
- CFA-X, when compared to CFA-Y, causes higher weight reduction, which is return can be attributed to more bubbles with bigger cell diameters in the VUPPP volume. In return, the mechanical properties are comparably poorer, with lower tensile strength values and higher strain data.
- NOx addition does not seem to have an inspectable role in mechanical properties.
- The weight reduction in the PP2 material came up to be superior to that of PP1. On the mechanical side, PP2 was also evaluated to be more durable than PP1.
- The complete set of evaluated results indicated a rise in weight reduction with the core-back application.
- An increase in weight reduction can be said to be an indicator for loss of mechanical durability with lower property data.

CRediT authorship contribution statement

Yasemin Gültekin: Methodology, Resources, Visualization, **Mustafa Atakan Akar:** Investigation, Writing - original draft, Supervision, **Anıl Altındağ:** Investigation, Methodology, Conceptualization, **Doğukan Duran:** Investigation, Methodology, Conceptualization, **Umut Kumlu:** Visualization, Writing - original draft, Writing - review& editing.

Declaration of competing interest

The authors declare that they have no known competing financial interests or personal relationships that could have appeared to influence the work reported in this paper.

Results:

Nr	Et MPa	σ x N/mm²	σM MPa	εM %	σB MPa	εB %	L0 mm
1	1310,00	14,52	25,31	5,92	12,96	32,54	75,18
2	1360,11	14,44	25,30	5,90	14,80	32,68	75,09
3	1395,98	13,75	25,66	5,69	15,36	28,46	75,09
4	1310,30	15,33	26,76	6,15	13,37	29,83	75,13
5	1326,11	14,38	25,16	5,90	16,55	20,32	75,11

Series graphics:

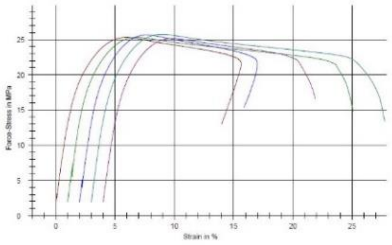

a)

Results:

Nr	Et MPa	σ x N/mm²	σM MPa	εM %	σB MPa	εB %	L0 mm
1	1305,97	15,17	24,09	5,49	22,26	17,37	75,00
2	1318,61	14,67	23,32	5,95	21,26	19,78	75,04
3	1275,63	15,10	24,22	5,93	22,15	19,04	74,98
4	1315,07	14,17	22,73	5,64	19,96	18,48	75,02
5	1345,73	13,46	23,78	6,11	20,88	22,69	75,08

Series graphics:

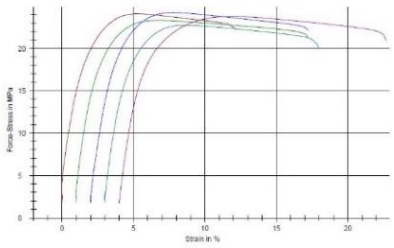

b)

Results:

Nr	Et MPa	σ x N/mm²	σM MPa	εM %	σB MPa	εB %	L0 mm
1	1239,37	13,35	22,45	7,68	19,43	18,65	75,09
2	1327,70	13,22	23,03	8,40	18,04	23,59	75,07
3	1246,86	13,84	22,84	7,64	18,67	19,66	75,09
4	1246,78	13,17	23,33	8,29	22,02	15,78	75,07
5	1194,98	13,38	23,23	8,42	18,87	24,04	75,09

Series graphics:

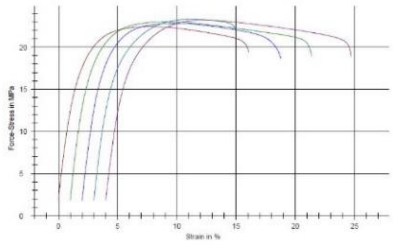

c)

Results:

Nr	Et MPa	σ x N/mm²	σM MPa	εM %	σB MPa	εB %	L0 mm
1	1360,85	17,42	26,85	6,11	9,32	45,46	75,05
2	1326,93	17,29	26,34	6,25	9,25	27,90	75,08
3	1302,51	17,62	26,29	6,10	7,70	39,52	75,06
4	1206,67	15,33	26,17	5,72	9,42	37,76	75,09
5	1341,63	16,86	25,67	6,21	20,75	18,39	75,02

Series graphics:

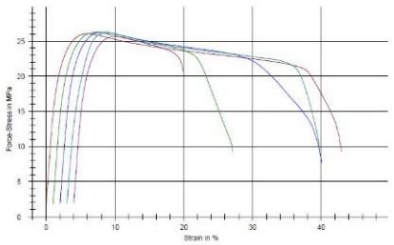

d)

Results:

Nr	Et MPa	σ x N/mm²	σM MPa	εM %	σB MPa	εB %	L0 mm
1	1013,56	17,56	22,34	5,34	16,75	26,05	75,03
2	1046,23	16,16	21,84	5,27	11,81	27,36	75,05
3	1098,52	15,38	21,70	5,22	18,05	36,86	75,02
4	1158,82	14,83	21,37	5,20	17,28	34,22	75,00
5	1073,97	14,32	20,74	5,37	8,69	31,87	74,97

Series graphics:

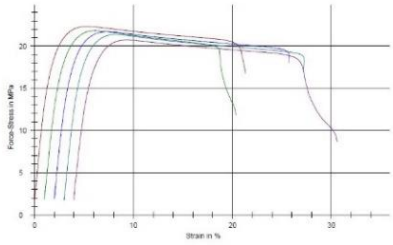

e)

Results:

Nr	Et MPa	σ x N/mm²	σM MPa	εM %	σB MPa	εB %	L0 mm
1	1243,87	11,34	19,82	5,46	17,45	31,23	75,02
2	1227,13	11,29	19,33	5,88	17,17	32,06	75,10
3	1264,59	11,17	19,47	5,84	16,69	36,07	75,11
4	1221,21	11,98	19,92	6,09	18,51	19,79	75,09
5	1048,53	12,26	19,92	7,01	17,18	37,99	75,11

Series graphics:

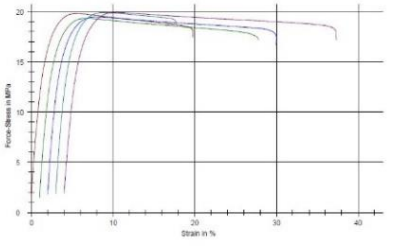

f)

Results:

Nr	Et MPa	σ x N/mm²	σM MPa	εM %	σB MPa	εB %	L0 mm
1	867,64	15,64	20,34	5,62	16,90	37,37	74,98
2	978,10	14,11	19,95	6,12	18,19	28,06	75,10
3	974,58	13,32	19,61	6,09	18,23	30,47	75,09
4	918,78	12,80	19,09	7,18	17,90	29,32	75,13
5	690,89	11,63	18,68	6,77	17,34	29,10	75,14

Series graphics:

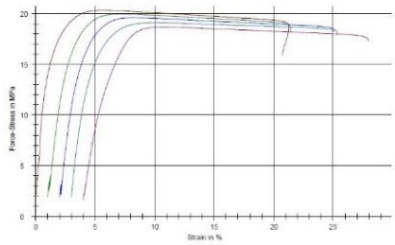

g)

Results:

Nr	Et MPa	σ x N/mm²	σM MPa	εM %	σB MPa	εB %	L0 mm
1	831,04	13,65	18,86	6,83	16,93	40,07	75,13
2	804,58	13,27	18,71	7,96	17,39	34,94	75,13
3	870,96	13,34	18,95	6,61	16,72	30,41	75,13
4	855,26	12,87	18,68	7,00	15,88	32,61	75,12
5	849,80	13,36	19,02	6,50	17,55	29,55	75,13

Series graphics:

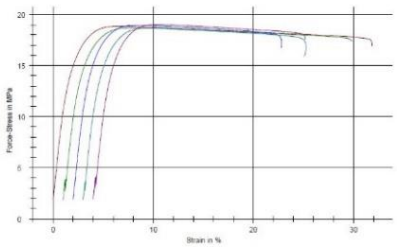

h)

Figure 6. Tensile test data and graphics of specimens

Acknowledgement

The authors would like to thank the TÜBİTAK TEYDEB (3190913) for financial support.

5. References

1. Akar M. A., Tosun A. T., Yel F., Kumlu U., "The Usage of Natural Fibers for Automotive Applications", Macromolecular Symposia, 404, 1, 1–3 2022.
2. Liu B., Gu J., Jiang T., Deng R., Yang J., Zeng X., Zhang C., He L., Gong W., "Designer petals shape ZnO nanoparticles as nucleating agents: Verification the mechanism of cavity nucleation in the polymer for foaming", Polymer Testing, 104, 107398, 1-10, 2021.
3. Wang L., Okada K., Hikima Y., Ohshima M., Sekiguchi T., Yano H., "Effect of cellulose nanofiber (CNF) surface treatment on cellular structures and mechanical properties of polypropylene/CNF nanocomposite foams via core-back foam injection molding", Polymers, 11, 2, 1–18, 2019.
4. Bai T., Dong B., Xiao M., Liu H., Wang N., Wang Y., Wang C., Liu C., Cao W., Zhang J., Ma Y.,Guo Z., "Polystyrene Foam with High Cell Density and Small Cell Size by Compression-Injection Molding and Core Back Foaming Technique: Evolution of Cells in Cavity", Macromolecular Materials and Engineering, 303, 9,1–11, 2018.
5. Wu H., Zhao G., Wang G., Zhang W., Li Y., "A new core-back foam injection molding method with chemical blowing agents", Materials and Design, 144, 331–342, 2018.
6. Muñoz-Pascual S., Saiz-Arroyo C., Vananroye A., Moldenaers P., Rodriguez-Perez M. A., "Effect on the Impact Properties of Adding Long-Chain Branched Polypropylene in Polypropylene-Polyolefin Elastomer Cellular Polymers Produced by Core-Back Injection Molding", Macromolecular Materials and Engineering, 306, (2000728), 1–17, 2021.
7. Jiang T., Zhang H., Zeng X., Zhang C., Gong W., He L., "The effect of injection process for microcellular foaming on the cell morphology and surface quality of Polyamide 6", Materials Research Express, 8, 4, 1-11, 2021.
8. Ishikawa T., Ohshima M., "Visual observation and numerical studies of polymer foaming behavior of polypropylene/carbon dioxide system in a core-back injection molding process", Polymer Engineering & Science, 51, 8, 1617–1625, 2011.
9. Wu H., Zhao G., Wang J., Wang G., Zhang W., "Effects of process parameters on core-back foam injection molding process", Express Polymer Letters, 13, 4, 390–405, 2019.
10. Ruiz J. A. R., Vincent M., Agassant J-F, "Numerical Modeling of Bubble Growth in Microcellular Polypropylene Produced in a Core-Back Injection Process Using Chemical Blowing Agents", International Polymer Processing, 31, 1, 26–36, 2016.
11. Park H. S., Anh D. B. H., "A new approach for molding multi component parts", International Journal of Precision Engineering and Manufacturing, 11, 2, 291–297, 2010.
12. Ozunlu B. G., Guner F. S., "An Industrial Case for Polypropylene Nanocomposite Foams : Lightweight, Soundproof Exterior Automotive Parts", Polymers(Basel), 14, 1192, 1–19, 2022.
13. Park J-M., Kim P-G., Jang J-H., Wang Z., Hwang B-S., DeVries K. L., "Interfacial evaluation and durability of modified Jute fibers/polypropylene (PP) composites using micromechanical test and acoustic emission", Composites Part B: Engineering, 39, 6, 1042–1061, 2008.
14. Cho D., Seo J. M., Lee H.S , Cho C. W., Han S. O., Park W. H., "Property improvement of natural fiber-reinforced green composites by water treatment", Advanced Composite Materials: The Official Journal of the Japan Society of Composite Materials, 16, 4, 299–314, 2007.
15. Hariprasad K., Ravichandran K., Jayaseelan V., Muthuramalingam T., "Acoustic and mechanical characterisation of polypropylene composites reinforced by natural fibres for automotive applications", Journal of Materials Research and Technology, 9, 6, 14029–14035, 2020.
16. H S N., S S., Kakkeri S., R S., "Development and mechanical testing of natural fibre reinforced polypropylene resin hybrid composite", Advances in Materials and Processing Technologies, 8, 2, 790-801, 2021.
17. Ladhari A., Kucukpinar E., Stoll H., Sängerlaub S., "Comparison of Properties with Relevance for the Automotive Sector in Mechanically Recycled and Virgin

Polypropylene", Recycling, 6, 76, 1–11, 2021.
18. Bunjes A., Arndt J., Geertz G., Barton B., "Characterization and chemometric modelling of mechanically recycled polypropylene for automotive manufacturing", Polymer, 249, 124823, 1–10, 2022.
19. Kim D., Hikima Y., Ohshima M., "Millefeuille-like cellular structures of biopolymer blend foams prepared by the foam injection molding technique", Journal of Applied Polymer Science, 139, 14, 1–14, 2022.
20. Taki K., Menale M., Pisante G., Di Maio E., "A design tool for core-back timing in foam injection molding", Journal of Applied Polymer Science, 139, 45, 1–10, 2022.
21. Weng Z., Ren Q., Wu M., Zhu X., Li W., Wang L., Zheng W., "Lightweight and tough PVDF foams via high-pressure foam injection molding with core-back operation", Polymer Engineering & Science, 62, 11, 3543–3452, 2022.

e-ISSN: 2146 - 9067

International Journal of Automotive Engineering and Technologies

journal homepage:
https://dergipark.org.tr/en/pub/ijaet

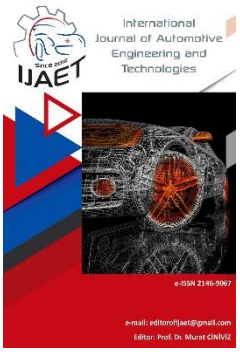

Original Research Article

Experimental investigation of heat transfer performance of different nanofluids in engine cooling system

Tahsin Yüksel[1,*], Abdullah Kapıcıoğlu[2]

[1, *] Mechatronic Engineering Department, Faculty of Technology, Sivas Cumhuriyet University, Sivas, 58050, Türkiye.
[2] Manufacturing Engineering Department, Faculty of Technology, Sivas Cumhuriyet University, Sivas, 58050, Türkiye.

ARTICLE INFO

Orcid Numbers
1. 0000-0003-3238-9113
2. 0000-0003-2982-0312

Doi: 10.18245/ijaet.1296361

* Corresponding author

tyuksel@cumhuriyet.edu.tr

Received: May 12, 2023
Accepted: Nov 12, 2023

Published: 31 Dec 2023

Published by Editorial Board Members of IJAET

ABSTRACT

Cooling systems are needed for internal combustion engines to operate efficiently. The fluid traditionally used to transfer heat in cooling systems is a mixture of ethylene glycol (EG) and water (W). These fluids generally exhibit an effect that extends the operating temperature range and limits the heat output. On the other hand, nanofluids are known to increase the thermal capacity of liquid suspensions and have been studied in many experimental and numerical studies. This study examines the effects of nanofluids instead of currently used EG-Water on an actual vehicle. Three different nanofluids (TiO_2, Al_2O_3, and SiO_2) were used, and the concentration ratios of these fluids were determined as 0.1% and 0.2%. A real vehicle engine cooling system with a volume of 1400 cm^3 operating at an average of 2000 rpm was used in the studies. Fluids that are widely studied in the literature were taken into account when selecting nanofluids. The results showed that SiO_2 achieved the highest performance, with an increase of 15% compared to the base fluid. On the other hand, it was observed that increasing the concentration value of TiO_2 exhibited a lower performance increase compared to other nanofluids. Finally, it has been observed that the operating temperature range of nanofluids affects.

Keywords: Cooling system; Experimental; Heat transfer rate; Internal combustion engine; Nanofluid

1. Introduction

The rapid development and change in the automotive industry have led to increased thermal loads and hence the need for higher cooling rates [1]. If the cooling system cannot provide sufficient cooling to keep the engine within a well-defined temperature range, performance and durability will decrease, and emissions will increase. Although increasing the radiator size is a solution here, this causes an increase in the vehicle's weight and, therefore, more fuel consumption [2]. Considering today's environmental concerns, the costs of increased fuel consumption and the additional emission caused by excessive fuel consumption are highly undesirable [3]. Traditional methods, such as the development of fins and the addition of microchannels, have already been extended to their limits [4].

On the other hand, ethylene glycol (EG)-Water (W) mixtures are used as heat transfer fluid in engines [1]. Mixing EG with the engine coolant is an indispensable solution for using vehicles in all climatic conditions. However, heat transfer is limited in heating-cooling processes using traditional fluids, such as EG-W, due to the fluids' limited thermal properties [5]. Therefore, improving the thermal properties of the heat transfer fluid can be offered as a solution since the radiator design parameters have reached their limits [6]. In this context, it is a helpful approach to use nanofluid (NF) as a heat transfer fluid in cooling systems [7]. The literature has reported that the use of nanofluids in different areas, such as ground heat exchangers [8], solar thermal collectors [9], or mini-duct coolers [10], gives successful results. Nanomaterials have even been successfully applied to coat radiator fins [11]. Investigating the use of NFs in automobile radiators is given in Table 1. These studies have observed increased heat transfer using NFs at different mixing ratios.

As seen from the studies given in Table 1, it can be said that using nanofluids in radiators increases the heat transfer rate. Thanks to the increase in heat transfer rate, the required cooling amount can be achieved with a smaller radiator [12]. More compact and lighter radiators provide both an increase in vehicle performance and a decrease in fuel consumption by decreasing weight [5, 13, 14]. The concentration ratio of nanoparticles mixed in the heat transfer fluid also affects the heat transfer. Studies carried out by adding nanoparticles at different volumetric concentrations into EG-W have indicated that as the density of nanoparticles increases, the volumetric concentration of nanoparticles increases; however, as the temperature increases, the thermal conductivity decreases [15]. Furthermore, studies have concluded that the heat transfer performance of the radiator in the heat transfer fluid is significantly increased with the increase in nanoparticle concentration [16, 17].

Table 1. Heat transfer studies in automobile radiators where nanofluids are used.

Researchers (Year)	**Nanofluid**	**(% vol.)**	**Findings**
Said et al. [4] 2019	Al_2O_3 – (EG-W) (50:50) TiO_2 - (EG-W) (50:50)	0.05 - 0.3	It has been found that the thermal conductivity of 0.3% Al_2O_3 NF was higher than TiO_2 NF.
Tijani and Sudirman [5] 2018	Al_2O_3 – (EG-W) (50:50) CuO – (EG-W) (50:50)	0.05 - 0.3	The heat transfer performance of CuO NF is the highest.
Jadar et al. [12] 2017a	MWCNT – (DI-W)	0.1	An increase in heat transfer performance of 45% has been obtained with the use of NF.
Peyghambarzadeh et al. [13] 2011	Al_2O_3 – W Al_2O_3 – EG (0, 10, 20 EG)	0 - 1 0 - 1	The heat transfer increase obtained with NFs has been approximately 40%.
Hussein et al. [14] 2014	SiO_2 – W	1 - 2.5	It has been determined that using NF increases heat transfer performance by up to 50%.
Tadepalli et al. [15] 2018	Al_2O_3, SiO_2, SiC, TiO_2, CuO - Liquid Oxygen	1 - 5	It has been found that the increase in temperature decreases the thermal conductivity, while the increase in volumetric concentration increases the thermal conductivity.
Subhedar et al. [16] 2018	Al_2O_3 – (EG-W) (50:50)	0.2 - 0.8	It has been found that using NF improves heat transfer performance even in the lowest amount (0.2%).
Ahmed et al. [17] 2018	TiO_2– W	0.1 - 0.3	It has been found that the increase in the volumetric concentration of NF positively affected the average heat transfer coefficient.
Peyghambarzadeh et al. [18] 2011	Al_2O_3 – W	0.1 - 1	45% heat transfer increase has been obtained with Al_2O_3 NF.
Elias et al. [19] 2014	Al_2O_3 – (EG-W) (50:50)	0 - 1	The volumetric increase of NF has increased the density, viscosity, and thermal conductivity values.
Nieh et al. [20] 2014	Al_2O_3 – (EG-W) (50:50) TiO_2 - (EG-W) (50:50)	0.2	It has been determined that TiO_2 NF has higher thermal conductivity than Al_2O_3.
M'hamed et al. [21] 2016	MWCNT – (EG-W) (50:50)	0.1 - 0.5	The increase in volumetric concentration has affected the average heat transfer increase in direct proportion.
Li et al. [22] 2016	SiC - (EG-W) (40:60)	0 - 0.5	The thermal conductivity of SiC NF is higher compared to the base fluid.
Elsebay et al. [23] 2016	Al_2O_3 – W CuO – W	0 - 7	It has been found that the heat transfer rate in the radiator can be increased by increasing the NF addition rate.
Elsaid [24] 2019	Al_2O_3 - (EG-W) (0:100, 10:90, 20:80)	0 - 0.2	It has been found that Co_3O_4 NF has higher thermal performance than Al_2O_3 NF.
Muruganandam and Mukesh Kumar [25] 2020	MWCNT - W	0.1 - 0.5	The mechanical efficiencies of NFs are higher than water.
Mukherjee et al. [26] 2020	Al_2O_3 – W TiO_2 - W	0.125 - 1.5	Al_2O_3 NFs have provided better thermal conductivity and transient heat conduction performance.

Table 2. Properties of nanoparticles.

Properties	TiO_2	Al_2O_3	SiO_2
Colour	White	White	White
Particle size (nm)	25-45	28	5-20
Purity	99.9%	99.99%	99.99%
Particle morphology	Almost spherical	Almost spherical	Almost spherical
Dissolution in water	Indissoluble	Indissoluble	Indissoluble
Density (gr/cm^3)	4.23	3.5 – 3.9	2.3 [4, 27, 30]
Thermal conductivity (W/mK)	8.95	40	1.34 – 1.4 [4, 27, 30]
Specific heat (J/kgK)	686	765	745 [4, 27, 30]

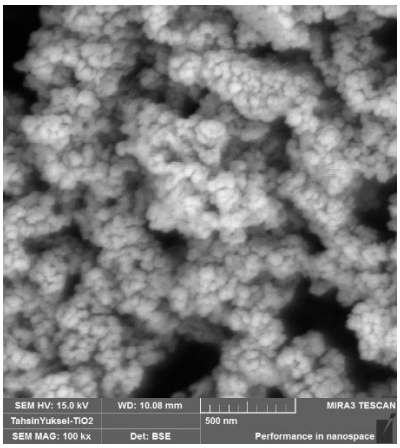

a) TiO_2

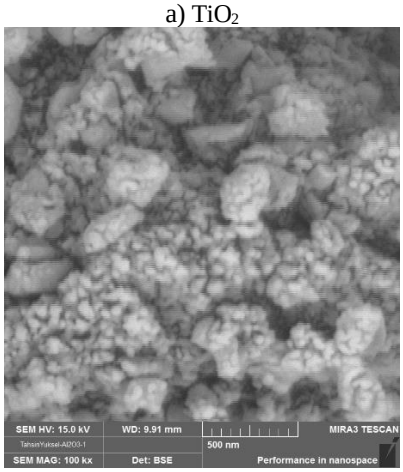

b) Al_2O_3

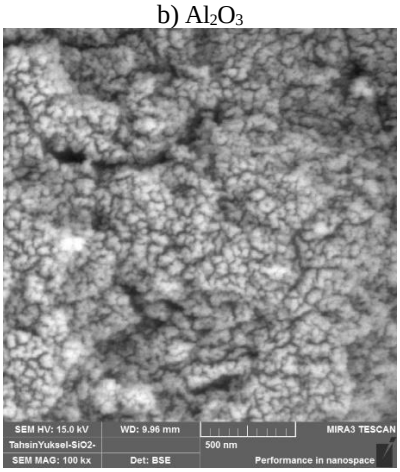

c) SiO_2

Fig. 1. SEM images of TiO_2, Al_2O_3, and SiO_2

However, it should be noted that the studies mentioned above were carried out in a laboratory environment. At this stage, it should not be ignored that there will be differences between the heat transfer values obtained from studies using only vehicle radiators in laboratory environments and the actual operating conditions obtained using a vehicle engine.

In order to evaluate the overall performance of a system, the geometry considered in the experiment and the system's geometry must be well-matched. When comparing the experimental and simulation results, even open or closed thermostats can cause large deviations in many parameters [31]. Although considering only a specific part, such as the radiator, gives us valuable results, it may be insufficient to reveal the performance values of the entire system. Examining only the radiator side causes the flow in areas such as water jackets, ducts, or connecting pipes inside the engine to be ignored. Using an internal combustion engine and existing cooling system, heat transfer values will show different values compared to laboratory conditions using conventional heat transfer fluids and NFs. The results calculated and found in the literature should be verified by applying all these results to real engines. In addition, it is aimed to form a basis for the numerical studies to be carried out thanks to this study. This study investigated the performance of nanofluid-assisted coolant in a vehicle cooling system. The examined system has all the cooling system components that a vehicle should have. Three different NFs (TiO_2, Al_2O_3, and SiO_2) prepared in different volumetric fractions (0.1% and 0.2%) were used in the study.

2. Materials and Methods

2.1. Nanofluids

When comparing the cooling system's heat transfer performance, the preferred 1:1 mixture of EG-W as the base fluid to prevent freezing in

cold climate conditions (approximately freezing point -34 °C, approximately boiling point 107 °C [32]) was used. NFs were prepared by mixing nanoparticles in volumes of 0.1% and 0.2% into the mixture. The nanodispersions used in the study (TiO_2, Al_2O_3, and SiO_2) were purchased in 100 ml ready-made packages prepared by the Nanography company. Sodium Dodecyl Sulphate (SDS) has been used as a surfactant for TiO_2 and Al_2O_3 NFs used in the study.

No surfactant has been used for SiO_2. Later, NFs were prepared by using an ultrasonic mixer to prevent sedimentation and agglomeration. The technical properties of the specified NFs are given in Table 2. The SEM images obtained as a result of their examination in Sivas Cumhuriyet University Advanced Technology Research and Application Center Laboratories are given in Fig. 1.

Eq. (1) was used to calculate the volume percentage of NFs and the volume of the base fluid. The lower concentration was obtained by adding the base fluid pre-calculated using Eq. (2). [22,24,27]:

$$\varphi = \frac{m_n / \rho_n}{m_n / \rho_n + m_f / \rho_f} x100 \quad (1)$$

$$\Delta V = V_2 - V_1 = V_1 (\varphi_1 / \varphi_2 + 1) \quad (2)$$

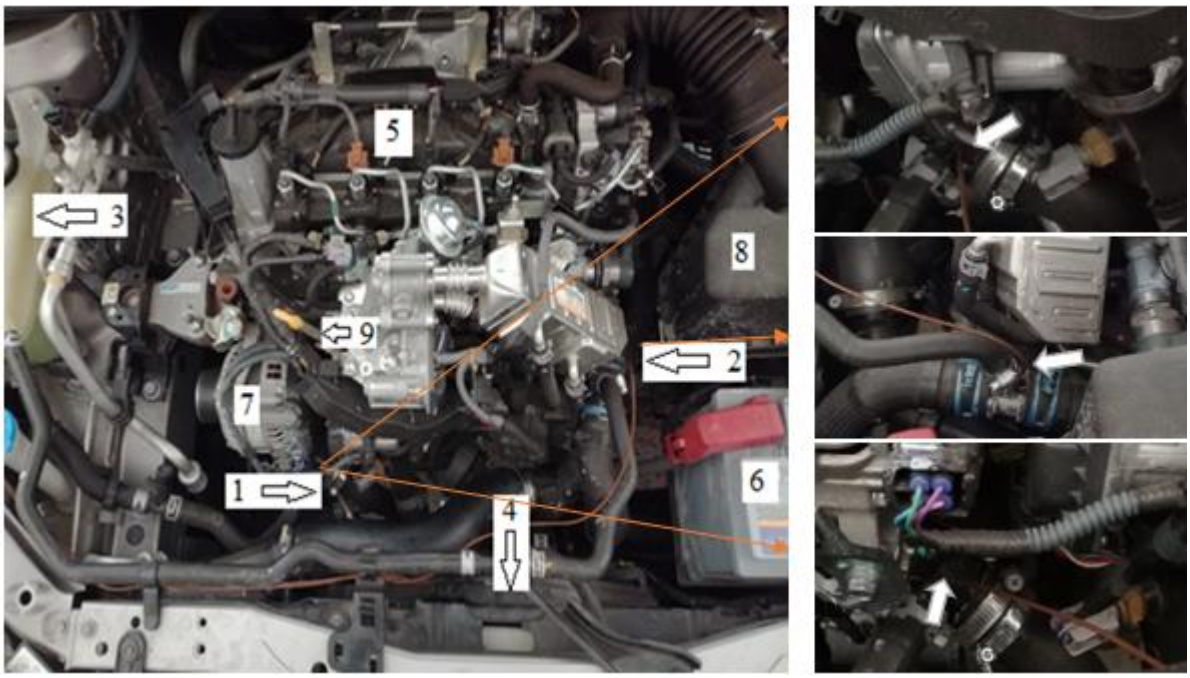

1-Fluid outlet (Radiator inlet thermocouple connection)
1-Thermostat slot
2-Fluid inlet (Radiator outlet thermocouple connection)
3- Expansion tank
4- Radiator
5- Engine
6- Accumulator
7- Alternator
8- Air filter
9- Dipstick

Fig. 2. Temperature measurement points on the engine

2.2. Experimental Setup

The vehicle in the Sivas Cumhuriyet University Automotive Laboratory was used in the experiments. Some technical features of the vehicle and the cooling system on which the tests were carried out are given in Table 3. Fig. 2 shows all temperature measurement points. T-type thermocouples were used in these measurements Thermocouples placed in the motor body are insulated, so they are not affected by the outside temperature. In the experiments, fluid temperatures were measured from the radiator inlet (1) and outlet (2), and all measurements were recorded every 5 seconds with a data logger. The engine rpm of the vehicle was monitored from both the tachometer of the vehicle and the Bosch BEA 350 device, which was connected to the vehicle through the OBD (On-board Diagnostics), and the measurements were made by keeping it at 2000 rpm. In the experiments, the thermostat was removed from the engine to examine the fluid temperature

change continuity and to facilitate fluid circulation.

Table 3. Engine and radiator specifications.

Experiment vehicle	Descriptions
Model of the vehicle	2014
Number of cylinders	4
Engine volüme	1400 cm^3
Fuel type	Diesel
Cooling system	
Heat transfer fluid capacity	~4.5 L
Thermostat opening temperature	~82 °C
Fan operating temperature	~90 °C
Radiator dimensions (mm)	625x390x25

The experimental setup was first filled into the vehicle's cooling system, whose features are specified in Table 3, with the fluid formed by the mixture of EG-W at a ratio of 1:1 as the base fluid, and experiments were carried out. To avoid any problems in fluid circulation, the air of the system was deaerated every time the heat transfer fluid was filled into the engine. In the following stages, the experiments continued by mixing NFs in the same amount of EG-W mixing with the ratio of 0.1% and 0.2% volumetric concentration. Temperatures above 50 °C were included in the experimental measurements. The vehicle was operated in a closed laboratory environment with ventilation to eliminate the differences in experimental operating conditions. The laboratory temperature was kept at 20 °C, and the exhaust gas discharge of the vehicle was given to the outside environment. After the experiments, the engine cooling system was cleaned by washing it with water. The experiments with each fluid (EG-W, EG-W- TiO_2 (0.1%), EG-W- TiO_2 (0.2%), EG-W- Al_2O_3 (0.1%), EG-W- Al_2O_3 (0.2%), EG-W- SiO_2 (0.1%), EG-W- SiO_2 (0.2%)) were repeated four times. In the experimental environment, which was kept at 20 °C, experimental measurements were started when the inlet temperature of the heat transfer fluid to the radiator was 50 °C, and the measurements were terminated when the radiator inlet temperature was 90 °C. At this temperature value, the fan on the radiator was activated, reducing the heat transfer fluid temperature in circulation. In this process, the engine operating cycle was fixed at an average of 2000 rpm. The study measured the time of the heat transfer fluid from the radiator inlet of the cooling system from 50 °C to 90 °C.

2.3. Uncertainty Analysis

The accuracy of the measurement values obtained from the experimental study is critical. There may be errors in temperature measurements due to measurement tools and the experimental system. The error analysis method for determining the uncertainty in experiments was presented by Kline and McClintock [24,33]. Considering the errors occurring during temperature measurement, the total error calculation can be obtained from equation (4). The WR uncertainty arising from different independent variables is obtained from equation (3). In the expressions in the equation, R dependent variable is a function of arguments x1, x2, x3,…, xn. From here: R = R (x1, x2, x3,…, xn). WR is the uncertainty in the result and the uncertainties in the arguments w1, w2, w3,…., wn. The resulting uncertainty expression is as follows:

$$W_R = \left[\left(\frac{\partial R}{\partial x_1} w_1 \right)^2 + \left(\frac{\partial R}{\partial x_2} w_2 \right)^2 + ... + \left(\frac{\partial R}{\partial x_n} w_n \right)^2 \right]^{1/2} \quad (3)$$

Total uncertainty (WR) can be determined as in equation (4);

$$W_R = \left[(a_1)^2 + (a_2)^2 + ... + (a_n)^2 \right]^{1/2} \quad (4)$$

a_1 - Error caused by the measurement device ± 0.5 ºC,

a_2 – Error caused by thermocouple ± 0.5 ºC,

a_3 – Error caused by connection points of measuring elements ±0.1 °C,

a_4 – Average error that can be made in measuring the temperature at the radiator inlet ±0.25 °C,

a_5 – Average error that can be made in measuring the ambient or experimental environment temperature ±0.25°C,

a_6 – Average error that can be made in measuring the temperature at the radiator outlet ±0.25 °C,

The uncertainties in the fluid temperature measurement at the engine radiator inlet, the engine radiator outlet, and the test environment or ambient temperature measurements were determined as ± 0.76 °C for the whole system.

3. Results and Discussion

In Fig. 3, the experiment's results with TiO_2 nanofluid are given. The experiments observed that the base fluid temperature increased to 90 °C in the 609th second. This value was

found to be 680 seconds and 681 seconds for 0.1% and 0.2% TiO_2 NF, respectively. Although reaching the desired temperature early is the desired situation in engines, it should not be forgotten that the thermostat that controls the flow in the engine is removed here. The thermostat makes it easier for the engine to reach the desired temperature by bypassing the flow to the engine until a specific temperature value. It then allows the flow, preventing the engine's temperature from rising further. However, when the thermostat is removed, the fluid that passes freely into the engine increases the time for the engine to reach the desired set value.

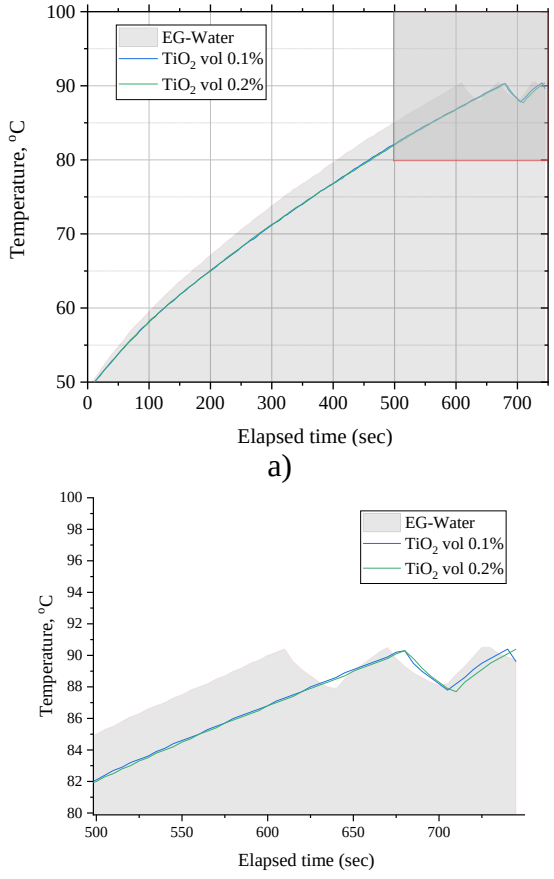

Fig. 3. Comparison of EG-W mixture and TiO_2 (0.1% and 0.2%) NF mixture (50-90 °C)

On the other hand, liquids with higher thermal conductivity transfer more heat to the external environment, extending this period even more. In the case that occurs here, reaching the desired temperature value later can be interpreted as an increase in the thermal performance of the fluid and is attributed to the increase in heat transfer. In Fig. 3, it takes longer depending on the heat discharged from the radiator with 0.1% and 0.2% TiO_2 NF.

However, interestingly, no significant difference was observed between 0.1% and 0.2% TiO_2 NFs. Said et al. [34] found that the rate of increase in TiO_2 NFs between 0.05% and 0.3% was approximately 65% less than the other NF (Al_2O_3) examined. The results obtained from this study and Said et al.'s results show parallelism. As a result, although TiO_2 increases the heat transfer rate, the heat transfer is quite limited with the increase in concentration.

Fig. 4 the results of the experiment with Al_2O_3 NF results. Similar to TiO_2 NF, an increase in heat transfer was observed in 0.1% and 0.2% Al_2O_3 NF. It can be said that the increase obtained here is at a lower rate compared to TiO_2. While the time to reach optimum operating conditions in TiO_2 took 680 seconds, this time was around 655 seconds in Al_2O_3.

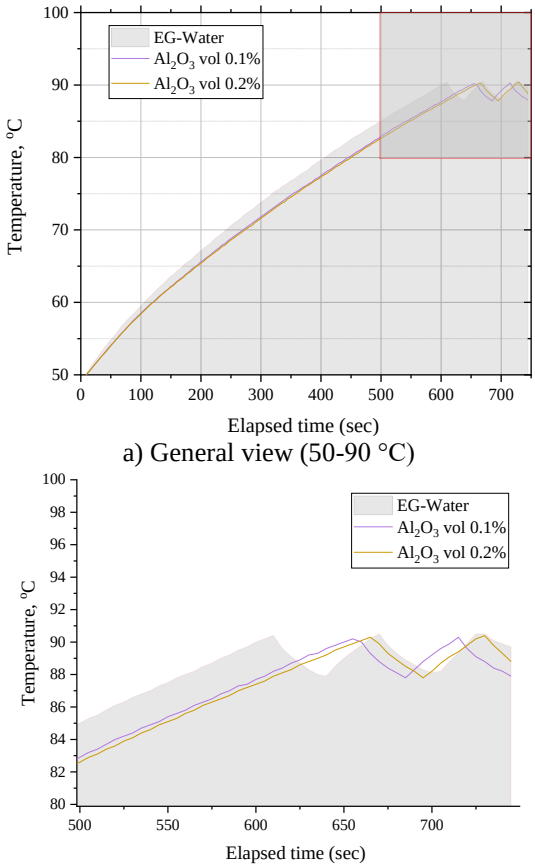

Fig. 4. Comparison of EG-W mixture and Al_2O_3 (0.1% and 0.2%) NF mixture (50-90 °C)

However, unlike TiO_2, there is a distinct difference between 0.1% and 0.2%. The difference increases in parallel with the increase in temperature. Experiment results with SiO_2 NF are given in Fig. 5. The time to reach the optimum operating temperature in

SiO_2 NF compared to other NFs increased significantly under optimum operating conditions. SiO_2 increased the time to reach 90 °C by approximately 14.8%. In addition, SiO_2 NF was also affected at the highest level by the temperature increase. While the 300 sec temperature difference was 0.3 °C, this difference increased to 0.6 °C in 600 sec.

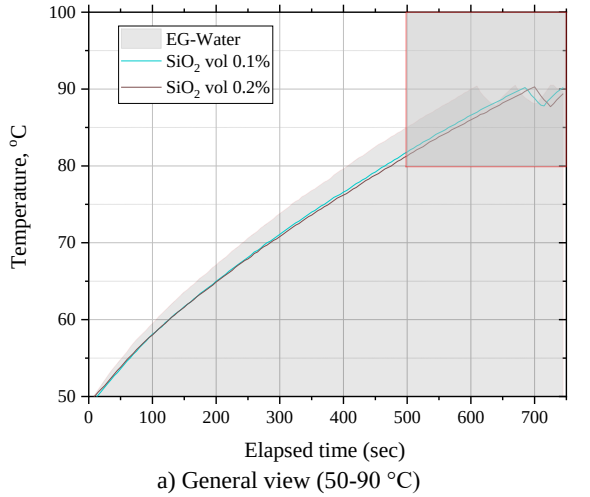

a) General view (50-90 °C)

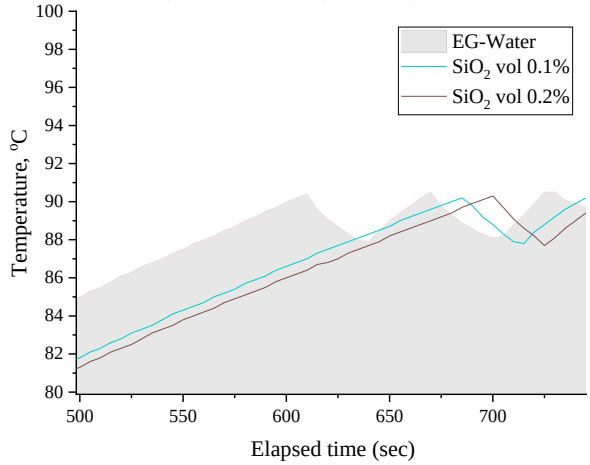

b) Detail view

Fig. 5. Comparison of EG-W mixture and SiO_2 (0.1% and 0.2%) NF mixture (50-90 °C)

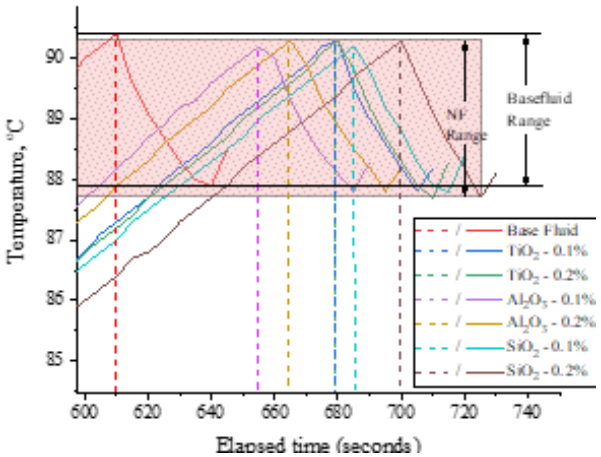

Fig. 6. Comparison of EG-W mixture and 0.1% and 0.2% NF

Comparisons of all examined NFs by concentration value are given in Fig. 6. It was determined that the heat transfer performance of the heat transfer fluid increased by approximately 9% with Al_2O_3 NF, approximately 12% with TiO_2 NF, and approximately 15% with SiO_2 NF. In addition, when the volumetric fractions of NFs mixed into the base fluid were examined, the highest heat transfer values were obtained with 0.2% volumetric fractions. This showed that the increase in NF volumetric fraction in the heat transfer fluid positively affected the heat transfer [15].

Among the NFs used, the highest heat transfer was achieved with the SiO_2 mixture. As it is known, the presence of nanoparticles and their random motion in the base fluid cause the thickness of the thermal boundary layer to decrease and contribute to the improvement of heat transfer. Although the heat transfer enhancement is generally attributed to the nanoparticle dispersion in the literature, the Brownian motions of the particles should not be ignored [35]. It can be said that the smaller size of SiO_2 in our study than the other nanoparticles examined and the Brownian motions (random movement of nanoparticles in the base fluid) due to the relatively increasing number of particles in the nanofluid contribute to the improvement of heat transfer. Compared to the base fluid, TiO_2 Al_2O_3 and SiO_2 NFs with 0.1% concentration extended the time to reach the optimum operating temperature value by 11.5%, 7.4%, and 12.3%, respectively. These values were 11.5%, 9.0% and 14.8% for TiO_2 Al_2O_3 and SiO_2 NFs with 0.2% concentration, respectively. On the other hand, as expected, NFs moved the operating range down. Working fluids were filled into glass containers (jars) after the experiments to monitor the behavior of solid nanoparticles in the base fluid. No sedimentation was observed in EG mixed into water, while there were sedimentations in all NFs, which were kept in the same condition for approximately two weeks. Therefore, sedimentation was identified as a problem for NFs, which had higher heat transfer performance than the base fluid. Therefore, in the cooling systems of vehicles that are kept unused for a long time, the heat transfer fluid will collapse on the canal

surfaces and form a mold layer. However, for frequently used internal combustion engines are not considered a significant problem.

4. Conclusions

This study investigates the usability of 3 different NFs (TiO_2, Al_2O_3, and SiO_2) at different concentration ratios (0.1% and 0.2%) in an existing vehicle cooling system. The results obtained within the scope of the study are thought to contain valuable results in preparing numerical studies and verifying laboratory tests. The essential findings obtained as a result of the study can be listed as follows:

Thanks to nanofluids, the heat produced in the engine is transferred to the environment at higher rates through the radiator, reaching optimum operating conditions later. This situation can be interpreted as an increase in the heat transfer rate and is directly related to the amount of heat transfer. NFs used in the cooling system extended the time to reach optimum operating conditions by 11.5%, 9.0% and 14.8% for Al_2O_3, TiO_2, and SiO_2, respectively.

In the study, it was determined that the performance increase due to the increase in TiO_2 concentration was quite limited. The most remarkable heat transfer change due to the concentration increase was observed in SiO_2. Particle size is thought to be effective here.

The operating temperature range associated with the on-off of the radiator fan has changed in the use of NF. The main reason for this change is that NFs respond faster to thermal changes in the system than the base fluid. Within the scope of the study, the stability states of nanofluids were also investigated. It has been observed that precipitation occurs in nanofluids that are kept for a certain period. It has been observed that nanoparticles adhere to the walls of radiator pipes similarly.

Conflict of Interest Statement

The authors must declare that there is no conflict of interest in the study.

CRediT Author Statement

Tahsin Yüksel: Conceptualization, Supervision, Writing-original draft,**Abdullah Kapıcıoğlu:** Conceptualization, Validation, Data curation, Formal analysis

Acknowledgment

This work is supported by the Scientific Research Project Fund of Sivas Cumhuriyet University under the project number TEKNO-026

Nomenclature

EG	: ethylene Glycol
W	: water
DI	: de-ionized
NF	: nanofluid
MWCNT	: multi-wall carbon nanotubes
OBD	: On-board Diagnostics
V	: volume, m^3
m	: mass (kg)
ρ	: density ($kg.m^{-3}$)
n	: nanofluid
f	: base fluid
1	: initial
2	: final

5. References

1. Said Z., Sohail M., Tiwari A.K., "Automotive coolants", Nanotechnology in the Automotive Industry, 773–792, 2022.

2. Bigdeli M.B., Fasano M., Cardellini A., Chiavazzo E., Asinari P., "A review on the heat and mass transfer phenomena in nanofluid coolants with special focus on automotive applications", Renewable and Sustainable Energy Reviews, 60, 1615–1633, 2016.

3. International Energy Agency, "Transport – Topics – IEA", 2022.

4. Said Z., el Haj Assad M., Hachicha A.A., Bellos E., Abdelkareem M.A., Alazaizeh D.Z., et al., "Enhancing the performance of automotive radiators using nanofluids", Renewable and Sustainable Energy Reviews, 112, 183–194, 2019.

5. Tijani A.S., Sudirman A.S. bin., "Thermos-physical properties and heat transfer characteristics of water/anti-freezing and Al_2O_3/CuO based nanofluid as a coolant for car radiator", Int J Heat Mass Transf, 118, 48–57, 2018.

6. Gupta M., Singh V., Kumar S., Kumar S., Dilbaghi N., Said Z., "Up to date review on the synthesis and thermophysical properties of hybrid nanofluids", J Clean Prod, 190, 169–192, 2018.

7. Alam T., Kim M.H., "A comprehensive review on single phase heat transfer enhancement techniques in heat exchanger applications", Renewable and Sustainable

Energy Reviews, 81, 813–839, 2018.
8. Kapıcıoğlu A., Esen H., "Experimental investigation on using Al_2O_3/ethylene glycol-water nano-fluid in different types of horizontal ground heat exchangers", Appl Therm Eng., 165, 2020.
9. Alous S., Kayfeci M., Uysal A., "Experimental investigations of using MWCNTs and graphene nanoplatelets water-based nanofluids as coolants in PVT systems", Appl Therm Eng, 162, 114265, 2019.
10. Saeed M., Kim M.H., "Heat transfer enhancement using nanofluids (Al_2O_3-H_2O) in mini-channel heatsinks", Int J Heat Mass Transf, 120, 671–682, 2018.
11. Jadar R., Shashishekar K.S., Manohara S.R., "Nanotechnology Integrated Automobile Radiator", Mater Today Proc, 4(11), 12080–12084, 2017.
12. Jadar R., Shashishekar K.S., Manohara S.R., "F-MWCNT Nanomaterial Integrated Automobile Radiator", Mater Today Proc., 4(10), 11028–11033, 2017.
13. Peyghambarzadeh S.M., Hashemabadi S.H., Hoseini S.M., Seifi Jamnani M., "Experimental study of heat transfer enhancement using water/ethylene glycol based nanofluids as a new coolant for car radiators", International Communications in Heat and Mass Transfer, 38(9), 1283–1290, 2011.
14. Hussein A.M., Bakar R.A., Kadirgama K., "Study of forced convection nanofluid heat transfer in the automotive cooling system", Case Studies in Thermal Engineering, 2, 50–61, 2014.
15. Tadepalli R., Gadekula R.K., Reddy K.V., Goud S.R., Nayak S.K., Saini V., et al., "Characterization of Thermophysical properties of Al_2O_3, TiO_2, SiO_2, SiC and CuO Nano Particles at Cryogenic Temperatures", Mater Today Proc., 5(14), 28454–28461, 2018.
16. Subhedar D.G., Ramani B.M., Gupta A., "Experimental investigation of heat transfer potential of Al_2O_3/Water-Mono Ethylene Glycol nanofluids as a car radiator coolant", Case Studies in Thermal Engineering, 11, 26–34, 2018.
17. Ahmed S.A., Ozkaymak M., Sözen A., Menlik T., Fahed A., "Improving car radiator performance by using TiO_2-water nanofluid", Engineering Science and Technology, an International Journal, 21 (5), 996–1005, 2018.
18. Peyghambarzadeh S.M., Hashemabadi S.H., Jamnani M.S., Hoseini S.M., "Improving the cooling performance of automobile radiator with Al_2O_3/water nanofluid", Appl Therm Eng., 31(10), 1833–1838, 2011.
19. Elias M.M., Mahbubul I.M., Saidur R., Sohel M.R., Shahrul I.M., Khaleduzzaman S.S., et al., "Experimental investigation on the thermo-physical properties of Al_2O_3 nanoparticles suspended in car radiator coolant", International Communications in Heat and Mass Transfer, 54, 48–53, 2014.
20. Nieh H.M., Teng T.P., Yu C.C., "Enhanced heat dissipation of a radiator using oxide nano-coolant", International Journal of Thermal Sciences, 77, 252–261, 2014.
21. M'hamed B., Che Sidik N.A., Akhbar M.F.A., Mamat R., Najafi G., "Experimental study on thermal performance of MWCNT nanocoolant in Perodua Kelisa 1000cc radiator system", International Communications in Heat and Mass Transfer, 76, 156–161, 2016.
22. Li X., Zou C., Qi A., "Experimental study on the thermo-physical properties of car engine coolant (water/ethylene glycol mixture type) based SiC nanofluids", International Communications in Heat and Mass Transfer, 77, 159–164, 2016.
23. Elsebay M., Elbadawy I., Shedid M.H., Fatouh M., "Numerical resizing study of Al_2O_3 and CuO nanofluids in the flat tubes of a radiator", Appl Math Model, 40(13–14), 6437–6450, 2016.
24. Elsaid A.M., "Experimental study on the heat transfer performance and friction factor characteristics of Co_3O_4 and Al_2O_3 based H_2O/$(CH_2OH)_2$ nanofluids in a vehicle engine radiator", International Communications in Heat and Mass Transfer, 108, 104263, 2019.
25. Muruganandam M., Mukesh Kumar P.C., "Experimental analysis on internal combustion engine using MWCNT/water nanofluid as a coolant", Mater Today Proc., 21, 248–252, 2020.
26. Mukherjee S., Chakrabarty S., Mishra P.C., Chaudhuri P., "Transient heat transfer characteristics and process intensification with Al_2O_3-water and TiO_2-water nanofluids: An experimental investigation", Chemical

Engineering and Processing - Process Intensification, 150, 107887, 2020.
27. Chiam H.W., Azmi W.H., Usri N.A., Mamat R., Adam N.M., "Thermal conductivity and viscosity of Al_2O_3 nanofluids for different based ratio of water and ethylene glycol mixture", Exp Therm Fluid Sci, 81, 420–429, 2017.
28. Tawfik M.M., "Experimental studies of nanofluid thermal conductivity enhancement and applications: A review", Renewable and Sustainable Energy Reviews, 75, 1239–1253, 2017.
29. Oztop H.F., Abu-Nada E., "Numerical study of natural convection in partially heated rectangular enclosures filled with nanofluids", Int J Heat Fluid Flow, 29(5), 1326–1336, 2008.
30. Al-damook, Amer; Alfelleg, Mohanad A.; Khalil W.H., "Three-dimensional computational comparison of mini pinned heat sinks using different nanofluids: Part one—the hydraulic-thermal characteristics", Heat Transfer, 49(1), 441–460, 2020.
31. Johansson A., Gunnarsson J., "Predicting Flow Dynamics of an Entire Engine Cooling System Using 3D CFD", Luleå University of Technology, 2017.
32. Che Sidik N.A., Witri Mohd Yazid M.N.A., Mamat R., "Recent advancement of nanofluids in engine cooling system", Renewable and Sustainable Energy Reviews, 75, 137–144, 2017.
33. Holman J.P., Experimental methods for engineers, 8th ed., McGraw-Hill Company, 2012.
34. Said Z., el Haj Assad M., Hachicha A.A., Bellos E., Abdelkareem M.A., Alazaizeh D.Z., et al., "Enhancing the performance of automotive radiators using nanofluids", Renewable and Sustainable Energy Reviews, 112, 183–194, 2019.
35. Kakaç S., Pramuanjaroenkij A., "Review of convective heat transfer enhancement with nanofluids", Int J Heat Mass Transf, 52(13–14), 3187–3196, 2009.

e-ISSN: 2146 - 9067

International Journal of Automotive Engineering and Technologies

journal homepage:
https://dergipark.org.tr/en/pub/ijaet

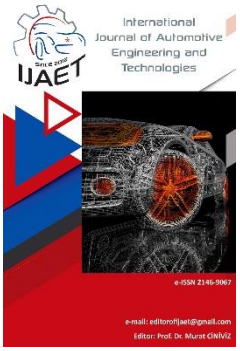

Original Research Article

Design and optimization of runner and gating systems, in high-pressure casting and sand casting, for an aluminum alloy valve cover

Alen Murat Kuyumcu[1, *], Yuşa Haktanır[2]

[1*, 2] Beykent University, Faculty of Engineering and Architecture, Mechanical Engineering, İstanbul, Türkiye.

ARTICLE INFO

Orcid Numbers
1. 0000-0002-6396-5315
2. 0000-0002-4808-7390

Doi: 10.18245/ijaet.1200972

* Corresponding author

alenkuyumcu@yahoo.com

Received: Nov 08, 2022
Accepted: Nov 14, 2023

Published: 31 Dec 2023

Published by Editorial Board Members of IJAET

ABSTRACT

The weight and speed advantage of aluminum die-casting leads to its use in many parts in the automotive industry. Casting simulation programs are used, to avoid time-consuming and expensive production costs, and to design the production process. For casting production one of the most important factors is the runner design, which directly affects castability, material selection, and casting quality. With the correct design of runner systems, there will be no problem with the casting part. In this study, the final part and the runner design for the aluminum alloy valve cover were modeled in CAD, according to the empirical calculations. Furthermore, an appropriate casting method was selected for the valve cover not only according to the results of both high-pressure die-casting and sand-casting simulations but also economic calculations. The main technical parameters for selection were mold and part temperature distribution, liquid metal flow rates, cold shut possibilities, final air quantities, microporosity, and microporosity values. After the final decision, the casting part was produced with high pressure die casting by the implementation of the final runner design.

Keywords: High pressure die casting, Sand casting, Casting simulation, Runner design, Aluminum alloy

1. Introduction

The high-pressure die casting (HPDC) method is used in many sectors today, especially in processes that have complex structures and require many similar parts to be produced. Thus, the production of complex parts from the outside and inside can be performed without any machining process. Manufactured parts are obtained for mass production because of their high repeatability. Parts and components of a large and complex structure can be economically produced using the high-pressure casting method, whereas their production is not possible using another manufacturing process. The injection molding method is a production method that allows the production of complex parts by melting and molding the material at high temperatures. The most important difference that distinguishes injection molding from other production methods is that the parts produced by injection molding do not require finishing operations; even if there is, this is a very rare condition.

Nowadays, small and large parts are produced by the injection molding method. HPDC accounts for almost 70% of aluminum components manufactured today [13]. Many aluminum components for the automotive industry are cast using this method because of its high productivity and near net shape production. Large components, such as gearbox housings and engine blocks, are typical examples of casting weights exceeding 15 kg. Because of the short cycle times, the die is exposed to high temperature fluctuations during each casting cycle, resulting in steep thermal gradients on and below the surface of the die [14]. With HPDC, molten metal is forced into the die cavity under pressure. Because of the high speed of metal filling and rapid solidification rate, this casting process is commonly used to manufacture high-volume, thin-walled castings rather than using other die casting methods, such as gravity or low pressure. Non-ferrous alloys, mainly aluminum, magnesium, and zinc, are most commonly cast using this process. [12]

Many casting methods are used, which are selected depending on the weight of the part, required surface quality, production quantities, and costs. Currently, sand casting (SC) is usually used in the production of casting parts at the prototype stage, whereas other casting methods are used in the production of mass-production parts by casting.

Zheng et al. stated that a good casting simulation should be used to improve casting quality and that simulation programs should reduce cost. They simulated the casting process of a copper alloy water flow meter produced by sand casting while focusing on the effects of different runner designs for optimized casting [10]. Kumar et al. used ProCast to design gating systems for rotary adaptor defect minimization [11]. Hu et al. performed numerical simulations of the design and optimization of runner and gating systems for die-casting thin-walled magnesium telecommunication parts. Two types of runner and gating systems were designed. Suresha and Pawan used Z-cast to design the mold and gate system for a heat sink [1]. Ramnath et al. performed analytic calculations in high-pressure casting for the design of the runner and confirmed the results by casting simulation [5]. Sulaiman and Keen performed flow analysis along the runner and gating system of a casting process using four gates and the angles of the branches leading to the gate [6]. Yang et. al. pointed out the importance of runner design to the mechanical strength of Al–7Si–Mg alloy castings by not only CFD analysis and X-ray radiography [8]. In addition, the four-point bending method was applied. Both numerical and experimental results showed that the vortex-flow runner system (VR) could effectively control the ingate velocity and keep its value lower than 0.5 m/s. As seen above, casting simulations are used more commonly day by day to ensure the quality and optimum production of parts in foundries. It is a great advantage to use casting simulations to provide complex geometry, large volume, and high production quality. Using casting simulations, the percentage of parts scrapped can be decreased. In addition, labor costs and casting times can be optimized for the foundry. To obtain realistic values from the casting simulation, all customized parameters should be entered into the simulation program according to previous experience. If all conditions of the process are defined correctly as simulation inputs, it is possible to obtain values that correlate with real-life values. Casting simulations were used to improve the parts in the design phase and the outputs of the casting properties. If the selected casting method is not suitable for the part design, the design should be revised according to the casting method.

The basic design can be finalized by the inputs of FEA or MBS analysis, while the part design is finished, casting simulations should be applied. If needed, a loop can be examined between the FAE and casting simulations.

2. Methodology

In this study, the appropriate casting method for an aluminum alloy valve cover was selected on the basis of casting simulations. In addition, the runner design was investigated. The engine valve cover, which is the outcome of the project, and the runner were designed using the Catia V5R21 CAD program. The production process of the designed runners and casting parts was simulated using a casting simulation program

called Altair Inspire Cast. Runner designs were made according to the runner calculations and verified by casting simulation. The valve cover was designed with different wall thicknesses for high-pressure die-casting and sand-casting. According to the simulation results, the most suitable casting method was selected, considering casting weight, production time, casting quality, total cost, and scrap rate. The casting simulations were completed by optimizing the mold temperature, runner optimization, riser position, and material temperature distribution. According to Dubey and Smruti (2019), mold design starts with the definition of geometry and material, which are selected according to mechanical and chemical needs [11]. After this process, necessary design corrections can be made according to the molding angle and shrink factor, which is a material feature, and several mold cavities will be decided according to the number of parts that fit into the mold. In the next step, the runner geometry and the location of the inlet channel, which will allow the liquid metal to enter the mold, must be determined while the mold cavities are placed for optimum filling of the casting part. Figure 1 shows the Design methodology systematic of the casting part. This figure is created in the light of the methodology of Dubey and Smruti.

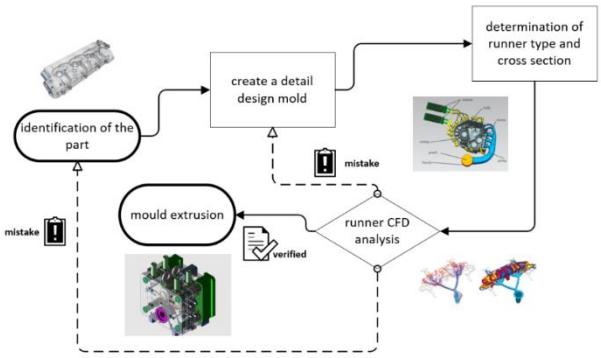

Fig. 1. Design methodology systematics of a casting part

3. Design parameters and calculations

The gating system and its design are the main parameters in the casting processes because they allow the liquid metal to enter the mold and determine the most important properties of the final product. An optimized runner design leads to less scrap and a more homogeneous material distribution. When liquid metal is poured into the mold, turbulence and splashes can occur. During each impact and splash, the molten metal absorbs air, which causes casting voids or porosity on the casting part. Vertical and horizontal runners are generally used in the runner designs that we traditionally use. Different conical spouts in vertical runners and straightforward molten metal descending designs are also known. Conical filling nozzles are usually made of a wide and flat filling nozzle that allows the liquid metal to be easily filled into the mold.

3.1. Characteristics of the valve cover to be used in casting simulations

A valve cover protects engine parts such as rockers, valves, and springs from dust and outer effects and is also used for noise insulation and condensation of evaporated engine oil. They are usually produced from cast or sheet metal or thermoplastic. In this study, we developed two different valve cover designs to fulfill casting production limits. A design is suitable for the high-pressure die-casting method and the other is suitable for the sand-casting method. Not only will the features of these two designs be discussed separately, but there will also be differences in the runner designs. The decision on the appropriate casting process to produce the valve cover will be made according to the final price and product quality. The features of the valve cover used in the high-pressure die casting simulation are listed in Table 1, and those of the valve cover used in the sand-casting simulation are listed in Table 2.

Table 1. Features of the valve cover used in high-pressure die-casting simulation

Determination	Descriptions
Engine type	4 cylinders
Casting part weight	2.3 kg
LengthxWidthxHeight (mm)	~190 x ~513 x ~121
Material	EN AC-46000 (G-Al Si9Cu3)
Runner feed	Bottom feed

Table 3 provides the terminology and key numerical values employed in the calculations for designing runners in high-pressure die-casting. Similarly, Table 4 outlines the terminology and critical numerical parameters used in the design calculations for runners in sand casting.

3.2. High-pressure die-casting design calculations

Machine capacity can be determined as below;

Projected projection area (Ps) including overflow and supply system = AC x AF
Total tonnage for locking =PS x Pi x safety coefficient from Ramnath et al (2014)
According to this information;
Total tonnage = 122,500 mm2 x 320 bar x 10 x 1.05 ≈ 412T
The tonnage required for locking is about 1.2 times the total tonnage.

Table 3. High-pressure diecasting nomenclature and critical numbers

Determination	Descriptions
d (plunger diameter)	75/80/85/90 mm
k (filling rate coefficient)	0.0346
Ti (Temperature of molten metal as it enters the die)	675°C
Tf (Minimum flow temperature of metal)	570°C
Td (Temperature of die cavity surface just before the metal enters)	160°C
S (percent solid fraction allowable in the metal at the end of filling)	25%
Z (The units conversion factor)	3.8
Casting average wall thickness	3 mm
Density	$2.65x10^{-3}$ g/mm^3
The projected area of component (Ac)	1225 cm^2
Draft angle	2°
Angular Tolerance	±0.5°
Specific injection pressure (Pi)	320 bar
Factor of safety	1.05
Stroke length for 550T machine	480 mm
Fill ratio	0.50
1.phase velocity	25 cm/s
2.phase velocity	375 cm/s
Mold material	1.2343

Total tonnage required for locking = 412T * 1.2 ≈ 495T
550t metal injection machine with a cold chamber can be selected according to the result.
Stroke volume can be calculated as below; 126
$V_c + V_{of}$ = 890,000 mm^3*1.4 = 1,246,000 mm^3
Vof: The volume of overflow and feed system, excluding biscuit volume
Actual stroke volume (Vs) = 1,246,000 mm^3 + $\pi*d^2*h/4$ mm^3
The stroke length for the 550-ton cold chamber injection machine is 480 mm; with a biscuit that has 15 mm thickness effective stroke will be decreased to 465 mm.
Assuming a filling rate of 0.50.
Volume offered by injection molding machine;
$= \pi*d^2*(465/4)*0.5$
$1,246,000 + \pi*d^2*(465/4)\ 0.5 = \pi*d^2*(465/4)$
$58*\pi*d^2 = 1,246,000$
$d^2 \approx 6841.65$
$d \approx 82$ mm
The piston diameter was selected as 80 mm.
According to Ramnath et al., the filling rate is defined as the ratio of metal volume to stroke distance [5]. In this work, filling rate was calculated as 0.53 which is an acceptable value.
Again, from same work filling time (FT) is calculated as;
FT = k*[Ti – Tf + s*z]*Tk / [Tf-Td]
t= ({0.0346*[675 – 570 + 25*3.8]*3}) / (570-160)
t = 0.05 sec.
Filling velocity (FV) can be defined as the ratio of liquid metal volume at nozzle inlet to filling time.
FV = 1,246,000 / 0.05 ≈ 24,920,000 mm3/sec
Total gate area (TGA) can be defined as the ratio of filling velocity to liquid metal velocity at gate inlet.
TGA = 24,920,000 mm^3/s / 50,000 mm/s
Total nozzle area ≈ 498 mm^2 / 5 ≈ 100 mm^2

Table 4. Sand casting nomenclature and critical numerical parameters

Determination	Descriptions
Ti (Temperature of molten metal as it enters the die)	750°C
Tf (Minimum flow temperature of metal)	562°C
Td (Temperature of die cavity surface just before the metal enters)	40°C
Casting average wall thickness	5 mm
Density	$2.67x10^{-3}$ g/mm^3
Draft angle	3°
Angular Tolerance	±0.5°
Total casting weight	6.8 kg
Casting time	5 sec.
Mold material	Greensand casting
Coefficient of friction	0.4
Shrinkage (%)	3.4
The surface area of the casting section	4398.9 cm^2

Gate section diameter varies according to various materials. Table 5 shows the areas of the input cross-section thickness, which vary according to the materials in Ramnath et al (2014).

In the optimized runner design, the width of the gate cross-section was 1.25 mm, resulting in a total thickness of 395 mm. As we used 5 gates, each width should be 79 mm. On the other hand, the runner cross-sectional area can be defined as the double of the nozzle area, i.e., 200 mm^2 for the branches.

Table 5. areas of the input cross-section, which vary according to the materials from

Material	Gate Section thickness (mm)
Al-Si – alloy	1 – 1.4
Al-Si Cu – alloy	1.2-2.5
Zn Al4 – alloy	0.35-0.8
Zn Al4 Cu alloy	0.5-1.2
Mg Al2	0.6-2
58-60 brass	1.5-3

3.3. Sand casting design calculations

The height of the flask is selected as 190 mm and the height of the part is 125 mm.

Effective casting height

HE = h – (c/2)

H_E = 19 cm – (12.50 cm / 2)

H_E = 12.75 cm

Critical section (C_a);

$$\frac{22.6 \text{ x } W}{\rho \text{ x } \varepsilon \text{ x } t \text{ x } \sqrt{H_E}} = \frac{22.6 * 6.8}{2.67 * 0.4 * 5 * \sqrt{12.75}}$$

W: Total casting weight (kg)

ρ= density (gr/cm^3)

ε= coefficient of friction

t= casting time (sec)

HE = effective casting height (cm)

Ca ≈ 8 cm^2 = 800 mm^2

Ca, colon = $r^2*\pi$

800 mm^2 = r^2*3.14

r ≈ 16 mm then Ø = 32 mm

Horizontal runner section;

Because the cross-section of the horizontal runner is in a trapezoid profile;

800 mm2 = (a+2a)*2a / 2 =$3a^2$

a ≈ 16 mm

Gate section; Ca x (1.1) ≈ 800 x 1.1≈ 880 mm^2

Number of feeder gate 10 PCs.

880 mm^2 / 10 = 88 mm^2

In general, gate cross-section measurements are experienced in the form of u-4u or u-6u. From the simulation, the gate entry section is taken as u–6u. If the feeder is to be used on the part, the feeder neck does not need to be calculated. According to Brown (1999), if the side feeder is used, it is obtained using MC:MN: MF = 1.0:1.1:1.2 ratio. Because the feeder will be used from the top of the valve cover to be simulated, the feeder neck is not calculated. To calculate the riser module, the component module must be calculated first.

Mc = VC / AC

Mc = 1000 cm3 / 4398.9 cm2 ≈ 0.22

MF = 1.2 x Mc

In the feeder module calculation formula, the safety factor is selected as 1.2 and the safety coefficient is selected as 1.8 which helps to increase the capacity of the feeder to eliminate shrinkage. MF = 1.8 x 0.22 ≈ 0.4 was found and when the module value was entered in the simulation program, the feeder module diameter was designed as 24 mm. Feeder weight;

$W_F = W_T$ x 100/C_c*S_s/100

According to Brown (1999), the optimal feeder metal ratio for Cc is 33% when using a Foseco sleeve, 16% if using a live natural feeder, i.e., a feeder before reaching the liquid metal casting cavity, and 10-14% for another natural feeder.

WF = 3.475 kg*100/14*3.4/100 ≈ 0.8 kg

3.4. Parts of high-pressure die casting and sand-casting process and runner design

In the runner design of the high-pressure die casting process, the casting part is fed with five gates, and chill vent-type ventilation and overflow pockets are used. The runner is designed with rounded lines to avoid sharp corners. The width of the runner was 20 mm, the narrowest area was 10 mm, and the thickness of the pouring basin was 1.25 mm. In the runner design of the sand-casting process, a part is fed with 6 gates without a riser. The offset pouring basin was evaluated according to the simulation results. Rounded lines are used to ensure that the liquid metal is not faced with any resistance when it is entangled in the mold. The width of the runner was 31 mm, the narrowest area was 16 mm, and the filling gate was 4 mm.

Figure 2 shows parts of the high-pressure die-casting process, and Figure 3 shows parts of the sand-casting process. Figure 4 shows a technical drawing of the runner design for high-pressure die casting, and Figure 5 shows a technical drawing of the runner design for sand casting.

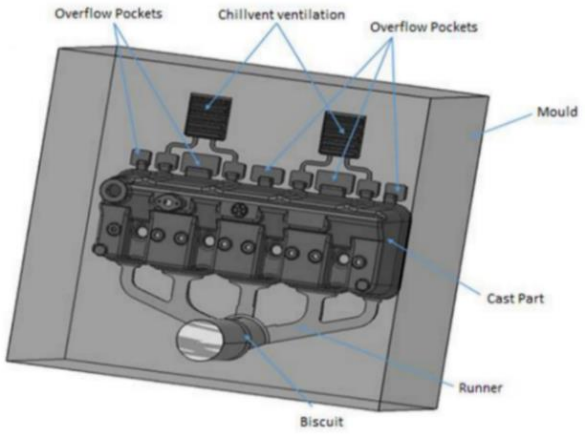

Fig. 2. Parts of the high pressure die casting process

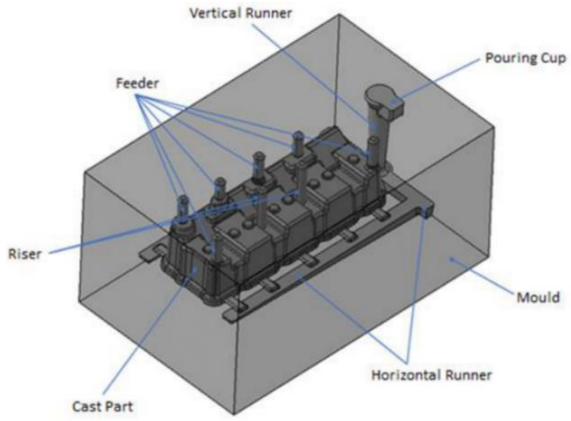

Fig. 3. Parts of the sand-casting process

4. Results and Discussion

These two casting methods have their advantages and disadvantages; however, in this section, a comparison will be performed according to the simulations of the aluminum alloy valve cover. When a well-calibrated casting simulation is used in accordance with the production process, errors in the preliminary design will emerge, and it will be possible to prevent losses such as mold material and labor costs.

4.1. Comparison of mold and part temperature distributions

In aluminum alloys, rapid cooling increases the strength of the casting part. In the literature. The main reason for this strength effect is the dendrite structure formed by the aluminum alloys during cooling. However, it is not correct to link increases in strength to the dendrite structure caused only by rapid cooling; it changes many parameters along with rapid cooling. Aluminum alloys begin to transform into the eutectic composition at approximately 555°C and exhibit high strength in this temperature range. In aluminum casting alloys, solidification should occur at the temperature ranges instead of the constant temperature range. Low mold temperature reduces thermal stress and mold wear.

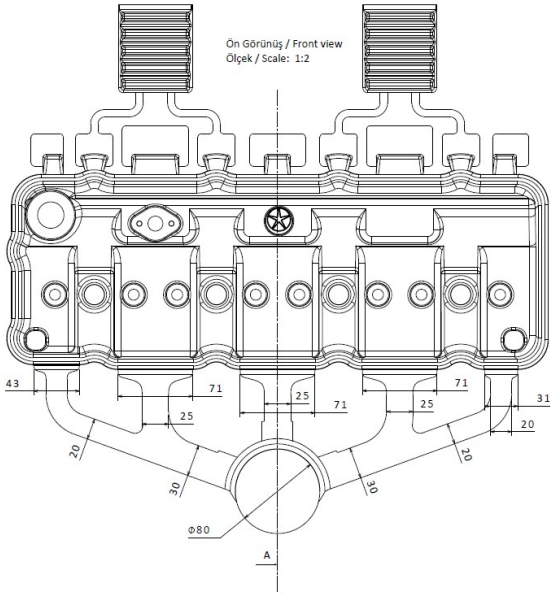

Fig. 4. Technical drawing of the runner to be produced by high-pressure die casting

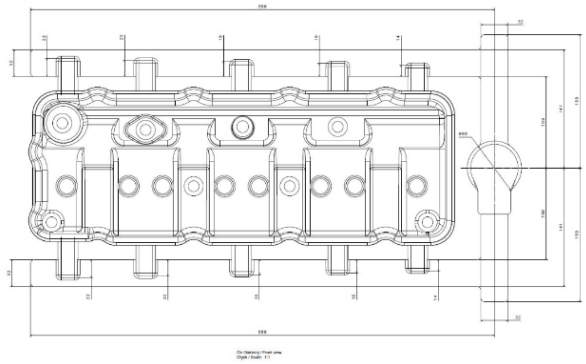

Fig. 5. Technical drawing of the runner to be produced by sand casting

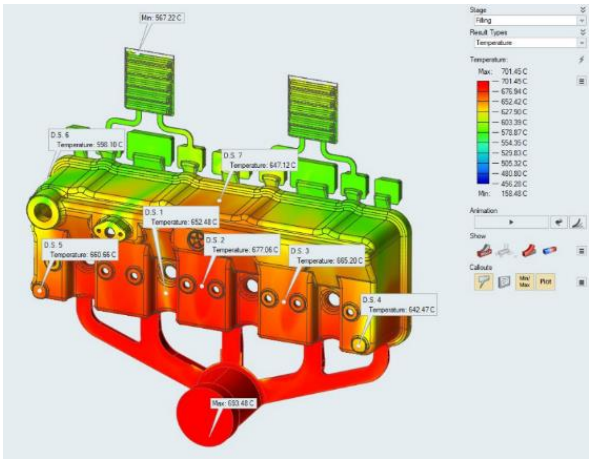

Fig. 6. End of casting temperatures for high pressure die casting

In high-pressure die casting simulation, the maximum mold temperature is 439°C; however, in sand casting 500°C to 545°C. Figure 6 shows the end of casting temperature distribution for high-pressure die casting, and Figure 7 shows the end of casting temperatures for sand casting. Figure 8 shows the temperature distribution 30 s after the start of solidification of high-pressure casting, and Figure 9 shows the same parameter for sand casting. Figure 10 shows a graph of the temperature at the end of the casting for high-pressure casting. Figure 11 shows the same results for sand casting.

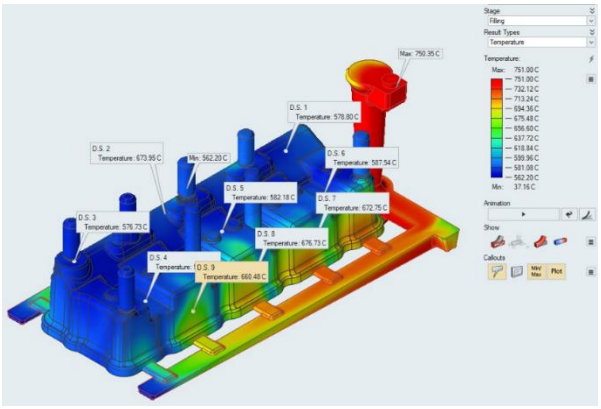

Fig. 7. End of casting temperatures for sand casting

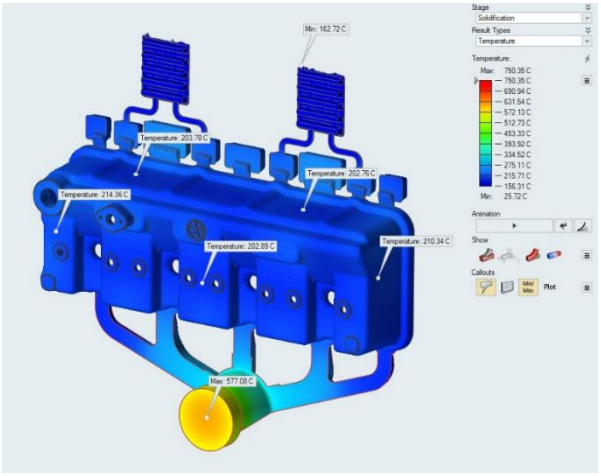

Fig. 8. Temperature 30 s after the start of solidification of high-pressure die casting

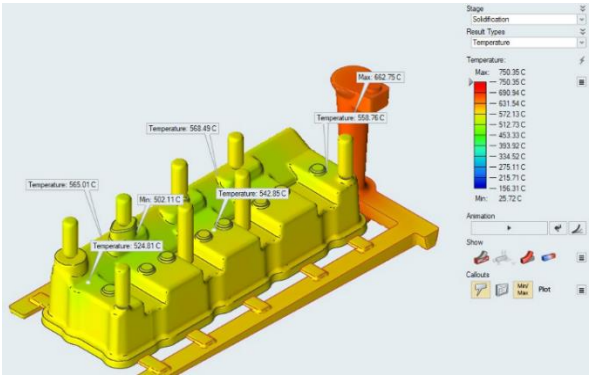

Fig. 9. Temperature 30 s after the start of solidification of the sand-casting part

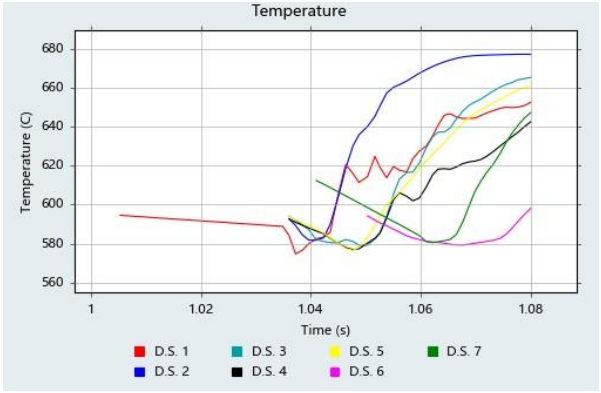

Fig. 10. Graph of the temperature for high-pressure die-casting part

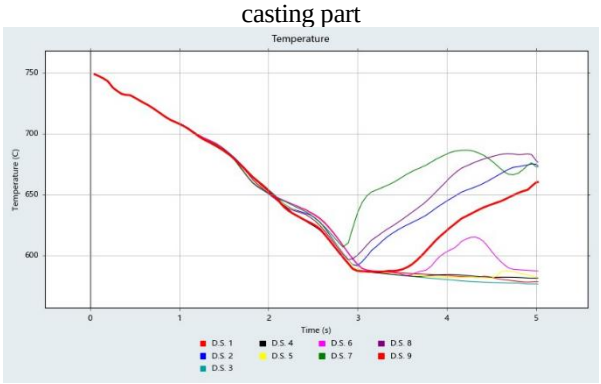

Fig. 11. Graph of the temperature for sand casting part

Figure 12 shows a comparison of the minimum cast temperatures in the 30th second of solidification. Compared with the part temperature distributions, solidification occurs much faster in sand casting than in high-pressure die casting.

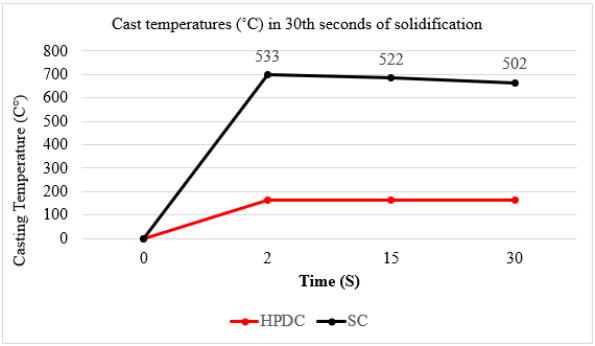

Fig. 12. Comparison of minimum cast temperatures (˚C) in 30th seconds of solidification

4.2. Liquid metal flow rates comparison

When the literature is examined, for high-pressure die casting, liquid metal velocities in the gate part are between 30 and 60 m/s [2], whereas for sand casting, this limit is 0.5 m/s, as reported by Campbell (2003). In addition, surface tension for aluminum was taken as 0.914 N/m [8]. The critical velocity is calculated for sand casting. Consequently, the liquid metal velocities of both casting methods are acceptable. Figure 13 shows

the liquid metal velocities in the gate section of the high-pressure casting. Figure 14 shows the same results for sand casting.

$$V_{critical} = 2 * \sqrt[4]{\gamma g/\rho};$$

$$2 *^4 \sqrt{0.914 \frac{N}{m} * 9.81\ m/s^2\ / 2670\ kg/m^3}$$

$$= 0.48\ m/s$$

$$V_{critical}$$

$$= 2 \times \sqrt[4]{\gamma g/\rho 2} \times \sqrt[4]{0.914 \frac{N}{m} \times 9.81\ m/s^2\ / 2670\ kg/m^3}$$

Liquid metal velocity is not only within acceptable ranges in the sand-casting method but also within acceptable limits for high pressure die casting.

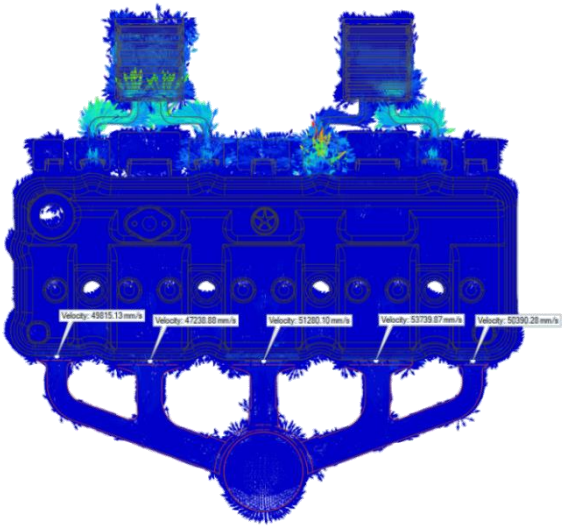

Fig. 13. Liquid metal velocities in the gate section of high-pressure die casting

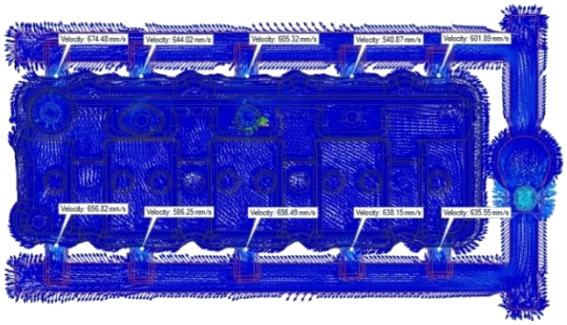

Fig. 14. Liquid metal velocities in gate section of sand casting

4.3. Cold shuts comparison die-casting

Cold shut can be explained as the case in which the liquid metal does not merge because of early solidification during the filling of the mold cavity through two separate channels. Thanks to the improvements made with the simulations, better results were obtained on cold-shut surfaces by increasing the casting velocity. While the filling time is 1.08 s for the runner design of high-pressure die casting, the filling time of the runner design in sand casting is 5 s. By feeding the part from 10 gates, a more linear filling was provided, and a sleeve and riser were added to prevent early solidification. Therefore, the total weight in sand casting is heavier than that in high-pressure die casting. Figure 15 shows the positions and quantities of the cold shuts for HPDC.

Figure 16 shows the positions and quantities of cold shuts for SC. It was observed that the cold shuts were significantly less in HPDC than in the SC method.

Figure 17 shows a comparison of the number of maximum cold-shut points. Figure 18 shows a comparison of the solidification times.

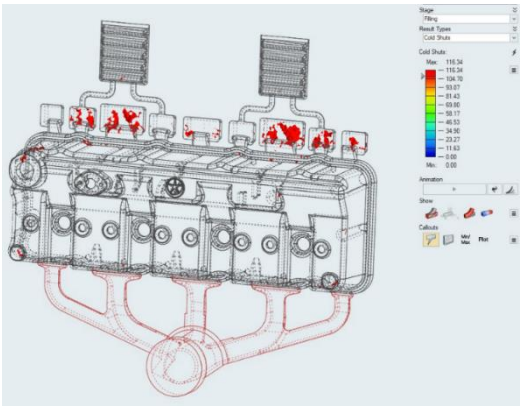

Fig. 15. Positions and quantities of cold shuts for HPDC

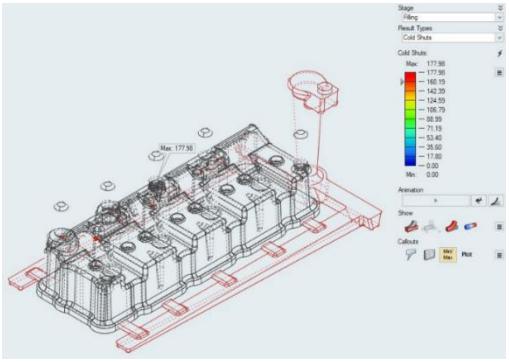

Fig. 16. positions and quantities of cold shuts for SC

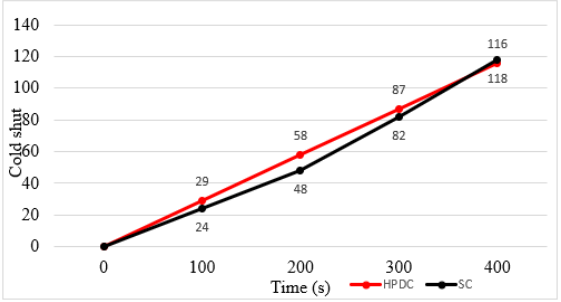

Fig. 17. Comparison of quantities for cold shut points in HPDC and SC

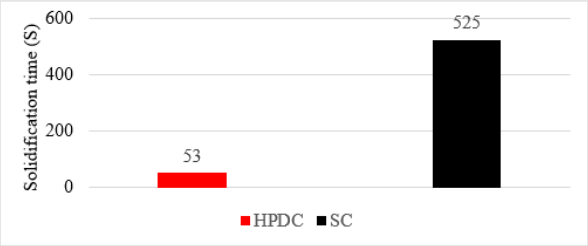

Fig 18. Comparison of the solidification time

4.4. Final air quantity comparison

In the high-pressure die casting process, filling takes very short periods; therefore, the air that fills the mold cavity is trapped in the liquid metal. The design uses chill vent pockets to remove trapped air from the liquid metal. In simulations where air pockets were not added, it was observed that there was too much oxide in the casting part. To ensure a non-air-trapped solution, thus trapped air inside the casting part causes porosity, air pockets were used in the runner design. The simulation parameter showing the final number of air shows where the air will or can be trapped. Since filling the liquid in the sand mold casting process occurs depending on the casting weight, the air that has filled the mold cavity is trapped in the liquid metal and rises to the upper parts of the casting part. A sleeve and riser were used to remove the air-trapped liquid metal from the casting part. A sleeve and riser were used in the design to remove trapped air from the liquid metal. Usage of the sleeve and riser not only will keep the part away from cold shutdown errors but also trap the final air inside the feeder. As in the high-pressure die casting, a high amount of oxide was observed in the casting part when the simulation was performed without the use of a sleeve and riser. Figure 19 shows the final air for HPDC, and Figure 20 shows the final air for SC. Considering the final air quantities, the oxides are transmitted to the ventilation pockets with the help of the liquid metal. HPDC gives slightly better results than the SC method.

4.5. Comparison of porosity

Microporosity can be defined as the voids created by gases during solidification, while macroporosity occurs due to material shrinkage during the same process. Specifically, Figure 21 displays areas with high macroporosity for High-Pressure Die Casting (HPDC), and Figure 22 illustrates high macroporosity regions for Sand Casting (SC). On the other hand, Figure 23 depicts high microporosity areas for HPDC, and Figure 24 showcases high microporosity regions for sand casting.

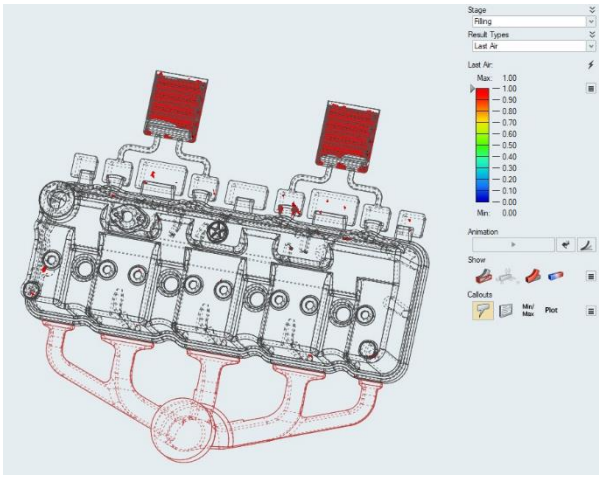

Fig. 19. High pressure die casting for final air

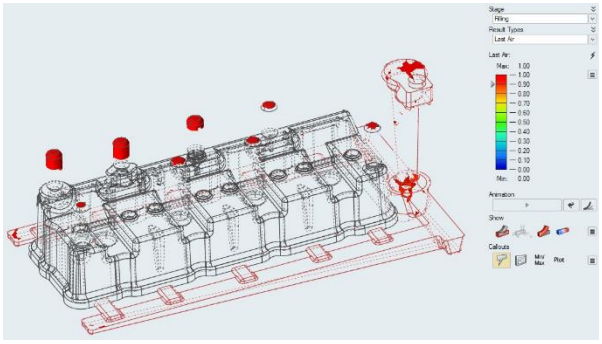

Fig. 20. Sand casting for final air

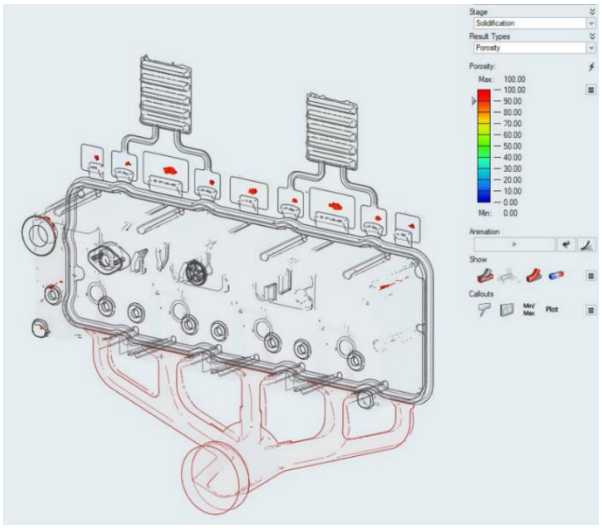

Fig. 21. High macroporosity areas for high pressure die casting

We must acknowledge that the higher mass is not solely attributed to this factor; according to production constraints in sand casting, part thickness should be greater than in high-pressure die casting. Additionally, the high-pressure die-cast method exhibits lower rejection rates in terms of macroporosity quantities.

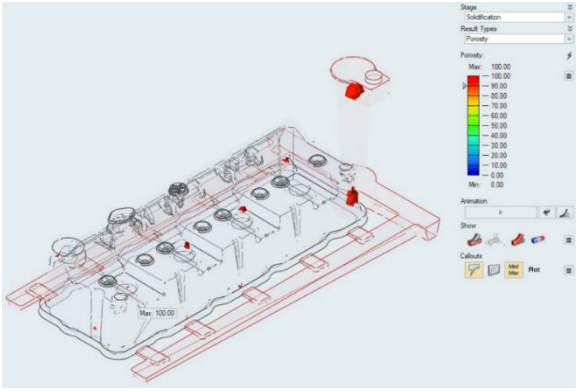

Fig. 22. High macroporosity areas for sand casting

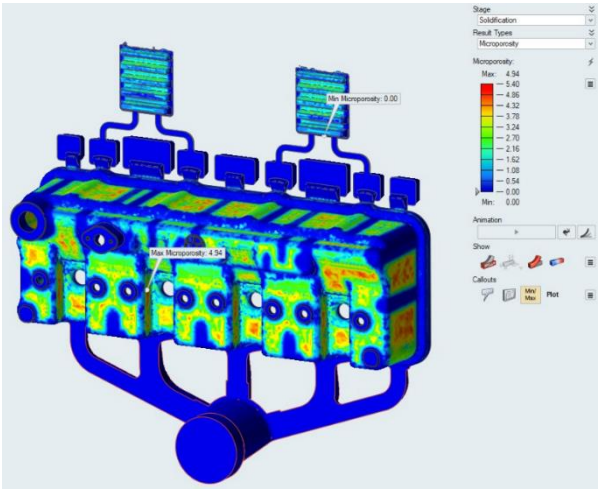

Fig. 23. High microporosity areas for high pressure die casting

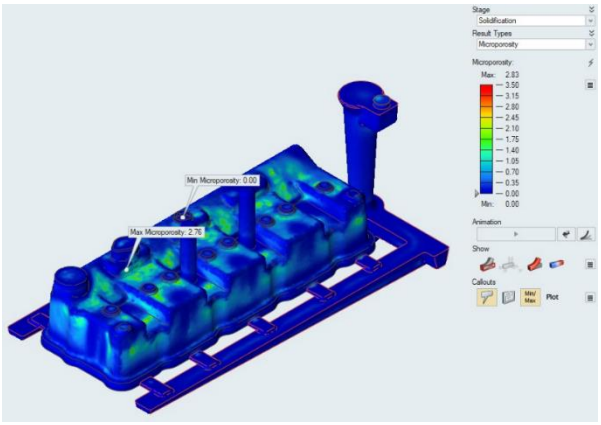

Fig. 24. High microporosity areas for sand casting

From the perspective of the microporosity index, as indicated in the literature and market research, values between 0 and 1 are considered perfect, between 1 and 2 are considered good, between 2 and 5 are considered medium, and values exceeding 5 are deemed bad. Figure 25 presents a comparison of the microporosity index for High-Pressure Die Casting (HPDC) and Sand Casting (SC).

The scrap weight ratio was determined by dividing the total weight of the runner and other casting process sections by the total weight of the entire casting. In the sand-casting method, the scrap rate was 48.9%, while in high-pressure casting, it was calculated at 43.9%.

Notably, the costs associated with high-pressure casting are considerably higher than those in sand casting due to the utilization of a metal die. High-Pressure Die Casting becomes economically feasible when the total annual production exceeds 2150 pieces. Unfortunately, specific cost details are not provided due to confidentiality concerns.

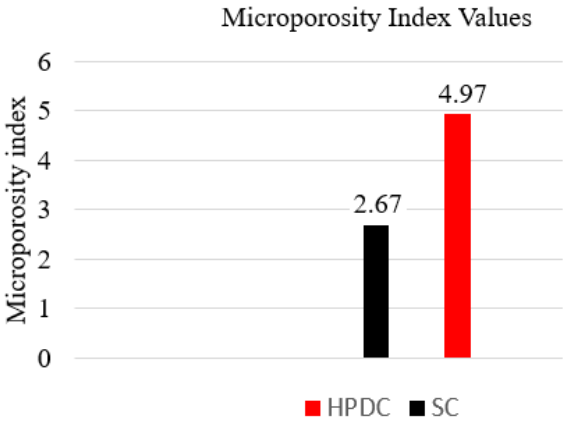

Fig 25. Comparison of microporosity index values

5. Conclusion

In this study, casting simulations were conducted using High-Pressure Die Casting (HPDC) and Sand Casting (SC) methods for the valve cover of a tractor engine. Through these simulations, the optimal casting method for producing the aluminum alloy valve cover was determined. To expedite the analysis process, some initial calculations were performed manually.

For both production methods, the optimum runner design was established with the assistance of simulations. Favorable outcomes were achieved by modifying the gate cross-section, the number of gates, and the width and depth of the runner in the high-pressure die casting simulation. This optimized runner design facilitated problem-free part production.

In sand casting simulations, challenges such as cold junction points, final air content, and early solidification were identified and addressed by adjusting the number of feeders, risers, and gate section thickness to optimize the runner.

Considering the simulation results and cost calculations, High-Pressure Die Casting (HPDC) was deemed the most viable production method for the valve cover. HPDC

resulted in a total casting weight 39.7% lighter than that of Sand Casting, and the latter required a higher percentage of machining. Furthermore, it is anticipated that improved results can be achieved with the use of conditioner and vacuum applications in HPDC.

In sand casting, employing dry sand molding instead of green sand molding is expected to increase mold temperature, potentially leading to better outcomes for issues such as cold shut points and mold erosion.

6. References

1. Suresha S, Pawan H. Numerical simulation aided design of heat sink using Z-cast. Mater Today Proc, vol. 45, Elsevier Ltd; p. 404–11, 2020. https://doi.org/10.1016/j.matpr.2020.12.758.

2. Papai J. Contact heat transfer coefficients in aluminum alloy die casting: An experimental and numerical investigation. Doctoral dissertation. Ohio State University, 1994.

3. Patnaik L, Saravanan I, Kumar S. Die casting parameters and simulations for crankcase of automobile using MagmaSoft. Mater Today Proc, vol. 22, Elsevier Ltd; p. 563–71, 2020. https://doi.org/10.1016/j.matpr.2019.08.208.

5. Jadhav AR, Hujare DP, Hujare PP. Design and optimization of gating system, modification of cooling system position and flow simulation for cold chamber high pressure die casting machine. Mater Today Proc, vol. 46, Elsevier Ltd; p. 7175–81, 2021. https://doi.org/10.1016/j.matpr.2020.11.346.

5. Ramnath BV, Elanchezhian C, Chandrasekhar V, Kumar AA, Asif SM, Mohamed GR, et al. Analysis and Optimization of Gating System for Commutator End Bracket. Procedia Materials Science, 6:1312–28, 2014. https://doi.org/10.1016/j.mspro.2014.07.110.

6. Sulalman S, Chee Keen T, Pertanian Malaysia U, Malaysia S. Flow analysis along the runner and gating system of a casting process. vol. 63. 1997.

7. Kumar R, Madhu S, Aravindh K, Jayakumar V, Bharathiraja G, Muniappan A. Casting design and simulation of gating system in rotary adaptor using Procast software for defect minimization. Mater Today Proc, vol. 22, Elsevier Ltd; p. 799–805, 2020. https://doi.org/10.1016/j.matpr.2019.10.156.

8. Dai X, Yang X, Campbell J, Wood J. Effects of runner system design on the mechanical strength of Al-7Si-Mg alloy castings. Materials Science and Engineering A, 354:315–25, 2003. https://doi.org/10.1016/S0921-5093(03)00021-2.

9. Hu BH, Tong KK, Niu XP, Pinwill I. "Design and optimisation of runner and gating systems for the die casting of thin-walled magnesium telecommunication parts through numerical simulation", Journal of Materials Processing Technolog, 105(1-2):128-133, 2000.

10. Zheng K, Lin Y, Chen W, Liu L. Numerical simulation and optimization of casting process of copper alloy water-meter shell. Advances in Mechanical Engineering, 12, 2020. https://doi.org/10.1177/1687814020923450.

11. Dubey S, Swain SR. Numerical investigation on solidification in casting using ProCast. IOP Conf Ser Mater Sci Eng, vol. 561, Institute of Physics Publishing; 2019. https://doi.org/10.1088/1757-899X/561/1/012049.

12. Long A., Thornhill D., Armstrong C. and Watson D., The Impact of Die Start-Up Procedure for High Pressure Die Casting. SAE International Journal of Materials and Manufacturing. Vol. 6, No.3, June 2013. https://doi.org/10.4271/2013-01-0829

13. Andresen, B., "Die Casting Engineering". New York: Marcel Dekker, ISBN : 0-8247-5935-4, 2005.

14. Klobcar, D and Tusek, J. "Thermal stresses in aluminum alloy die casting dies". Computation Materials Science. 43, 2008. https://doi.org/10.1016/j.commatsci.2008.03.009

e-ISSN: 2146 - 9067

International Journal of Automotive Engineering and Technologies

journal homepage:
https://dergipark.org.tr/en/pub/ijaet

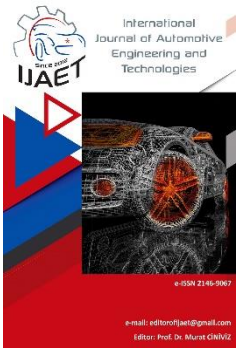

Original Research Article

A benchmarking analysis on electric vehicle emissions of leading countries in electricity generation by energy sources

Adem Uğurlu[1, *]

[1, *] Mechatronics Engineering, Faculty of Technology, Kırklareli University, Kırklareli Türkiye.

ARTICLE INFO

Orcid Numbers
1. 0000-0002-9531-3944

Doi: 10.18245/ijaet.1285587

* Corresponding author
adem.ugurlu@klu.edu.tr

Received: Apr 19, 2023
Accepted: Dec 15, 2023

Published: 31 Dec 2023

Published by Editorial Board Members of IJAET

ABSTRACT

A benchmarking analysis on vehicle emissions has been performed in this study. Sport Utility Vehicle (SUV) powered by electricity is taken into consideration in emission analysis. Calculations have been conducted for leading G20 countries in certain energy sources in electricity generation. According to the analysis, most optimal results are obtained in Volatile Organic Compounds (VOC), Carbon Monoxide (CO), Particulate Matters (PM10 & PM2.5), Sulfur Oxides (SOx), and Carbon Dioxide (CO2) emissions, if the vehicle is charged in France. Only Nitrogen Oxides (NOx) emissions are calculated as to be the lowest values in Canada, compared to other countries. Emissions of an average SUV Internal Combustion Engine Vehicle (ICEV) powered by gasoline are also added to the comparison.

Keywords: Benchmarking; Electric vehicles; Electricity generation; Vehicle emissions.

1. Introduction

Although electric vehicles (EV) do not emit exhaust emissions, they have different amounts of background emissions depending on the energy sources from which the electricity of the vehicle is generated. Therefore, EVs bring about VOC, CO, NO_x, PM_{10}, $PM_{2.5}$, SO_x, and CO_2 emissions, even though there is no exhaust pipe in them at all. There are many studies on why these emissions occur and what kind of damage they cause in the literature. Kim et al. [1] and Schürmann et al. [2] found out that VOC is one of the most deteriorating emissions to the ambient air quality. Derwent et al. [3], Palli et al. [4], and Toro et al. [5] showed that it is an important ozone precursor that increases aerosol formation. In addition, its smoke is dangerous to human life. Above all, VOC smoke irritates human organs such as eyes and lungs [6, 7] and damages some crops, reducing useful agricultural products [8]. CO emissions, mainly resulting from incomplete combustion of hydrocarbon energy sources, is a highly toxic gas that causes death when exposed to high amounts [9]. NO_x emissions, which is a combination of nitric oxide and nitrogen dioxide are emitted to the atmosphere due to very high temperatures in combustion chambers of vehicle engines. Human health and the environment are significantly affected by NO_x emissions [10]. PM pollution is a common vehicle emission in the atmosphere [11] that impairs human health [12] and

disrupts the climate [13]. PM pollution affects the health of living things not only in the short term [14] but also in the long term [15], and exposure to this pollution is the sixth leading risk factor worldwide [12]. PM emissions are largely vehicle-related emissions. Many studies show the negative effects of PM_{10} emissions on human health. Some of these studies focus on children [16], some on pedestrians [17], and some on lung cancer and tuberculosis patients living in urban areas [18, 19]. $PM_{2.5}$ emissions have a great potential to increase cardiovascular and respiratory diseases worldwide [20]. SO_x, another one of the main emissions from vehicles, is also included in the literature. Its negative effects locally and globally deteriorate not only air quality and human health, but also climate change [21, 22]. Finally, carbon dioxide emissions, that is, greenhouse gas emissions, which are mentioned more in the literature than other emissions, are not actually toxic emissions, but their effects are perhaps the worst for life on Earth. Since, one of the most important problems faced by the environment in the last century is climate change, and the main reason for climate change is the increase in greenhouse gases, this problem should be addressed seriously [23, 24]. In brief, these emissions occur due to the characteristics of combustion, characteristics of the energy sources, incomplete combustion, high combustion temperatures, and oxygen deficiencies during combustion; and spread to the environment, causing damages such as various diseases, pollution, and global warming. Therefore, it is very important to reduce the mentioned emissions.

Some energy sources are frequently preferred in electricity production in the world. These are coal, nuclear, oil, natural gas, renewable wastes, hydro, geothermal, wind, and solar. While some of these energy sources cause low emissions in electricity production, some increase harmful emissions. Especially for countries with high energy consumption, which are at the top of the world economy, it is important from which source the electricity is obtained. Hence, the same vehicle causes different emissions in different countries depending on the source from which electricity is produced. In literature, several studies show that this is the case. For example, Wu and Zhang [25] report that in terms of WTW emissions in countries whose electricity grids rely heavily on thermal energy production, EVs may cause higher PM_{10}, SO_2 and NO_X emissions, although they give lower CO_2 emissions compared to internal combustion engines. Doucette and McCulloch [26] suggested that in countries such as India that produce their electricity with carbon-based fuels, EVs may lead to more CO_2 emissions than conventional vehicles. The findings in another study [27] demonstrate the advantages of using decarbonized energy sources in electricity generation to reduce emissions. According to their studies, vehicles charged in the Scandinavian countries, which produce their electricity from renewable energy sources at a higher rate, give lower emissions than those charged in the Balkan countries, which produce their electricity with more traditional methods. Sheng et al. [28] conducted an empirical study and it appeared that EVs offer the most promising results in terms of minimizing energy consumption and emissions as they clearly provide the best values among other fuel type vehicles. Garcia et al [29] found out that the emission advantages of EVs would be decreased if nuclear power plants are closed. Another study [30] that shows EVs as having lower emissions when compared to ICEVs. On the other hand, they concluded that in a country predominantly using coal-fired power plants to generate electricity, it should be focused on to decarbonize the electricity production sector. Garcia and Freire [31] showed in their review study that the electrified vehicle fleet emissions have been directly related to the electricity generation source. Wang and Tang [32] found out in their comparison study that EVs have higher carbon emissions in the production phase, but throughout the life cycle of their carbon emissions are lower than gasoline powered ICEVs.

In this study, VOC, CO, NO_x, PM_{10}, $PM_{2.5}$, SO_x, and CO_2 emissions for the cases that the EV is charged in countries that generate their electricity from different energy sources at different rates are given in the analysis. Countries that are selected from G20 with the best and worst results are presented for each

emission, also comparing to the emissions from an average gasoline powered SUV ICEV.

2. Methodology

The countries compared in this benchmarking analysis have been selected from the G20 countries, so that a small country that obtains all of its electricity from any source does not come to the fore. Since developed countries produce and consume large amounts of electricity, the improvements they will make will contribute greatly to air pollution.

In the emission analysis of the vehicle, processes of the production, transportation, storage, and filling are included with the vehicle operation by that energy source. Electricity generation shares of energy sources, which are given in Table1, are adapted exactly to the declared shares for the related year 2021 [33]. Even some reports show disorders in shares, they are utilized exactly as given by the reference. In G20 countries, South Africa is the leader coal user with 85.78% in electricity production. With 61.22%, Argentina has the highest share in natural gas, with 59.61% Canada in hydro energy, with 11.66% Australia in solar energy, with 20.80% United Kingdom in wind energy, with 30.22% Saudi Arabia in oil, and with as high as 69.33% France in nuclear energy in their electricity generations. World, G20, and OECD average shares of energy sources in electricity production are also given in the figure. The deficiencies in the shares due to some wrong data encountered in the related references are completed to 100% in the analysis using correction values, which demonstrated in the last line of the table.

Emission analysis is performed using GREET software, which determines VOC, CO, NO_x, PM_{10}, $PM_{2.5}$, SO_x, and CO_2 emission values in the study.

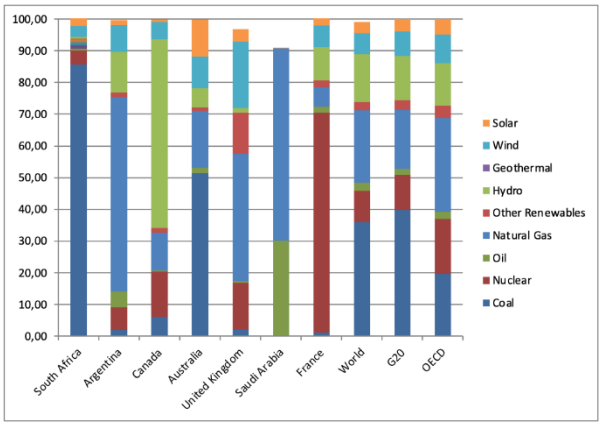

Figure 1: Percentage of the energy sources in electricity generation of the countries.

Electricity powered SUV is selected as a target vehicle to be investigated on emission basis in the analysis. SUVs are getting more attention by years in the world market. Calculation of the emissions is conducted according to the equation as follows, which is detailed by Wang [34]:

$$(TE)_i = \sum_j \left[(CE)_{i,j} + (UE)_{i,j}\right] \times (EC)_j \quad (1)$$

where, , , , and are the total emissions of pollutant i of the energy source throughput for the given process, the combustion emissions of the pollutant i of the energy source j burned, the upstream emissions of the pollutant i of the energy source j utilized to produce and distribute the energy source to the related process, and the energy consumption of the energy source j during the process, respectively. Total emissions are calculated in kg/hkm for every process of all the energy sources depleted through all the combustion and upstream emissions in kg/kJ of consumed energy in kJ/hkm according to the formula.

Table 1: Energy sources in electricity generation of the countries.

%	South Africa	Argentina	Canada	Australia	United Kingdom	Saudi Arabia	France	World	G20	OECD
Coal	85.78	1.91	6.03	51.37	2.10	0.00	1.11	35.99	39.77	19.58
Nuclear	4.27	7.10	14.35	0.00	14.80	0.00	69.33	9.84	11.07	17.33
Oil	0.64	5.20	0.45	1.76	0.50	30.22	1.94	2.53	1.87	2.36
Natural Gas	0.00	61.22	11.85	17.81	40.07	60.55	6.20	22.90	18.78	29.57
Other Renewables	0.18	1.38	1.51	1.25	12.91	0.00	2.05	2.68	2.85	3.85
Hydro	0.57	12.85	59.41	5.98	1.62	0.00	10.59	15.01	14.04	13.37
Wind	3.35	8.49	5.48	10.02	20.80	0.00	6.76	6.54	7.62	9.06
Solar	3.23	1.44	0.81	11.66	4.00	0.23	2.67	3.63	4.00	4.89
Correction	1.98	0.41	0.11	0.15	3.20	9.00	-0.65	0.88	0.00	-0.01

3. Results and Discussion

Table 2 shows VOC, CO, NO_x, PM_{10}, $PM_{2.5}$, SO_x, and CO_2 emissions of an SUV-EV in South Africa, Argentina, Canada, Australia, United Kingdom, Saudi Arabia, and France, with World, G20, and OECD averages. Emissions are given in kg/hkm in the table and the figure that shows how much emission in kg a vehicle emits in 100 km distance cruising of the vehicle. Green color demonstrates the lowest emission values, while red color shows the highest values in the table. Emissions of a reference SUV Spark Ignition (SI) ICEV are also added to the table, which can be compared to SUV EV emissions. SUV SI ICEVs have the highest emissions except NO_x, PMs, and SO_x. As South Africa generates nearly all its electricity from coal (85.78%), it has three highest emissions: PM_{10}, SO_x, and CO_2. Other emissions are also very high compared to the other countries. Argentina generates 61.22% of its electricity from natural gas. Hydro (12.85%), wind (8.49%), and nuclear (7.1%) energy sources find a comparable share in electricity mix in Argentina also. Therefore, Argentina has lower values in all emissions when compared to the other countries. Canada, where its electricity depends highly on hydro (59.41%), nuclear (14.35%), and natural gas (11.85%), has the lowest value in NO_x emissions among all the countries. It can be seen that Canada is the second environmentally friendly country in the list also. Although Australia has a big share (51.37%) of coal consumption in electricity generation, it is the leading country in solar energy to a considerable extent (11.66%) in the list, and that is because the emissions are seemed to be balanced in some degree, still close to the highest values in all emissions with no exception. United Kingdom, wind energy leader (20.80%) in the list, generates its electricity using natural gas as high as 40.07% share with comparable emissions near to the lowest values more than the highest values in all kinds of emissions except CO and CO_2. Saudi Arabia, which is famous for its worldwide oil and natural gas production, naturally also benefits from these energy sources in electricity production, thus becoming the country with the highest emissions, especially in VOC, CO, NO_x, and $PM_{2.5}$. Saudi Arabia is the leader country in oil consumption in electricity generation with a share of 30.22% compared to the countries in the list. It has also a very big share for natural gas, which is as high as 60.55%. France, on the other hand, appears to be the greenest country in the list by means of nuclear energy with the highest share (69.33%) giving the lowest emissions in VOC, CO, PM_{10}, $PM_{2.5}$, SO_x, and CO_2, leaving nuclear energy waste problems to another study. NO_x emissions are also very low in France, near to the lowest value. Finally, the list also gives information about the emissions of World, G20, and OECD averages. Although all three have similar values in emissions, OECD differs slightly from the others in a positive way. The reason for that is the average mix of the energy sources in electricity generation in OECD countries is shifting from coal to nuclear and renewable energy sources compared to the averages of world and G20 countries.

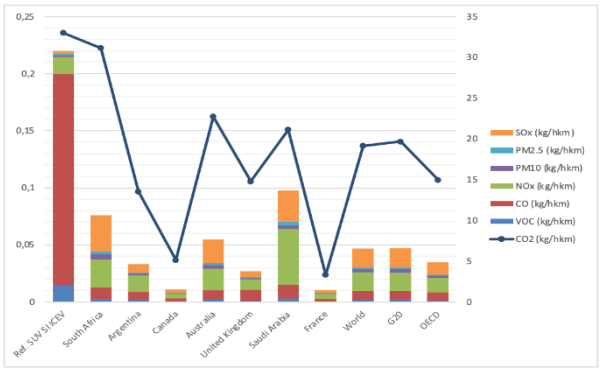

Figure 2: Emissions by countries.

Fig. 2 demonstrates VOC, CO, NO_x, PM_{10}, $PM_{2.5}$, SO_x, and CO_2 emissions of the SUV-EV in South Africa, Argentina, Canada, Australia, United Kingdom, Saudi Arabia, and France, with World, G20, and OECD averages. As clearly seen from the figure, France and Canada have the lower emissions compared to the other countries, thanks to their higher renewable energy shares in electricity production. Saudi Arabia and South Africa on the other hand, have higher emissions due to carbon-based energy source utilization in their electricity generation. CO_2 emissions draw a parallel image compared to the total emissions with slight differences in all countries. Coal in particular is responsible for high CO_2 emissions. It can be understood from the figure that Nuclear (France) and hydro

(Canada) energy sources produce lower CO_2 emissions.

Table 2: SUV emissions in the analyzed countries.

(kg/hkm)	Ref. SUV SI ICEV	South Africa	Argentina	Canada	Australia	United Kingdom	Saudi Arabia	France	World	G20	OECD
VOC	0.0148	0.0027	0.0019	0.0005	0.0021	0.0013	0.0032	0.0004	0.0019	0.0018	0.0015
CO	0.1846	0.0099	0.0070	0.0025	0.0082	0.0094	0.0117	0.0022	0.0077	0.0077	0.0069
NO_x	0.0153	0.0244	0.0147	0.0040	0.0187	0.0091	0.0490	0.0045	0.0166	0.0163	0.0129
PM_{10}	0.0014	0.0050	0.0011	0.0005	0.0033	0.0009	0.0033	0.0004	0.0026	0.0027	0.0017
$PM_{2.5}$	0.0010	0.0023	0.0010	0.0003	0.0016	0.0008	0.0030	0.0003	0.0014	0.0014	0.0010
SO_x	0.0029	0.0316	0.0073	0.0033	0.0209	0.0055	0.0275	0.0027	0.0165	0.0172	0.0109
CO_2	33.0	31.2	13.5	5.1	22.7	14.8	21.1	3.3	19.2	19.7	15.0

While CO_2 emissions vary between 31.2 and 3.3 kgs/hkm, other emissions fluctuate between the approximate values of 0.10 and 0.01 kgs/hkm. On the other hand, the reference SUV SI ICEVs appears to be ranked as the worst vehicle in terms of CO_2 and total emissions.

4. Conclusion

An emission analysis has been conducted benchmarking the leading countries in electricity generation in this study.

The leading countries have been selected from the G20 countries, so that every energy source has the highest share in electricity generation mix. Other energy resource ratios of selected countries are also included in the calculation. Electric SUVs, sales rates of which have been increasing in recent years in the world, have been chosen as the sample vehicles. Gasoline powered SUVs are also presented for comparison. The calculations have been performed using GREET software. VOC, CO, NO_x, PM_{10}, $PM_{2.5}$, SO_x, and CO_2 emissions have been taken into consideration. It can be concluded that France and Canada have been appeared to be the most environmental countries thanks to their low emission energy sources in electricity generation such as nuclear and hydro energy. Saudi Arabia and South Africa, on the other hand, have been seen as the countries that have the highest emissions due to their especially oil and coal utilization in electricity generation. It has also been revealed that SUVs with SI ICEVs have the highest CO_2 and total emissions when compared to EVs in all country selections.

EVs have no emissions when running on road, but they indirectly emit emissions according to how the electricity they are charged with is generated. Therefore, the same vehicle can have different emissions in different countries. This study has revealed that these emissions are high in countries that produce their electricity with carbon-based fuels such as coal, oil, and natural gas; while the emissions are reduced in countries that obtain their electricity from renewable energy sources such as hydro, solar, and wind. Nuclear energy also decreases VOC, CO, NO_x, PM_{10}, $PM_{2.5}$, SO_x, and CO_2 emissions, if nuclear wastes are not taken into consideration, as in this study. While electric vehicles travel on the roads without emitting harmful emissions ensures that the traffic flows in a clean air, generating the necessary electricity with clean energy sources is very important in terms of keeping the whole atmosphere clean. Here, it is important to benchmark with countries that produce their electricity with clean sources and to try to reduce emissions accordingly.

Nomenclature

CO	carbon monoxide
CO_2	carbon dioxide
EC	energy consumption
NO_x	nitrogen oxides
PM_x	particulate matters
NO_x	nitrogen oxides
SO_x	sulfur oxides
TE	total emissions
UE	upstream emissions

Greeks

$\sum$	summation

Subscripts

i pollutant of the energy source throughput for the given process

j energy source utilized to produce and distribute to the related process

5. References

1. Kim K.H., Shon Z.H., Kim M.Y., Sunwoo Y., Jeon E.C., Hong J.H., “Major aromatic VOC in the ambient air in the proximity of an urban landfill facility”, J.

Hazard Mater., 150, Pages 754-764, 2008.
2. Schürmann G., Schäfer K., Jahn C., Hoffmann H., Bauerfeind M., Fleuti E., Rappenglück B., "The impact of NOx, CO and VOC emissions on the air quality of Zurich airport", Atmos. Environ., 41, Pages 103-118, 2007.
3. Derwent R.G., Jenkin M.E., Utembe S.R., Shallcross D.E., Murrells T.P., Passant N.R., "Organic aerosol formation from a large number of reactive man-made organic compounds", Sci. Total. Environ., 408, Pages 3374-3381, 2010.
4. Palli D., Sera F., Giovannelli L., Masala G., Grechi D., Bendinelli B., Caini S., Dolara P., Saieva C., "Environmental ozone exposure and oxidative DNA damage in adult residents of Florence, Italy", Environ. Pollut., 157, Pages 1521-1525, 2009.
5. Toro M.V., Cremades L.V., Calbó J., "Relationship between VOC and NOx emissions and chemical production of tropospheric ozone in the Aburrá Valley (Colombia)", Chemosphere, 65, Pages 881-888, 2006.
6. Durmusoglu E., Taspinar F., Karademir A., "Health risk assessment of BTEX emissions in the landfill environment", J. Hazard Mater., 176, Pages 870-877, 2010.
7. WHO, "Air quality guidelines for Europe", European Series, 91, WHO Regional Publications, Copenhagen, Denmark, 87-91, 2000.
8. Bortolin R.C., Caregnato F.F., Divan Junior A.M., Reginatto F.H., Gelain D.P., Moreira J.C.F., "Effects of chronic elevated ozone concentration on the red oxstate and fruit yield of red pepper plant Capsicum baccatum", Ecotoxicol Environ. Saf., 100, Pages 114-121, 2014.
9. Aldossary M., Almadni O., Kharoshah M., Alsaif D., Alsowayigh K., Alfaraidy M., "Carbon monoxide toxicity in Dammam, KSA: Retrospective study", Egyptian Journal of Forensic Sciences, 5, Pages 36-38, 2015.
10. Alcantara V., Padilla E., Piaggio M., "Nitrogen oxide emissions and productive structure in Spain: an input-output perspective", J. Clean. Prod., 141, Pages 447-461, 2017.
11. Sharma M., Dikshit O., "Comprehensive study on air pollution and green house gases (GHGs) in Delhi", A report submitted to Government of NCT Delhi and DPCC Delhi, 1-334, 2016.
12. GBD 2015 Risk Factors Collaborators, "Global, regional, and national comparative risk assessment of 79 behavioral, environmental and occupational, and metabolic risks or clusters of risks, 1990-2015: a systematic analysis for the Global Burden of Disease study", 2015 Lancet., 388, Pages 1659-1724, 2016.
13. Von Schneidemesser E., Monks P.S., Allan J.D., Bruhwiler L., Forster P., Fowler D., Lauer A., Morgan W.T., Paasonen P., Righi M., Sindelarova K., Sutton M.A., "Chemistry and the linkages between air quality and climate change", Chem. Rev., 115, Pages 3856-3897, 2015.
14. Díaz-Robles L., Cortés S., Vergara-Fernández A., Ortega J.C., "Short term health effects of particulate matter: a comparison between wood smoke and multi-source polluted urban areas in Chile", Aerosol Air Qual Res., 15, Pages 306-318, 2015.
15. Hampel R., Peters A., Beelen R., Brunekreef B., Cyrys J., de Faire U., "Long-term effects of elemental composition of particulate matter on inflammatory blood markers in European cohorts", Environ. Int., 82, Pages 76-84, 2015.
16. Chen Z., Cui L., Cui X., Li X., Yu K., Yue K., Zhang J., "The association between high ambient air pollution exposure and respiratory health of young children: a cross sectional study in Jinan, China", Sci. Total. Environ., 656, Pages 740-749, 2019.
17. Qiu Z., Song J., Hao C., Li X., Gao H.O., "Investigating traffic-related PM exposure on and under pedestrian bridges: a case study in Xi'an, China", Atmos. Pollut. Res., 9, 5, Pages 877-886, 2018.
18. Popovic I., Magalhaes R.J.S., Ge E., Marks G.B., Dong G., Wei X., Knibbs L.D., "A systematic literature review and critical appraisal of epidemiological studies on outdoor air pollution and tuberculosis outcomes", Environ. Res., 170, Pages 33-45, 2019.
19. Stabile L., Massimo A., Rizza V., D'Apuzzo M., Evangelisti A., Scungio M., Buonanno G., "A novel approach to evaluate the lung cancer risk of airborne particles

emitted in a city", Sci. Total. Environ., 656, Pages 1032-1042, 2019.
20. Anderson J.O., Thundiyil J.G., Stolbach A., "Clearing the air: a review of the effects of particulate matter air pollution on human health", J. Med. Toxicol., 8, Pages 166-175, 2012.
21. Aksoyoglu S., Baltensperger U., Prévôt A., "Contribution of ship emissions to the concentration and deposition of air pollutants in Europe", Atmos. Chem. Phys., 16, Pages 1895-1906, 2016.
22. Costa S., Ferreira J., Silveira C., Costa C., Lopes D., Relvas H., Borrego C., Roebeling P., Miranda A.I., Teixeira J.P., "Integrating health on air quality assessment - review report on health risks of two major European outdoor air pollutants: PM and NO_2", J. Toxicol. Environ. Health B., 17, Pages 307-340, 2014.
23. Friedrich T., Timmerman A., Tigchelaar M., Elison Timm O., Ganopolski A., "Nonlinear climate sensitivity and its implications for future greenhouse warming", Sci. Adv., 2, e1501923, Nov 9, Pages 1–11, 2016.
24. Valadkhani A., Smyth R., Nguyen R., "Effects of primary energy consumption on CO_2 emissions under optimal thresholds: Evidence from sixty countries over the last half century", Energy Economics, 80, Pages 680-690, 2019.
25. Wu Y., Zhang L., "Can the development of electric vehicles reduce the emission of air pollutants and greenhouse gases in developing countries?", Transport Res. Part D: Transport and Environ., 51, Pages 129-145, 2017.
26. Doucette R.T., McCulloch M.D., "Modeling the CO_2 emissions from battery electric vehicles given the power generation mixes of different countries", Energy Pol., 39, 2, Pages 803-811, 2011.
27. Kucukvar M., Onat N.C., Kutty A.A., Abdella G.M., Bulak M.E., Ansari F., Kumbaroglu G., "Environmental efficiency of electric vehicles in Europe under various electricity production mix scenarios", J. Clean Prod., 335, 130291, 2022.
28. Sheng M.S., Sreenivasan A.V., Sharp B., Du B., "Well-to-wheel analysis of greenhouse gas emissions and energy consumption for electric vehicles: A comparative study in Oceania", Energy Policy, 158, 112552, 2021.
29. García A., Monsalve-Serrano J., Martinez-Boggio S., Soria Alcaide R., "Carbon Footprint of Battery Electric Vehicles Considering Average and Marginal Electricity Mix", Energy, 268, 126691, 2023.
30. Xia X., Li P., Xia Z., Wu R., Cheng Y., "Life cycle carbon footprint of electric vehicles in different countries: a review", Separation and Purification Technology, 301, 122063, 2022.
31. Garcia R., Freire F., "A review of fleet-based life-cycle approaches focusing on energy and environmental impacts of vehicles", Renew. Sust. Energ. Rev., 79, Pages 935–945, 2017.
32. Wang N., Tang G., "A review on environmental efficiency evaluation of new energy vehicles using life cycle analysis", Sustainability, 14, 3371, 2022.
33. https://ourworldindata.org/electricity-mix.2021, 24/03/2023.
34. Wang M.Q., "GREET 1.5 - Transportation Fuel-Cycle Model. Volume 1: Methodology, Development, Use, and Results", 1999.